Few-Body Systems in a Shell-Model Approach

Dissertation

zur

Erlangung des Doktorgrades (Dr. rer. nat.)

der

Mathematisch-Naturwissenschaftlichen Fakultät

der

Rheinischen Friedrich-Wilhelms-Universität Bonn

vorgelegt von

Simon Tölle

aus

Siegburg

Bonn 2013

Angefertigt mit der Genehmigung der Mathematisch-Naturwissenschaftlichen Fakultät der Rheinischen Friedrich-Wilhelms-Universität Bonn

Referent: Prof. Dr. Hans-Werner Hammer

Korreferent: PD. Dr. Bernard Ch. Metsch

Tag der Promotion: 10.02.2014

Erscheinungsjahr: 2014

Zusammenfassung

Im Rahmen dieser Arbeit werden zunächst Implementierungen zweier verschiedener Schalenmodelle zur Bestimmung von Bindungsenergien in bosonischen Mehrteilchensystemen vorgestellt und verglichen.

Schwerpunktmäßig verwende ich das Schalenmodell zur Beschreibung von Bosonen mit Kontaktwechselwechselwirkungen, die in einem Oszillatorpotential eingesperrt sind, als auch für wechselwirkende ^{4}He-Atome und ihre Clusterbildung. Ausgiebig werden Abhängigkeiten der Resultate im Schalenmodell von seiner Modellraumgröße untersucht und Möglichkeiten geprüft, eine schnellere Konvergenz zu erreichen; wie etwa ein Verschmieren der Kontaktkräfte sowie eine unitäre Transformation der Potentiale. Hierbei werden Systeme betrachtet, die maximal aus zwölf Bosonen bestehen.

Zusätzlich wird ein Verfahren zur Bestimmung von Streuobservablen anhand von Energiespektren von Fermionen im harmonischen Oszillator vorgestellt und geprüft. Schlussendlich werden anhand der Abhängigkeit von Energiespektren von der Oszillatorbreite Position und Breite von Streuresonanzen extrahiert.

Teile dieser Arbeit sind zuvor in folgenden Artikeln veröffentlicht worden:

- S. Tölle, H.-W. Hammer, and B. Ch. Metsch, Universal few-body physics in a harmonic trap, C. R. Phys. **12**, 59 (2011).
- S. Tölle, H. W. Hammer, and B. Ch. Metsch, Convergence properties of the effective theory for trapped bosons, J. Phys. G **40**, 055004 (2013).

Abstract

In this thesis, I introduce and compare an implementation of two different shell models for physical systems consisting of multiple identical bosons.

In the main part, the shell model is used to study the energy spectra of bosons with contact interactions in a harmonic confinement as well as those of unconfined ^{4}He clusters. The convergence of the shell-model results is investigated in detail as the size of the model space is increased. Furthermore, possible improvements such as the smearing of contact interactions or a unitary transformation of the potentials are utilised and assessed. Systems with up to twelve bosons are considered.

Moreover, I test a procedure to determine scattering observables from the energy spectra of fermions in a harmonic confinement. Finally, the position and width of resonances are extracted from the dependence of the energy spectra on the oscillator length.

Some parts of this thesis have been previously published in following articles:

- S. Tölle, H.-W. Hammer, and B. Ch. Metsch, Universal few-body physics in a harmonic trap, C. R. Phys. **12**, 59 (2011).
- S. Tölle, H. W. Hammer, and B. Ch. Metsch, Convergence properties of the effective theory for trapped bosons, J. Phys. G **40**, 055004 (2013).

Contents

Chapter 1

Introduction

Strongly correlated systems play an important role in several fields of physics, ranging from atomic and nuclear to condensed matter physics. The description and understanding of such systems is challenging, since they defy a treatment by perturbative methods. A new perspective is offered in the framework of effective theories and especially of effective field theories (EFT). In particular, systems with a large magnitude of the scattering lengths $|a|$ will be at the focus of this thesis. Below, I shall introduce the concept of the scattering length a, discuss the importance of large scattering lengths a and the description of such a system. But first, I shall cover some relevant experimental issues.

In atomic physics an active field of research concerns the so-called ”BEC-BCS crossover”. This means the transition from the phase of a Bose-Einstein condensate (BEC) of weakly interacting bosons, consisting of tightly bound fermions, to bosonic pairs of weakly interacting fermions, called the cooper pairs, in the Bardeen-Cooper-Schrieffer (BCS) phase. The former phase belongs to small positive scattering lengths with the BEC-limit $1/a \to +\infty$. In contrast, the latter phase is characterised by a small negative scattering length with the BCS-limit $1/a \to -\infty$. Consequently, the crossover happens in the vicinity of the resonance where the interaction leads to an unnatural absolutely large scattering length $1/a \approx \pm 0$. After the discovery of high-temperature superconductors in 1986 and the realisation that their phase seemed to be related to this crossover, a lot of effort was made to examine the phenomenon in other experiments. In 1995, BEC’s could finally be realised in gases of rubidium by Anderson et al. [1]. Great progress was made with the realisation of a BEC in ^{6}Li and ^{40}K by various groups in 2003 [2–4]. These systems enabled a deeper investigation of the crossover with the help of Feshbach resonances, since Feshbach resonances permit a continuous modification of the inter-particle interaction through external magnetic fields and thus a tuning of the scattering length a. An extensive review of the research about the BEC-BCS crossover is given in [5].

Strongly interacting systems with large scattering length occur also in nuclear physics. Prominent examples are the proton-neutron system [6] and the scattering of α particles [7] as well. Furthermore, halo nuclei are at the focus of experimental research [8]. Along with large scattering lengths, they are characterised by a small nucleon separation energy and a large radius, i.e. a long tail in the nucleon density distribution. The main characteristic of halo nuclei is that the inner core is surrounded by weakly bound nucleons. In nature, several halo nuclei could be identified: for example ^{11}Li, the Borromean nucleus ^{6}He and the most exotic nucleus ^{8}He with four weakly bound neutrons.

A successful theoretical approach towards understanding the low energy physics for strongly correlated systems is the application of effective theories. They exploit a separation of scales in systems in order to find the appropriate degrees of freedom and describe their behaviour in a model-independent and systematically improvable way. At each order of the corresponding effective theory there is a fixed number of unknown effective parameters which have to be matched to observables. In the context of quantum field theories the technique of effective theories is used in a multitude of applications. A prominent example is chiral perturbation theory (ChPT), an effective description of quantum-chromo-dynamics (QCD) at low energies [9]. Another example is the halo EFT, which is successfully applied for halo nuclei mentioned above and is based on a dominant large scattering length a [10].

In this thesis, I shall use the framework of the non-relativistic local EFT. Since I shall concentrate on small momenta, a non-relativistic approximation is justified. In the case of non-relativistic field theories, quantum field theory is equivalent to quantum mechanics; such field theories conserve the particle number. Consequently, the principles of effective field theories (EFT) can be applied to quantum mechanical problems, as pointed out by Lepage [11]. Hence, I shall work in a quantum mechanical framework. Deeply connected to the non-relativistic EFT's is the effective range expansion (ERE) in non-relativistic scattering theory [12]. The ERE is the low energy expansion in the squared momentum k^2 of the scattering phase shift $\delta(k)$. The first and the second expansion parameter of the S-wave scattering phase shift are the negative inverse of the scattering length $(-1/a)$ and the effective range r_0, respectively. These parameters can serve as scattering observables to determine the effective parameters in the EFT.

In the non-relativistic local EFT, the Hamiltonian is expressed as the integral of a Hamiltonian density that depends on terms consisting of combinations of quantum fields ψ and their gradients at the same point. The form of the interaction terms in the Hamiltonian are restricted by the principle, that the EFT has to fulfil the same symmetries as the fundamental theory, such as Galilean symmetry [6]. In the situation of a dominant scattering length a, the leading interaction term is the two-body contact interaction without any range. In this case, the in principle highly complicated potentials are then approximated by schematic contact potentials. Accordingly, observables depend only on the scattering length in first order. This limit with vanishing effective range is called the scaling limit. It can be applied to very different physical systems. Therefore regimes with unnaturally large a are called universal. The theoretical interesting limit of $a \to \infty$ is called the unitary limit.

In the three-body system, a new effect occurs in the vicinity of the unitary limit, which was predicted by Efimov in 1970 [13]. The Efimov effect signifies that in the universal regime there are three-body bound states, so-called trimers, with binding energies which are approximately related to the geometric series. In the unitary limit, there are infinitely many trimers with binding energies exactly related to the geometric series with an accumulation point at the 3-body scattering threshold. The first experimental evidence for an Efimov trimer was provided in a trapped gas of ultra-cold Cs atoms by its signature in the 3-body recombination rate [14]. Since this pioneering experiment, there has been significant experimental progress in studying ultra-cold quantum gases and in several experiments the Efimov effect could be detected [15]. So far these experiments were carried out in a regime where the influence of the trap on the few-body spectra could be neglected. However, the trap also offers new possibilities to modify the properties of few-body systems. In particular, narrow confinements can lead to interesting new phenomena.

In the first part of this thesis, I shall focus on these effects. This work is partially an extension of my diploma research topic [16]. For the sake of simplicity the confinement potential is idealised by an isotropic harmonic oscillator potential (HOP). For such an harmonic confinement, the energy spectrum for the two-body sector was determined in the scaling limit by Busch [17]. Furthermore, the binding energies of three-body states could be found in the unitary limit [18]. The main observation is that there are two types of states: The first type includes states, which are completely specified by the scattering length a. States, which belong to the second type, are called Efimov-like and are fixed by the scattering length and an additional three-body parameter. For finite scattering lengths and systems with more particles analytic solutions are unknown.

An established method to treat a confined strongly correlated few body system with spherical symmetry is the shell model. The basic idea is that the infinite-dimensional Hilbert space spanned by (anti-)symmetric products of so-called single-particle wave functions is truncated e.g. by an energy cutoff. Afterwards, a basis is chosen for this finite-dimensional model space. In this model space the Schrödinger equation can be solved, since the Hamiltonian is just a finite matrix which can be diagonalised numerically. There are several versions of shell model approaches which vary in details. I shall concentrate on shell models for bosons with a basis of symmetric products of harmonic oscillator functions. Here, I work with the uncoupled oscillator basis in one-particle coordinates, the so-called M-scheme, as well as with angular momenta coupled basis states expressed in relative coordinates, the so-called J-scheme. Both methods have specific advantages and drawbacks which are pointed out in section 3.3.

The second part is devoted to the description of ^{4}He clusters consisting of A atoms. The theoretical and experimental investigation of atomic clusters is an important part of chemical physics. Helium has two stable isotopes: the rare fermionic ^{3}He and the common bosonic ^{4}He. The latter has the outstanding property that the Efimov effect can be observed directly because of the unnatural large scattering length of ^{4}He atoms [6]. Furthermore, the understanding of ^{4}He clusters is the basis to study properties of ^{4}He liquid droplets and the related phenomenon of super-fluidity of liquid ^{4}He [19]. Also the resonant absorption of nanosecond laser pulses in doped Helium nanodroplets is an active area of research [20].

The existence of ^{4}He A-body clusters could be proved by diffraction experiments from a transmission grating [21]. Unfortunately, properties of the clusters cannot be measured in these experiments, e.g. even the binding energies are not directly observable in these experiments. Only in the two body sector the binding energy of the two-body cluster, the dimer, can be deduced from its size [22].

Various theoretical approaches have been used to investigate such systems and determine the binding energies. Moreover, several ab initio potentials for ^{4}He-^{4}He interaction are constructed within different approaches. The potentials and these approaches are summarised in [23]. The binding energies of the trimer ground and excited state are determined for a variety of these ab initio potentials. I shall concentrate on the so-called LM2M2 potential [23].

For few atoms the sizes and energies of A-body clusters have been calculated with Monte Carlo methods and hyper-spherical adiabatic expansions. Up to the value $A = 10$ numerical results for the ground and first excited states for the LM2M2 potential are presented in [24]. The challenging part in the A-body calculations, as in nuclear physics for the nucleon-nucleon potential, is the treatment of the hard core repulsion of two ^{4}He atoms, which causes a coupling of low and high energy physics. In order to solve the Hamiltonian numerically, some cutoff must be introduced. However, the corresponding results contain large errors due to the coupling of the different energy scales. A possible solution is to construct effective potentials and circumvent the hard core repulsion. For instance, in [25] Gattobigio et al. propose a parametric interaction consisting of an attractive He-He Gaussian potential with a contribution of a Gaussian-hyper-central three-body force, which reproduces the LM2M2 ground state trimer binding energy. Due to the research location of the majority of the related research collaboration, I shall call this potential the Pisa potential. Gattobigio et al. solved the Schrödinger equation with the Pisa potential in the hyper-spherical harmonic expansion for up to six He-atoms and published the binding energies for the ground state and first excited state [25].

There exists, however, a systematic procedure of the similarity renormalisation group (SRG) transformation to construct effective potentials based on unitary transformations. Numerical results become more stable for SRG-transformed potentials at the expense of the introduction of effective many body forces induced. In principle, these forces have to be considered for few body systems.

With my shell model methods for bosons I shall investigate the ^{4}He system for up to twelve particles. In cooperation with Prof. Forssén from Gothenburg, I utilise the Pisa potential as well as the LM2M2 potential as inter-particle potentials. For the purpose of better convergence, here indeed the SRG evolution is exploited.

My thesis is organised as follows. In chapter 2, I outline the quantum mechanical scattering theory and the basics of effective theories. Then the Efimov effect is elucidated and the SRG transformation is introduced. At the end of this chapter, relevant experimental techniques are mentioned, which enable to observe the systems which I consider theoretically in this thesis. Subsequently, I explain both the shell model approaches, which I used, in detail in chapter 3 and compare their merits and demerits. In the following chapter 4, my results for few bosons in the scaling limit in traps are presented. The calculations for atomic clusters of Helium atoms is the subject of chapter 5. In chapter 6, I collect alternative approaches and ideas. Finally, I summarise my results and give an outlook of possible further studies in chapter 7.

Chapter 2

Physical Background

In this chapter I introduce the theoretical concepts and basic principles of experiments for the physical systems considered. At first, the basics of scattering theory are summarised in section 2.1. The definition of differential cross sections, the connection to Green's functions as well as the partial-wave S-matrix are outlined. Afterwards, I give an introduction to effective theories in section 2.2 and explain the local non-relativistic effective field theory (EFT) which will be utilised for resonant interactions. In section 2.3 the Efimov effect is elucidated with and without a confining trap in the form of an oscillator potential. Subsequently, the similarity-renormalisation-group (SRG) transformation method is explained in section 2.4, as I need this technique to handle realistic potentials. At the end, in section 2.5 I mention some experimental techniques for observing the physical systems considered theoretically in my thesis.

2.1 Scattering Theory

Here, I present an overview on the quantum theory of non-relativistic, elastic scattering. It follows the introduction to scattering theory in the textbook of Taylor [12].

2.1.1 Differential Cross Section

For the sake of simplicity, I describe the scattering of a projectile on an infinite-heavy target described by a potential. The reformulation for two-particle scattering in relative coordinates is straightforward.

The starting point is the time-dependent Schrödinger equation with the Hamiltonian H. The Hamiltonian consists of the free part, i.e. the kinetic energy $H_0 = \frac{p^2}{2m}$, and the time-independent potential V. The formal solution of the initial value problem is given with the time evolution operator $U(t)$ as

$$i\frac{\partial}{\partial t}\big|\psi(t)\big\rangle = H\big|\psi(t)\big\rangle \, , \qquad\qquad U(t)\big|\psi\big\rangle := e^{-iHt}\big|\psi(0)\big\rangle = \big|\psi(t)\big\rangle \, . \tag{2.1}$$

In general, a scattering experiment is designed to start with a free incoming wave packet, the asymptotic state $\big|\psi_{\text{in}}(t)\big\rangle = U^0(t)\big|\psi_{\text{in}}\big\rangle$ before the actual scattering process, and to detect long time after the scattering ($t \to \infty$) a free outcoming wave packet, the asymptotic state $\big|\psi_{\text{out}}(t)\big\rangle$. Both packets are asymptotes of the actual orbit $U(t)\big|\psi\big\rangle$, i.e.

$$U(t)\big|\psi\big\rangle - U^0(t)\big|\psi_{\text{in}}\big\rangle \overset{t\to-\infty}{\longrightarrow} 0 \ , \qquad U(t)\big|\psi\big\rangle - U^0(t)\big|\psi_{\text{out}}\big\rangle \overset{t\to+\infty}{\longrightarrow} 0 \ . \tag{2.2}$$

The maps between the actual orbit and the asymptotes define the Møller wave operators Ω_+ and Ω_- by

$$\big|\psi\big\rangle = \Omega_+\big|\psi_{\text{in}}\big\rangle = \lim_{t\to-\infty} U^\dagger(t)U^0(t)\big|\psi_{\text{in}}\big\rangle \ , \quad \big|\psi\big\rangle = \Omega_-\big|\psi_{\text{out}}\big\rangle = \lim_{t\to+\infty} U^\dagger(t)U^0(t)\big|\psi_{\text{out}}\big\rangle \ . \tag{2.3}$$

Thus, the whole scattering process from $\big|\psi_{\text{in}}\big\rangle$ to $\big|\psi_{\text{out}}\big\rangle$ is described by a combination of Møller operators, which is called the S-matrix S. One finds

$$\big|\psi_{\text{out}}\big\rangle = S\big|\psi_{\text{in}}\big\rangle := \Omega_-^\dagger\Omega_+\big|\psi_{\text{in}}\big\rangle \ . \tag{2.4}$$

In momentum space equation (2.4) becomes

$$\big\langle\vec{p}\big|\psi_{\text{out}}\big\rangle = \int \frac{\mathrm{d}^3q}{(2\pi)^3}\ \big\langle\vec{p}\big|S\big|\vec{q}\big\rangle\big\langle\vec{q}\big|\psi_{\text{in}}\big\rangle \ , \tag{2.5}$$

with the S-matrix elements $\big\langle\vec{p}\big|S\big|\vec{q}\big\rangle$. In the end, one is interested in the scattering part of the wave function. Therefore, the trivial contribution is separated. The rest of the S-matrix defines the on-shell T-matrix $t(\vec{q} \leftarrow \vec{p})$. Because of energy conservation a factor $\delta(E_q - E_p)$ occurs and one writes

$$\big\langle\vec{p}\big|S\big|\vec{q}\big\rangle = (2\pi)^3\ \delta^{(3)}(\vec{q}-\vec{p}) - 2\pi i\ \delta(E_q - E_p)\ t(\vec{q} \leftarrow \vec{p}) \ , \tag{2.6}$$

which defines $t(\vec{q} \leftarrow \vec{p})$. The observable in scattering experiments of spinless particles is the differential cross section. The typical situation of scattering experiments is schematically depicted in Figure 2.1.

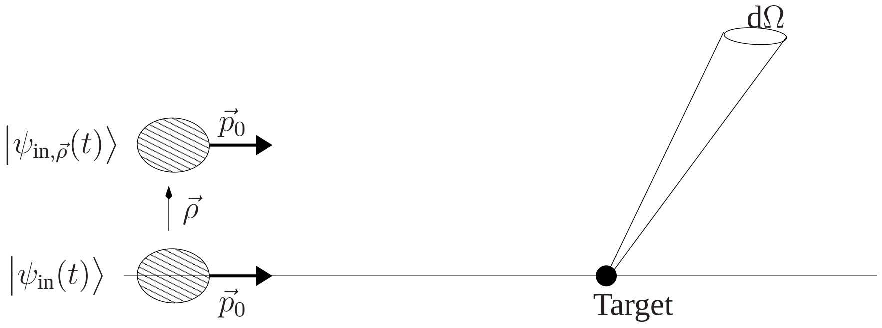

Figure 2.1: Two wave packets $\big|\psi_{\text{in},0}(t)\big\rangle = \big|\psi_{\text{in}}(t)\big\rangle$ and $\big|\psi_{\text{in},\vec{\rho}}(t)\big\rangle$ approach the target with their identical mean momentum $\vec{p}_0$ and two different impact parameters $|\vec{\rho}|$. The quantity $w(\mathrm{d}\Omega \leftarrow \psi_{\text{in},\vec{\rho}})$ is the probability that $\big|\psi_{\text{in},\vec{\rho}}(t)\big\rangle$ is scattered into the solid angle $\mathrm{d}\Omega$.

The incident projectile approaches the target with the asymptote $\big|\psi_{\text{in}}\big\rangle$. Now, the detector measures the outgoing particle under a given solid angle $\mathrm{d}\Omega$. The experiment consists of a sequence of independent collisions. In general the incoming wave packets will have different impact parameters ρ. The cross section $\sigma(\mathrm{d}\Omega \leftarrow \psi_{\text{in}})$ is the relation between the number of scattered particles in the solid angle $\mathrm{d}\Omega$ and all incoming particles with different displacements $\vec{\rho}$. Thus, the cross section is the integration over the impact parameter of the probability $w(\mathrm{d}\Omega \leftarrow \psi_{\mathrm{in},\vec{\rho}})$. Here, $w(\mathrm{d}\Omega \leftarrow \psi_{\mathrm{in},\vec{\rho}})$ is the probability that the projectile with $\vec{\rho}$ is scattered into the solid angle $\mathrm{d}\Omega$. The cross section can be expressed with the outgoing asymptote $\left|\psi_{\mathrm{out},\vec{\rho}}\right\rangle$ via

$$\sigma(\mathrm{d}\Omega \leftarrow \psi_{\mathrm{in}}) = \mathrm{d}\Omega \int \mathrm{d}^2\rho \int_0^\infty \frac{\mathrm{d}p}{(2\pi)^3}\, p^2 |\psi_{\mathrm{out},\vec{\rho}}(\vec{p})|^2 \; . \tag{2.7}$$

By means of equation (2.5), this yields

$$\sigma(\mathrm{d}\Omega \leftarrow \psi_{\mathrm{in}}) = \mathrm{d}\Omega \int \mathrm{d}^2\rho \int_0^\infty \frac{\mathrm{d}p}{(2\pi)^3}\, p^2 \left| \int \frac{\mathrm{d}^3q}{(2\pi)^3} \left\langle \vec{p}\middle|S\middle|\vec{q}\right\rangle \psi_{\mathrm{in},\vec{\rho}}(\vec{q}) \right|^2 \; . \tag{2.8}$$

In general, the incoming asymptote is designed to be peaked around a definite momentum $\vec{p}_0$ and one measures approximately $\sigma(\mathrm{d}\Omega \leftarrow \vec{p}_0)$. The combination of equations (2.6) and (2.7) then leads to

$$\sigma(\mathrm{d}\Omega \leftarrow \vec{p}_0) = \frac{m^2}{(2\pi)^2} |t(\vec{p} \leftarrow \vec{p}_0)|^2 \, \mathrm{d}\Omega \; , \tag{2.9}$$

$$:= \frac{\mathrm{d}\sigma}{\mathrm{d}\Omega}(\vec{p} \leftarrow \vec{p}_0)\, \mathrm{d}\Omega \tag{2.10}$$

with the differential cross section $\frac{\mathrm{d}\sigma}{\mathrm{d}\Omega}(\vec{p} \leftarrow \vec{p}_0)$. The scattering amplitude $f(\vec{q} \leftarrow \vec{p})$ is then defined as $f(\vec{p} \leftarrow \vec{p}_0) := -\frac{m}{2\pi} t(\vec{p} \leftarrow \vec{p}_0)$.

2.1.2 Green's Function

Green's functions are an important concept for scattering theory. The full Green's function $G(z)$ and the free Green's function $G^0(z)$ are formally the resolvents of the Hamilton operator $H = H_0 + V$ and of the free Hamiltonian H_0, respectively:

$$G(z) := (z - H)^{-1} \; , \qquad\qquad G^0(z) := (z - H^0)^{-1} \; . \tag{2.11}$$

The Green's function is analytic in the complex energy plane apart from specific points like bound state energies or resonances, and it has a branch cut on the real axis from 0 to ∞. In scattering theory another useful operator is the T-matrix defined as

$$T(z) = V + VG(z)V \; . \tag{2.12}$$

The integral equations, which relate the Green's function $G(z)$, $G^0(z)$ and $T(z)$, are the Lippmann-Schwinger equations for $G(z)$ and for $T(z)$:

$$G(z) = G^0(z) + G^0(z)VG(z) \; , \qquad\qquad T(z) = V + VG^0(z)T(z) \; . \tag{2.13}$$

Then, for $z = \lim_{\epsilon\downarrow 0}(\frac{p^2}{2m} + i\epsilon)$ one finds

$$t(\vec{q} \leftarrow \vec{p}) = \lim_{\epsilon\downarrow 0} \left\langle \vec{q}\middle| T(p^2/(2m) + i\epsilon) \middle|\vec{p}\right\rangle \; , \tag{2.14}$$

with $|\vec{q}| = |\vec{p}|$ for elastic scattering. Please note, that $\left\langle \vec{q}\middle|T(z)\middle|\vec{p}\right\rangle$ is more general than $t(\vec{q} \leftarrow \vec{p})$. In the complex plane of z, poles in the T-matrix reflect important physical properties. We define $z = k^2/(2m)$ and in the k-plane the poles in the T-matrix $T(k^2/(2m))$ correspond to bound states, if k lies on the positive imaginary axis. If k has an negative imaginary part and a non-vanishing real part, these poles correspond to resonances. The poles on the negative imaginary axis are unphysical virtual states.

2.1.3 Partial-Wave S-Matrix

In the following, I shall focus on stationary scattering theory. For a stationary plane wave $\left|\vec{p}\right\rangle$ the scattered wave function is given by $\left|\vec{p}+\right\rangle := \Omega_+\left|\vec{p}\right\rangle$. For large distances from the scattering region the scattered wave function has the following asymptotic behaviour

$$\left\langle \vec{x}\middle|\vec{p}+\right\rangle \overset{|x|=r\to\infty}{\longrightarrow} (2\pi)^{-3/2}\left(e^{i\vec{p}\cdot\vec{x}} + f(p\hat{x} \leftarrow \vec{p})\frac{e^{ipr}}{r}\right) . \tag{2.15}$$

In case of central forces, the S-matrix is diagonal in the angular momentum quantum number ℓ as well as in the corresponding projection quantum number m and one finds for the scattering amplitude a multipole expansion

$$f(\vec{q} \leftarrow \vec{p}) = \sum_{\ell}(2\ell+1)f_\ell(p)P_\ell(\hat{q}\cdot\hat{p} = \cos(\theta)) , \tag{2.16}$$

where $\hat{q} := \vec{q}/|\vec{q}|$ and P_ℓ are the Legendre polynomials [97]. Unitarity of the S-matrix guarantees that the amplitude can be expressed in terms of the scattering phase $\delta_\ell(p)$ through

$$f_\ell(p) = \frac{1}{p\cot(\delta_\ell(p)) - ip} . \tag{2.17}$$

For low energies the scattering phase behaves as $\delta_\ell \sim p^{2\ell+1}$. Therefore, the s-wave scattering ($\ell = 0$) dominates the scattering in the vicinity of the threshold $p = 0$. The term $p\cot\delta_0(p)$ can be expanded in even powers of p. This is called the effective range expansion (ERE)

$$p\cot(\delta_0(k)) = -\frac{1}{a} + \frac{1}{2}r_0p^2 + \mathcal{O}(p^4) . \tag{2.18}$$

For $p \approx 0$ the scattering length a dominates and determines at leading order all scattering quantities. Poles in the scattering amplitude for non-negative imaginary p lead to bound states. For the limit $a \gg r_0 > 0$, there is a pole in the vicinity of $p = +i/a$; corresponding to a shallow bound state at $E \approx -1/(2ma^2) \approx 0$. In general, the sign of a is crucial for the physical interpretation. A negative a means that the scattering potential is attractive but too weak to build a bound state. Positive scattering lengths are ambivalent: The potential can be either repulsive or attractive, when a bound state could emerge.

2.2 Effective Theories

Effective theories have proved to be very useful in a vast variety of physical systems to describe low energy properties. The application of the concept of effective theories in the quantum field theory framework is called effective field theory (EFT). In section 2.2.1 I give an overview of the basic concepts of effective theories. Subsequently, I consider EFT's and the so-called local EFT for non-relativistic particles with short range interactions. I orient myself on the treatments given in [6, 26].

2.2.1 Basic Concept

An effective treatment is based on a separation of scales for a specific physical system. Separation of scales means that the system has at least two scales with the property $\Lambda_{\text{low}} \ll \Lambda_{\text{high}}$. In the dimensionless small quantity $\Lambda_{\text{low}}/\Lambda_{\text{high}} \ll 1$ then a perturbative expansion can be performed. The expansion up to different orders then defines a tower of effective theories.

A popular simple example is an approximation of Newton's gravitational law, which reads $V_{\text{Newton}} = -GMm/(R+h)$ for an object with mass m in a height h above the earth which has the mass M and radius R, by a constant earth acceleration g, which yields $V_{\text{Newton}}^{(\text{eff})} = +mgh$. The high scale is the radius $\Lambda_{\text{high}} = R$ and the low scale is the height $\Lambda_{\text{low}} = h$. Newton's potential can be expanded in $\Lambda_{\text{low}}/\Lambda_{\text{high}} = h/R$ and one has

$$V_{\text{Newton}} = -\frac{GM}{R}m\left(1 - \frac{h}{R} + \frac{1}{2}\left(\frac{h}{R}\right)^2\right) + \mathcal{O}\left(\left(\frac{h}{R}\right)^3\right) . \tag{2.19}$$

The first term is just a constant and irrelevant, since potentials can be measured only relatively and not absolutely. The leading order in the effective theory is exactly mgh with identification of $GM/R^2 = g$ as the coupling constant. At next to leading order a second coupling constant $g_2 = -GM/(2R^3)$ appears in the term g_2mh^2.

In spite of the simplicity of this example, several characteristic features of effective theories are evident: The accuracy of the theory can be improved systematically with each order. The small expansion parameter establishes a so-called power-counting scheme to sort the expansion terms by importance. Coupling constants absorb the physics at the high scale and finally, the theory predicts the scale of its own collapse at $h \approx R$. In general the coupling constants cannot be determined by the fundamental theory. Either the fundamental theory is unknown or the fundamental theory is too complex to calculate the coupling constants explicitly. In these cases, the coupling constants are to be determined by experimental data.

2.2.2 Effective Field Theory

Historically, EFT's have been formulated in the field of nuclear physics. This was encouraged by the endeavour to overcome model dependent descriptions of hadronic and nuclear properties and to find a model-independent approach for the strong interaction with QCD as the fundamental theory.

Nowadays, two effective theories are used for strong interactions: chiral effective field theory (χEFT) [9] and the pionless EFT ($\not\pi$EFT) [27]. The former bases on the approximate chiral symmetry of the QCD Lagrangian, i.e. the invariance under the separate transformations of left-handed and right-handed fields with the group SU(3)$_L\times$SU(3)$_R$. However, the chiral symmetry is hidden due to spontaneous breaking of this group to SU(3)$_V$. According to the Goldstone theorem, this spontaneous breaking induces eight mass-less Goldstone bosons. Consequently, the eight lightest mesons in the spectrum, the pions, kaons and η, are identified with the Goldstone bosons as the explicit dynamical degrees of freedom. Since the symmetry is broken explicitly by the small and various quark masses, the Goldstone bosons obtain finite masses.

Thus, the χEFT is an expansion around the chiral limit and has two high scales $\Lambda_{\text{high}}^{\chi}$. The first one is the so-called chiral symmetry breaking scale $\Lambda_{\text{CSB}} = 4\pi f_\pi$ where f_π is the pion decay constant. The second one is the mass m_ρ of the lightest vector meson ρ, which is integrated out and is not a dynamical degree of freedom anymore. The low scales $\Lambda_{\text{low}}^{\chi}$ are the momentum p of the considered process and the masses of the dynamical degrees of freedom $m_{\pi,\kappa,\eta}$. Consequently, the expansion is in powers of the small parameters $\Lambda_{\text{low}}^{\chi}/\Lambda_{\text{high}}^{\chi}$, where

$$\Lambda_{\text{low}}^{\chi} \in \{m_\pi, m_\kappa, m_\eta, p\} \qquad \text{and} \qquad \Lambda_{\text{high}}^{\chi} \in \{4\pi f_\pi, m_\rho\} . \tag{2.20}$$

The pionless EFT ($\not{\pi}$EFT) is used for nucleon-nucleon reactions for momenta $p \ll m_\pi$. In χEFT the nucleon interactions are strong and lead to non-perturbative phenomena. Thus, the effects cannot be treated in the normal power-counting scheme of χEFT. The reason behind this is the unnatural large scattering length $a \gg 1/\Lambda^{\chi}_{\text{high}}$ of the nucleon-nucleon scattering and the associated shallow bound states at the vicinity of $E = \frac{1}{2\mu a^2}$ with the reduced mass μ. In the next section the basics of the $\not{\pi}$EFT are considered.

2.2.3 Local Non-Relativistic EFT

The local non-relativistic EFT relies on the scattering length being large and is independent of the mechanism responsible for this. This is summarised in the term universality. This theory can be applied in nuclear physics, known as $\not{\pi}$EFT, in atomic as well as particle physics.

The starting points of EFT's are the Lagrangian densities. In local quantum field theories the Lagrangian density is constructed with terms consisting of a combination of quantum fields ψ and their gradients at the same point only. Accordingly to the symmetry principle [28], e.g. all terms which fulfil Galilean symmetry, are included. Furthermore, terms which differ only by integration by parts are equivalent, because the difference is just a boundary term. Since one is interested in small momenta, terms with higher derivatives are suppressed. Consequently, at leading order the Lagrangian is given by

$$\mathcal{L} = \psi^\dagger(\vec{x},t)\big(i\frac{\partial}{\partial t} + \frac{1}{2m}\Delta_x\big)\psi(\vec{x},t) - \frac{g_2}{4}\big(\psi^\dagger(\vec{x},t)\psi(\vec{x},t)\big)^2 - \frac{g_3}{36}\big(\psi^\dagger(\vec{x},t)\psi(\vec{x},t)\big)^3 + \cdots \; . \tag{2.21}$$

The ellipses indicate the terms in higher power-counting order. The leading order corresponds to the limit of zero range interactions, the so-called scaling limit. It is equivalent to the truncation of the ERE after the effective range term $1/a$, which is justified for $1/k \geq a \gg r_0$.

This quantum field theory is equivalent to a quantum mechanical description because no anti-particles terms are present and sectors with different particle numbers decouple in the Fock space. In short, the quantum fields $\psi^\dagger(\vec{x},t)$ and $\psi(\vec{x},t)$ create a particle at position $\vec{x}$ at time t or destroy a particle, respectively. For bosons, the fields fulfil the commutator relation

$$\big[\psi^\dagger(\vec{x},t), \psi(\vec{y},t)\big]_- = \delta^{(3)}(\vec{x}-\vec{y}) \; , \tag{2.22}$$

and all other commutator relations vanish identically. With the relation to the Hamiltonian density

$$\mathcal{H}(\vec{x},t) = \frac{\partial\mathcal{L}}{\partial\dot{\psi}}\dot{\psi} - \mathcal{L} \; , \tag{2.23}$$

$$= \psi^\dagger(\vec{x},t)\, \frac{-\Delta}{2m}\, \psi(\vec{x},t) + \frac{g_2}{4}\big(\psi^\dagger(\vec{x},t)\psi(\vec{x},t)\big)^2 + \frac{g_3}{36}\big(\psi^\dagger(\vec{x},t)\psi(\vec{x},t)\big)^3 + \cdots \; , \tag{2.24}$$

the quantum field formulation can be rewritten in the quantum mechanical formulation with the Hamiltonian H. As an example I consider the 2-body sector where the three-body term in the

Lagrangian density is then irrelevant. After normal ordering, denoted by two colons, one finds

$$\begin{aligned}
&\big\langle \vec{x},\vec{y}\big|\int \mathrm{d}^3z \;:\mathcal{H}(\vec{z},t):\big|\phi_1,\phi_2\big\rangle \\
&= \int \mathrm{d}^3z d^3v d^3w \big\langle \vec{x},\vec{y}\big|: \psi^\dagger(\vec{z},t)\frac{-1}{2m}\Delta_z\psi(\vec{z},t) + \frac{g_2}{4}\big(\psi^\dagger(\vec{z},t)\psi(\vec{z},t)\big)^2 :\big|\vec{v},\vec{w}\big\rangle \\
&\quad \big\langle \vec{v},\vec{w}\big|\phi_1,\phi_2\big\rangle\;, \qquad (2.25)\\
&\propto \Big[-\frac{1}{2m}\Delta_x - \frac{1}{2m}\Delta_y + \frac{g_2}{2}\delta^{(3)}(\vec{x}-\vec{y})\Big]\;\big(\phi_1(\vec{x},t)\phi_2(\vec{y},t)+\phi_1(\vec{y},t)\phi_2(\vec{x},t)\big)\;, \qquad (2.26)\\
&= H\;\big(\phi_1(\vec{x},t)\phi_2(\vec{y},t)+\phi_1(\vec{y},t)\phi_2(\vec{x},t)\big)\;. \qquad (2.27)
\end{aligned}$$

2.2.3.1 Two-Body Scattering

In this section I investigate the scattering of two identical bosons with the EFT described above. In order to calculate the scattering amplitude from the Lagrangian in the scaling limit, the Feynman rules read as follows: The Feynman propagator for a particle of mass m with energy k_0 and momentum $\vec{k}$ is given by $i/(k_0 - k^2/(2m) + i\epsilon)$. The only vertex contribution is a constant $-ig_2$. Note that g_2 is not small in general. Thus, the scattering amplitude cannot be determined perturbatively with the Dyson series: a re-summation of the loop-diagram contributions has to be performed. Finally, this yields the Lippmann-Schwinger equation for the T-matrix, see equation (2.13). At on-shell energies the T-matrix coincides with the scattering amplitude, see equation (2.14).

In Figure 2.2 the equations for the scattering amplitude are depicted diagrammatically. It describes scattering of two identical bosons with reduced mass $\mu = m/2$, relative energy $E = k^2/(2\mu) = k^2/m$ and momentum $\vec{k}$. Thus, in the centre-of-mass frame for $|\vec{k}\,'| = |\vec{k}|$ the integral equation diagram reads

$$\begin{aligned}
&\big\langle \vec{k}\,'\big|T(E)\big|\vec{k}\big\rangle \\
&= +g_2 + \frac{i}{2}g_2^2\int\frac{\mathrm{d}^3q}{(2\pi)^3}\int\frac{\mathrm{d}q_0}{(2\pi)}\,\frac{1}{q_0-\frac{q^2}{2m}+i\epsilon}\,\frac{1}{E-q_0-\frac{q^2}{2m}+i\epsilon}\big\langle\vec{q}\big|T(E)\big|\vec{k}\big\rangle\;. \qquad (2.28)
\end{aligned}$$

Because of the contact interaction, the T-matrix simplifies and depends only on the energy E and is independent of the direction $\hat{k}'$. At on-shell energies, $E = |\vec{k}|^2/(2\mu)$, the T-matrix is related to the scattering amplitude as follows:

$$\mathcal{A}_2(E) := -\lim_{\epsilon\downarrow 0}\big\langle\vec{k}\,'\big|T(E+i\epsilon)\big|\vec{k}\big\rangle = -t(\vec{k}\,'\leftarrow\vec{k}) = +2\frac{2\pi}{\mu}f(\vec{k}\,'\leftarrow\vec{k})\;. \qquad (2.29)$$

Due to the identity of the bosons, there is an additional factor of two.

Note that the integral over $\vec{q}$ in equation (2.28) diverges. This signifies that the Lagrangian is ill-defined as such and has to be regularised. Likewise, the corresponding Hamiltonian is not self-adjoint because of the contact interaction in the form of the term with the δ-distribution. A possible regularisation is a momentum cutoff Λ, i.e. the integration is substituted by $\int_{\vec{q}\leq\Lambda}\mathrm{d}^3q$. Thereafter, the integral become finite but cutoff-dependent with the result

$$\mathcal{A}_2(E) = -g_2\big[1+\frac{mg_2}{4\pi^2}\big(\Lambda-\frac{\pi}{2}\sqrt{-mE-i\epsilon}\big)\big]^{-1}\;. \qquad (2.30)$$

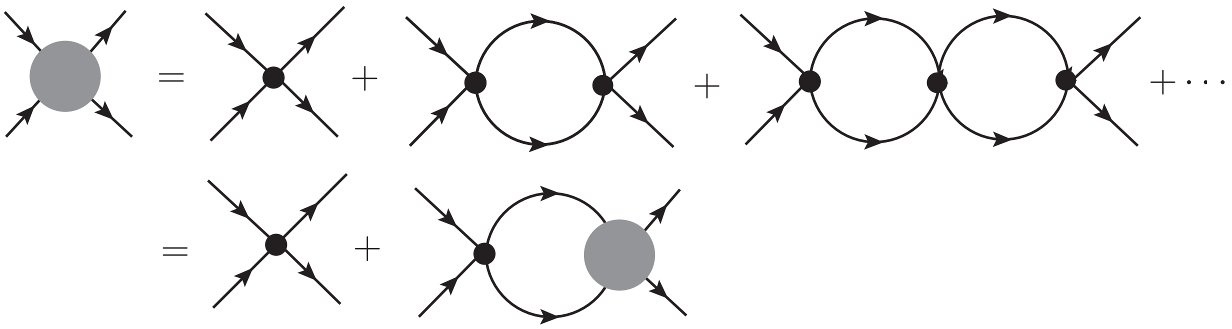

Figure 2.2: Lippmann-Schwinger equation for the scattering of particles in leading order of the local non-relativistic EFT.

In order to predict observables, the coupling constant must be renormalised and matched for a fixed Λ to an observable with the result that g_2 becomes a function of Λ, the running coupling constant. Explicitly, g_2 is renormalised by the constraint that the scattering length a is fixed:

$$-a \overset{!}{=} \lim_{k\to 0} f(\vec{k}\,' \leftarrow \vec{k}) = \lim_{E\to 0} \frac{\mu}{4\pi} \mathcal{A}_2(0) \ . \tag{2.31}$$

Then, the renormalised scattering amplitude becomes independent of the ultraviolet cutoff and one finds

$$\mathcal{A}_2(E+i\epsilon) = \frac{4\pi}{\mu} \frac{1}{-1/a + \sqrt{-(2\mu)E - i\epsilon}} \ . \tag{2.32}$$

The pole in the amplitude at $E_D = -\frac{1}{2\mu a^2}$ indicates the universal two-body bound, already mentioned in section 2.1.3.

At the end of this section, I would like to stress that the complete Λ-independence in the amplitude is accidental. In general, one expects only a suppressed Λ-dependence with E/Λ^2. But, in the scaling limit, the cutoff can be increased without bounds and at all energies the system can be treated in the EFT. Note however, that in real physical systems a natural cutoff is usually given by the inverse of the effective range $1/r_0$. In short, the EFT is appropriate only for physical properties at energy scales of $E < 1/r_0^2$.

2.2.3.2 Three-Body Scattering

The Lagrangian for the three-body sector now contains a three-body term. The description of three-boson scattering within the EFT in the scaling limit is rather intricate. In the centre-of-mass frame the 6-point Green's function in momentum space $\langle 0 | T(\psi\psi\psi\psi^\dagger\psi^\dagger\psi^\dagger) | 0 \rangle$ depends on 4 momentum vectors and 5 off-shell energies and such an solution of a integral equation in many variables is highly complicated.

At this point, one introduces an auxiliary dimer field. The new quantum field d, the dimer field, is a composite of two ψ's. The 6-point Green's function then reduces to a 4-point Greens function $\mathcal{A}_3 = \langle 0 | T(d\psi d^\dagger \psi^\dagger) | 0 \rangle$. A new Lagrangian, which involves the field d explicitly and is equivalent to the former Lagrangian in leading order, can be constructed and is written as

$$\mathcal{L}_3 = \psi^\dagger \big(i\frac{\partial}{\partial t} + \frac{\Delta}{2m}\big)\psi + \frac{g_2}{4} d^\dagger d - \frac{g_2}{4}\big(d^\dagger\psi\psi + \psi^\dagger\psi^\dagger d\big) - \frac{g_3}{36} d^\dagger d \psi^\dagger \psi \ . \tag{2.33}$$

Based on this Lagrangian, Figure 2.3 depicts in terms of Feynman diagrams the scattering equation for three bosons, in the case of elastic boson-dimer scattering.

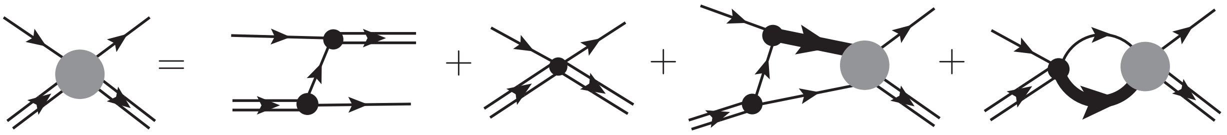

Figure 2.3: Three-body scattering rewritten in dimer-boson scattering.

The corresponding Feynman rules for the Lagrangian in equation (2.33) are collected in Figure 2.4. Note that, the Feynman propagator of the field d is naively just a constant, but the dimer can be split into two bosons. Thus, the full propagator is a sum over all loop diagrams which leads to the same integral equation as in the 2-body scattering apart from constants (see equation (2.28)). At the end, one has for the full dimer propagator with energy P_0 and momentum $\vec{P}$

$$iD(P_0,\vec{P}) = i\frac{32\pi}{mg_2^2}\left[\frac{1}{a} - \sqrt{-mP_0 + \vec{P}^2/4 - i\epsilon}\right]^{-1} . \tag{2.34}$$

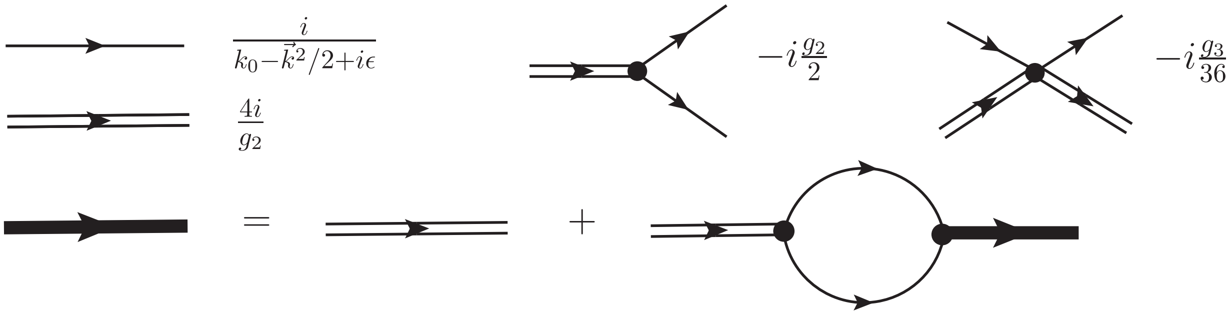

Figure 2.4: Feynman rules for Lagrangian in equation (2.33).

Using the Feynman rules with projection onto S-waves and with the help of the residue theorem, one finds in the centre-of-mass frame for the dimer-boson amplitude

$$\begin{aligned}\mathcal{A}_S(p,k;E) = {} & \frac{16\pi}{a}\left[\frac{1}{2pk}\ln\left(\frac{p^2+pk+k^2-E-i\epsilon}{p^2-pk+k^2-E-i\epsilon}\right) + \frac{H(\Lambda)}{\Lambda^2}\right] \\ & + \frac{4}{\pi}\int_0^\Lambda \mathrm{d}q\, q^2 \left[\frac{1}{2pq}\ln\left(\frac{p^2+pq+q^2-E-i\epsilon}{p^2-pq+q^2-E-i\epsilon}\right) + \frac{H(\Lambda)}{\Lambda^2}\right] \frac{\mathcal{A}_S(q,k;E)}{-\frac{1}{a} + \sqrt{\frac{3}{4}q^2 - E - i\epsilon}} .\end{aligned} \tag{2.35}$$

Here, p and k denote the absolute value of the incoming and the outcoming momenta, respectively and E is the energy. Since the original integral is again divergent, the integral has been regularised with the cutoff Λ. In order to match to observables and to compensate the Λ-dependence, the coupling constants must be renormalised. The cutoff dependence of g_3 is described in the function $H(\Lambda)/\Lambda^2 := -g_3/(9g_2^2 m)$. It can be shown, that $H(\Lambda)$ is a periodic function related to a UV renormalisation group limit cycle. H can be parametrised as

$$H(\Lambda) = \frac{\cos\left[s_0 \ln\left(\frac{\Lambda}{\Lambda *}\right) + \arctan\left(s_0\right)\right]}{\cos\left[s_0 \ln\left(\frac{\Lambda}{\Lambda *}\right) - \arctan\left(s_0\right)\right]} . \tag{2.36}$$

The scaling-violation parameter Λ_* is related to an observable in the three-body sector up to a multiplicative factor of $\exp(n\pi/s_0)$ with $n \in \mathbb{N}$, where s_0 is an universal constant. For identical bosons one finds $s_0 \approx 1.00624$.

We will see that the integral equation (2.35) yields roughly geometrically distributed three-body bound state energies, even for negative scattering lengths, where no two-body bound state exists. The existence of these bound states is called the Efimov effect and it is discussed in the next section 2.3 in more detail.

2.3 Efimov Effect

As mentioned in [29], Efimov published his studies about the three-nucleon system interacting through short-ranged interactions with the natural length scale l in 1970 [13]. For interactions with large scattering lengths $a \gg l$, he focused on the low-energy behaviour, i.e. $E \ll \hbar^2/(ml^2)$. In doing so, he discovered a sequence of roughly geometrically distributed bound state energies between $\hbar^2/(ml)^2$ and $\hbar^2/(ma)^2$. If the scattering length is increased, new bound states appear in the spectrum. For the unitary limit ($a \to \pm\infty$), the bound state energies are exactly geometrically distributed with an accumulation point at the threshold $E = 0$. Afterwards, the Efimov effect was formally proved by Amado and Noble in the following two years [30, 31]. Within the local EFT we will see that the Efimov effect is observed in the three-body scattering in the modern language of quantum field theory and that it is a manifestation of an UV renormalisation group limit cycle.

More than 30 years after the prediction of Efimov trimers, the first experimental evidence for these were found in a trapped gas of ultra-cold Cs atoms [14]. In this experiment, signatures in the three-body recombination rate for negative scattering lengths indicate the existence of trimer states. Their dependence on the scattering length was studied by tuning the scattering length by Feshbach resonances (see section 2.5.1.1). Since this pioneering experiment, a lot of progress was made and Efimov physics was observed in several experiments.

Evidence for Efimov trimers in 3-body recombination was also obtained in a balanced mixture of atoms in three different hyper-fine states of ^{6}Li [33, 34], in a mixture of Potassium and Rubidium atoms [35], and in an ultra-cold gas of ^{7}Li atoms [36]. In another experiment with Potassium atoms [37], two bound trimers were observed with energies compatible with the geometric prediction for Efimov states. Efimov states can also be observed as resonances in atom-dimer scattering. Such resonances have been seen with atom-dimer mixtures of Cs atoms [38] and of ^{6}Li atoms [39, 40]. The first direct observation of Efimov trimers of ^{6}Li atoms created by radio frequency association was recently reported by the Heidelberg group [41].

These experiments were carried out in a regime where the influence of the trap on the system could be neglected. However, it is to be expected that with experimental advances the trap frequencies can be increased and the trap itself could be used to modify and study internal properties of few-body systems.

2.3.1 Efimov Effect and local EFT

Within the local EFT the Efimov effect can be studied via the scattering amplitude of the three-body scattering. It turns out to be automatically related to the renormalisation group concept [6]. As in the two-body sector, poles in the scattering amplitude for negative energies signify the existence of a bound state with binding energy $E_T^{(n)}$. In order to extract the poles from the integral equation (2.35) one exploits that the amplitude factorises in the vicinity of a pole:

$$\mathcal{A}_S(p,q;E) \rightarrow \frac{\mathcal{B}^{(n)}(p)\mathcal{B}^{(n)}(q)}{E+E_T^{(n)}} \quad \text{as} \quad E \rightarrow -E_T^{(n)} \, . \tag{2.37}$$

Then, combining equations (2.35) and (2.37), the bound-state integral equation for the amplitude of Efimov states is found:

$$\begin{aligned}\mathcal{B}^{(n)}(p) = \frac{4}{\pi}\int_0^\infty & \mathrm{d}q \\ & q^2\left[\frac{1}{2pq}\ln\left(\frac{p^2+pq+q^2-E-i\epsilon}{p^2-pq+q^2-E-i\epsilon}\right)+\frac{H(\Lambda)}{\Lambda^2}\right]\left[-1/a+\sqrt{\frac{3}{4}q^2-E-i\epsilon}\right]^{-1}\mathcal{B}^{(n)}(q) \, .\end{aligned} \tag{2.38}$$

The values for E for which this homogeneous equation has solutions are the binding energies $(-E_T^{(n)})$ of the Efimov states. In fact the spectrum depends on two parameters determined by two observables. The first one is the scattering length a and the second one is the parameter Λ_* in the function $H(\Lambda)$ which is matched to reproduce some binding energy of a single Efimov trimer in the spectrum. The rest of the spectrum is then independent of the arbitrary cutoff Λ. It can be chosen as a root $\tilde{\Lambda}$ of the periodic function $H(\Lambda)$. $\tilde{\Lambda}$ is fixed only up to the multiplicative factors of $(e^{m\pi/s_0})$ with integer m. For a specific cutoff $\tilde{\Lambda}$, all Efimov states up to around the binding energy $|E_T^n| \leq \tilde{\Lambda}^2$ can then be calculated with equation (2.38) numerically. In order to compute more deeper bound Efimov states, the cutoff has to be increased, i.e. one chooses a larger root $\tilde{\Lambda}$ of the function $H(\Lambda)$. The spectrum for a fixed Λ_* is shown schematically as a function of $1/a$ in Figure 2.5.

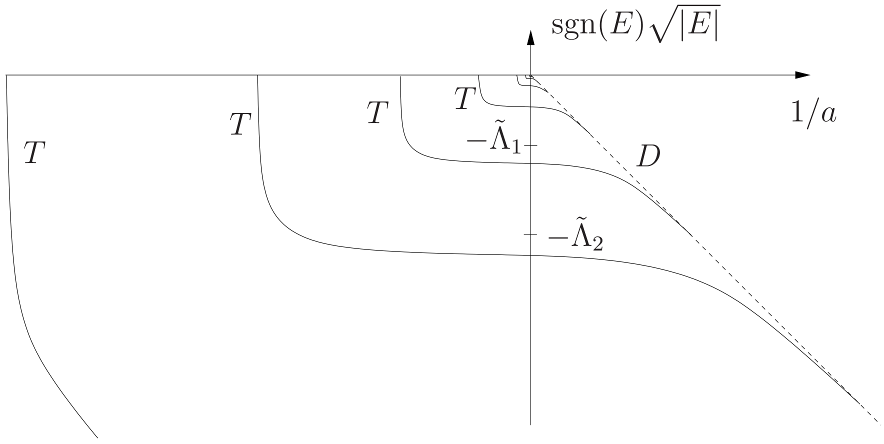

Figure 2.5: Efimov states T for a specific Λ_* as a function of $1/a$ with the dimer threshold D. The trimers are not drawn to scale. In fact, they scale with a factor of $e^{\pi/s_0} \approx 22.7$. With $\tilde{\Lambda}_1$ the deeper Efimov states below $\tilde{\Lambda}_1$ can not be found. Thus, a larger cutoff $\tilde{\Lambda}_2$ is necessary to determine the next Efimov state.

Note that the EFT describes systems in the scaling limit. The spectrum of a real physical system is restricted from below since all interactions have a finite range and therefore a natural length l. Exactly this additional scale restricts the scope of the theory. Hence, only Efimov trimers with energies $E_T \ll \hbar/(ml^2)$ are described correctly. Physical properties at higher binding energies depend on the details of the interaction beyond the EFT.

2.3.2 Efimov Effect with External Confinement

Before reviewing the solution of the three-body problem in a harmonic trap, it is worthwhile to inspect the confined two-body problem in the scaling limit.

I consider a two-body system confined by an isotropic harmonic oscillator. For simplicity, it is sensible to express all lengths in the oscillator length $b := \sqrt{\hbar/(m\omega)}$ with the mass m and the frequency ω. The dimensionless Jacobi coordinates (see appendix A) are defined by $\vec{s}_i^{(b)} := \vec{s}_i/b$. The contact interaction is parametrised with the regularised δ-distribution $\delta^{(3)}(\vec{s}_1^{(b)})\frac{\partial}{\partial s_1^{(b)}}s_1^{(b)}$. The coupling constant is related to the scattering length a, see [16]. Thus, the corresponding Hamiltonian in Jacobi coordinates reads

$$H = \hbar\omega\Big[-\frac{1}{2}\Delta_{\vec{s}_1^{(b)}} + \frac{1}{2}|\vec{s}_1^{(b)}|^2 + \sqrt{2}\pi\frac{a}{b}\delta^{(3)}(\vec{s}_1^{(b)})\frac{\partial}{\partial s_1^{(b)}}s_1^{(b)}\Big] . \tag{2.39}$$

The spectrum of this Hamiltonian has been determined by Busch et al. [17]. Only the spectrum for vanishing relative angular momentum is modified by the contact term and the energies E are given by solutions of

$$\frac{b}{a} = \sqrt{2}\frac{\Gamma\left(-\frac{E}{2\hbar\omega}+\frac{3}{4}\right)}{\Gamma\left(-\frac{E}{2\hbar\omega}+\frac{1}{4}\right)} . \tag{2.40}$$

Therefore, the spectrum is completely specified by the scattering length a. In principle, the scattering length could be extracted from a measurement of the energy spectrum. Note that a specification of the scattering length a is equivalent to specifying any energy of the spectrum. Both procedures determine the whole spectrum and both quantities can be used as an observable to renormalise the coupling constant in the effective theory.

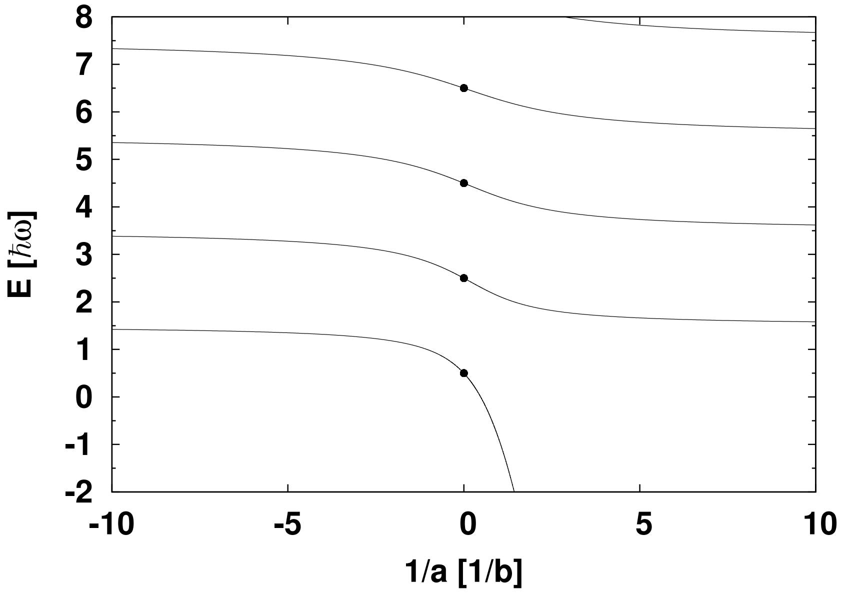

Figure 2.6: Spectrum of the two-body sector in the harmonic confinement as a function of $1/a$ [17]. The dots indicate the spectrum in the unitary limit $b/a \to 0$.

The spectrum is depicted in Figure 2.6. For $b/a \to -\infty$ the result is the spectrum of the oscillator without any contact interaction. This spectrum is lowered by $\Delta E = 1\ \hbar\omega$ in the unitary limit

$b/a \to 0$. For the limit $b/a \to +\infty$ the states are again lowered by $\Delta E = 1\ \hbar\omega$ apart from the ground state, of which the energy diverges to $-\infty$. Then again the oscillator spectrum is found with an additional infinitely deeply bound ground state.

For an axial-symmetric or an anisotropic harmonic oscillator potential the two-body energy spectra were derived analytically by Idziaszek et al. [42] and by Liang et al. [43], respectively.

The three-body sector is more complicated and the Hamiltonian cannot be solved in general. But for the unitary limit, solutions are published for bosons by Jonsell et al. [44] and for bosons and fermions by Werner et al. [18].

The most noteworthy point is that for the bosons there are two types of energy states for vanishing relative angular momentum $l = 0$. On the one hand, there are states for $|a|/b \to \infty$ with energies

$$E_{n,q} = \hbar\omega(s_{0,n} + 1 + 2q) \ , \tag{2.41}$$

with a non-negative integer q and the positive real, not integer solutions $s_{0,n}$ of the transcendental equation

$$+s_{0,n} \cos\left(\frac{\pi}{2} s_{0,n}\right) = \frac{8}{\sqrt{3}} \sin\left(\frac{\pi}{6} s_{0,n}\right) \ . \tag{2.42}$$

On the other hand, states of the second type are called Efimov-like. They belong to the single imaginary solution $s_{0,0} \approx 1.0062\ i$ of the transcendental equation. As for Efimov states, energies of these states depend on a three-body parameter R_t in addition to the scattering length $a/b \to \infty$. The energies of Efimov-like states are the solutions of the following equation:

$$\arg\left[\Gamma\left(\frac{1 + s_{0,0} - E/(\hbar\omega)}{2}\right)\right] = -|s_{0,0}| \ln(R_t/b) + \arg\left[\Gamma\left(s_{0,0} + 1\right)\right] \quad \mod \ \pi \ . \tag{2.43}$$

The spectrum of Efimov-like states is bounded neither from below nor from above. The scaling with the factor of about 22.7, known from the unconfined three-body system, can be observed for adjacent, large negative energies E_n, E_{n+1}:

$$\frac{E_n}{E_{n+1}} \sim (22.7)^2 \ . \tag{2.44}$$

2.4 Similarity Renormalisation Group

In 1990's, Glazek and Wilson [45, 46] as well as Wegner [47] developed independently the similarity renormalisation group approach (SRG). The first application to the nuclear many-body problem was published in 2007 by Bogner et al. [48]. I will exploit the SRG-transformation for the few-body sector of ^{4}He-atoms treated with the realistic ab-initio LM2M2 potential in section 5.

The motivation for the SRG approach is the strong intertwinement of high- and low-energy physics for strong short-ranged potentials in particular for potentials with a hard core. Due to this, the spectrum in shell-model calculations shows a strong cutoff dependence. Accordingly, only results with large cutoffs are reliable, but at the same time, the determination is then very time-consuming and elaborate. A possible expedient is the SRG approach which decreases the correlations at the expense of introducing more-particle interactions.

Wegner [47] formulates the SRG evolution as a flow equation of the Hamiltonian. The SRG evolution is a unitary transformation of the Hamiltonian with a flow parameter s and can be written as

$$H(s) = U(s) H U^\dagger(s) \ . \tag{2.45}$$

Owing to unitarity, the transformation matrices $U(s)$ and $U^\dagger(s)$ fulfil the following relation:

$$0 = \frac{\mathrm{d}}{\mathrm{d}s} 1 = \frac{\mathrm{d}}{\mathrm{d}s}\left(U(s)U^\dagger(s)\right) = \underbrace{U'(s)U^\dagger(s)}_{\eta(s)} + \underbrace{U(s)U^{\dagger\prime}(s)}_{\eta^\dagger(s)} \ . \tag{2.46}$$

Therefore, the flow equation of the Hamiltonian is just given by

$$\frac{\mathrm{d}}{\mathrm{d}s} H(s) = \left[\eta(s), H(s)\right]_- \ . \tag{2.47}$$

Additionally, the generator $G(s)$ is defined by

$$\eta(s) = \left[G(s), H(s)\right]_- \ . \tag{2.48}$$

In our application, only the potential should be transformed and the kinetic energy is to be kept constant. Accordingly, the kinetic energy can be used as the generator $G(s) = T$. Hence, one has with $H(s) = T + V(s)$

$$H'(s) = V'(s) = \left[\left[T, V(s)\right]_-, T + V(s)\right]_- \ . \tag{2.49}$$

At the end, I would like to point out that many-body potentials are induced and that with the kinetic energy as generator the correlation is suppressed in the evolution. The latter can be seen from writing equation (2.49) in momentum space:

$$\langle \vec{p} | V'(s) | \vec{k} \rangle = \frac{\mathrm{d}}{\mathrm{d}s} V(s,p,k) \tag{2.50}$$

$$= -V(s,p,k)\frac{(|\vec{p}|^2 - |\vec{k}|^2)^2}{4m^2} + \int_0^\infty \mathrm{d}q\, q^2 V(s,p,q) V(s,q,k) \frac{|\vec{p}|^2 + |\vec{k}|^2 - 2q^2}{2m} \ . \tag{2.51}$$

The second term is suppressed with respect to the first one for significantly different momenta p and k for the physical potential. Neglecting this term, the solution of the differential equation (2.51) is given by

$$V(s,p,k) = V(0,p,k) \exp\left(-s\frac{(p^2 - k^2)^2}{4m^2}\right) \ . \tag{2.52}$$

Hence, the correlations of different energy scales are suppressed approximately exponentially. For details see [49].

Within the occupation number formalism with creation operators $a_i^{(\dagger)}$ and annihilation operators a_i, the induction of higher-body potentials can be seen explicitly in the flow equation. For instance, typical terms occurring in equation (2.49) for 2-body potentials are

$$V^{(2)}_{ijkl} V^{(2)}_{pqrs} \left[a_i^\dagger a_j^\dagger a_k a_l, a_p^\dagger a_q^\dagger a_r a_s\right]_- \ . \tag{2.53}$$

These commutators have contributions of three-body interactions terms $a_i^\dagger a_j^\dagger a_k^\dagger a_l a_m a_n$. Consequently, many-body terms are induced by the evolution.

Finally we make a small comment on the physical dimension of s: The dimension of the evolution parameter s is $[s] = [E]^{-2}$. Typically, a new parameter $\Lambda^{-4} = s/(4m^2)$ is defined, which then has the dimension of a momentum $[\Lambda] = [p]$. In section 5, this parameter Λ will be used as flow parameter instead of s.

2.5 Experimental Techniques

In this section, I briefly discuss experimental techniques, which are used to investigate the physical systems considered in sections 4 and 5. This overview should convey the principle and issues of modern experiments for atoms with resonant interactions in external confinements and for ^{4}He clusters.

2.5.1 Study of Atoms with Resonant Interactions in Traps

A review about experiments with ultra-cold atoms at Feshbach resonances is published by Chin et al. [50]. An overview about experiments with Efimov physics is given in [15]. Here, I just summarise some relevant experimental techniques.

2.5.1.1 Feshbach Resonances

Due to Feshbach resonances cold atoms are the perfect systems to investigate universal behaviour. The Feshbach resonances allow to modify the atom-atom interactions with external magnetic fields. Therefore, the scattering length a can be tuned and the universal region is accessible for experiments. The effect of Feshbach resonances can be illustrated in a two-channel model as in the left panel of Figure 2.7.

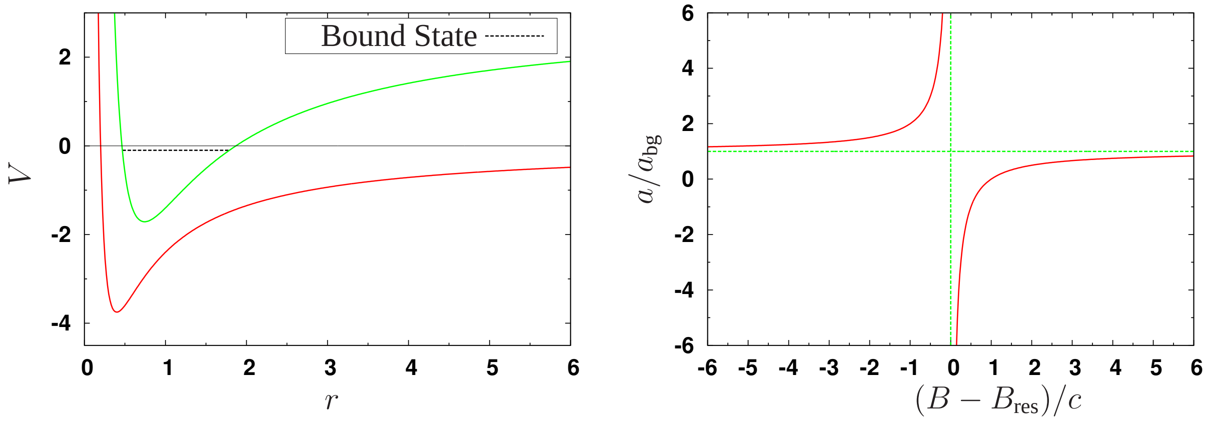

Figure 2.7: **Left panel**: Two-channel model of Feshbach resonances. With the magnetic field B, the open (red) and closed (green) channel can be tuned. **Right panel**: Scattering length a as a function of B in the vicinity of the Feshbach resonance at B_{res}

The effect requires at least an open and a closed channel which are only weakly coupled. The resonance occurs when a binding energy of the closed channel and the threshold of the open channel coincide. This coincidence can be generated by an external magnetic field if the magnetic moments of the two channel states differ. For instance, this is the case for different spin structures in the two channels.

The corresponding scattering length is depicted in the right panel of Figure 2.7. For narrow Feshbach resonances the dependence of a from B can be approximately described in the vicinity of the resonance at the magnetic field B_{res} by

$$a(B) \approx a_{\text{bg}} \left(1 + \frac{c}{B - B_{\text{res}}} \right) \, . \tag{2.54}$$

Here, c denotes the width of the resonance and a_{bg} is the background scattering length far away from the resonance.

For experiments, the width is a crucial quantity, since it signifies the necessary resolution for the magnetic fields. The widths of s-wave resonances are often larger than 1 G. For higher partial waves (e.g. d-or g-waves resonances) a resolution in the order of mG is usually required.

2.5.1.2 Traps and Cooling

In atomic physics, various techniques for realising a confinement by traps are available. To start with, there are magnetic or magnetic-optical traps (MOT). However, in many experiments the lowest atomic states should be studied and these states are high-field seeking and cannot be trapped magnetically. Furthermore, the scattering length is to be tuned with external magnetic fields, which would influence the trap field. Thus optical dipole traps are usually used in such experiments. But they have typical depths below 1 mK and this require strong cooling which can be achieved more efficiently in magnetic traps. Consequently, MOT's are often utilised to precool the atomic gases. Subsequently, the atoms are loaded in optical dipole traps to cool the system to the operating temperature of the experiment.

In general, optical traps are realised by several counter-propagating laser beams. It is possible to tailor geometries specially designed for specific experiments. The trap potential is caused by the dispersive interaction between the induced dipole moments in the neutral atoms and the intensity gradient of the light field. A review of experimental techniques and theoretical models of optical dipole traps can be found in Grimm et al. [51].

In order to study typical phenomena of Efimov physics the system has to be cooled to few 10 nK. For few 100nK thermodynamical effects prevent the necessary resolution and the interesting phenomena are obscured. These low temperatures are accessible only by combination of different techniques.

With the so-called Doppler cooling, temperatures down to few 100 μK can be achieved. The basic principle is the excitation of the atoms with an oriented laser beam. The subsequent spontaneous emission is not oriented and in average the atoms loose kinetic energy. A theoretical limit is determined by the Doppler limit, which is connected to the width of the cooling transition.

Following this, the Sisyphus cooling is a possible method to achieve the recoil limit of the laser beam of few 100 nK [52]. It exploits the Zeeman sub-levels of the atoms. With two laser beams, which propagate in opposite direction and are linearly polarised perpendicular to each other, an interference pattern of alternating clockwise and counterclockwise circular polarised light can be generated. Along this pattern, the Zeeman sub-levels change their energies and switch their position. Metaphorically, the energy levels move uphill and back to a valley. In average, more electrons at the hill are optically pumped in an excited state and fall back in a valley. Thus the atom looses energy and is cooled.

Finally, in order to achieve the 10 nK region, the approach of forced evaporative cooling is used. Originally proposed by Hess [53], the principle is that atoms confined in a trap with threshold E_{sh} could generate constituents with energy $E > E_{\text{sh}}$ by collisions. These high-energetic atoms are allowed to evaporate out of the trap. The remaining atoms rethermalise and the temperature drops. The evaporation is enhanced by rf-induced spin flips [54], with slowly lowering of the depth of the trap potential [55], or with a combination of both. The lowering of the depth is called the direct forced evaporation.

2.5.2 Investigation of Helium Clusters by Diffraction

In section 5, I will study clusters of ^{4}He-atoms within the present shell-model approach. These clusters eluded an experimental investigation for a long time. Common experimental techniques in molecular physics like spectroscopy with microwaves, infrared or visible light as well as electron scattering disturb the investigated system. As a consequence, weakly bound systems are destroyed if such techniques are used.

A breakthrough was made in 1994 by Schöllkopf et al. [21]. Improved measurements and even dimer binding energies were published in 2000 by Grisenti et al. [22,56]. The detection of clusters is based on diffraction off a transmission grating.

The schematic construction of the experiments is depicted in Figure 2.8. A nearly mono-energetic, supersonic beam of helium atoms is produced by expanding the ^{4}He gas through a 5-μm-diameter nozzle. The temperature and pressure of the ^{4}He source can be varied and hereby the de Broglie wavelength of the ^{4}He atoms from 0.56 Å to 1.81 Å. Two 10 μm slits in the beam arrange a sufficient spatial coherence. The beam is diffracted at a perpendicular silicon nitride grating which has a period of $d = 200$ nm. The diffraction patterns are detected with a rotatable mass spectrometer behind the transmission grating and collimation by another slit.

By virtue of the narrow velocity distribution, the experiment shows a high selectivity in cluster sizes. Because of this narrow distribution, all clusters nearly have the same velocity v. The corresponding de Broglie wavelength λ of a cluster with N constituents is given with the mass of Helium atoms m_{He} by

$$\lambda = \frac{2\pi\hbar}{N m_{\text{He}} v} \ . \tag{2.55}$$

The diffraction angles for a beam are described in the Fraunhofer approximation by

$$\sin(\theta) \approx \frac{n}{d} \frac{2\pi\hbar}{N m_{\text{He}} v} \ . \tag{2.56}$$

With this formula, the mass of the clusters ($N m_{\text{He}}$) are determined from the diffraction angle.

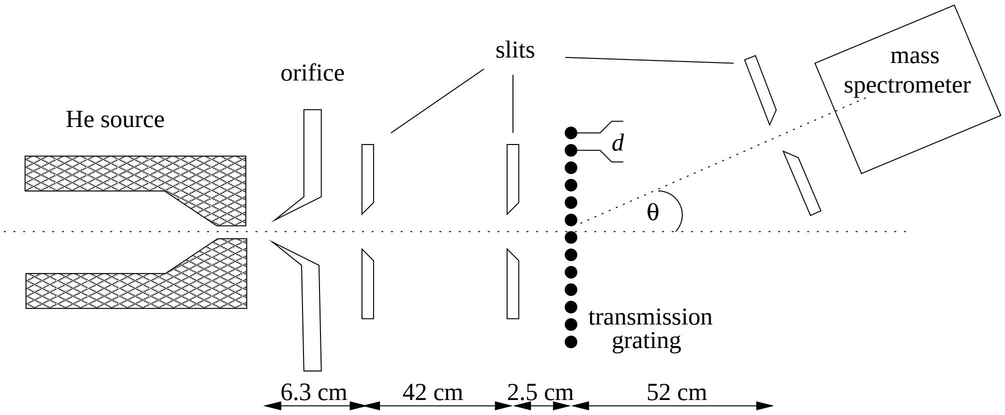

Figure 2.8: Schematic construction of the diffraction experiment designed by Schöllkopf et al. [21].

Chapter 3

Shell-Model Approach

Historically, shell models were introduced in order to explain the shell structure of the electron configuration in atoms. As a first approximation, the electrons are assumed to be negatively charged particles moving independently in the field of the positively charged atomic nucleus (coulomb potential) complemented with a potential describing the average electron-electron repulsion, known as the Hartree-Fock potential of the atom mean field approximation. In this approximation the many-electron system is described by a single Slater-determinant of the single-particle orbitals. In order to account for correlations the remaining electron-electron interaction can e.g. be treated by diagonalisation of the corresponding Hamiltonian in an appropriate finite basis spanned by the single-particle orbitals.

In nuclear physics, shell models were suggested after the discovery of the so-called magic numbers in the separation energies of neutrons and protons. In 1963, M. G. Mayer and J. H. D. Jensen were awarded the Nobel Prize for their studies concerning the nuclear shell structure. In contrast to atomic physics, there exists a priori no strong central potential such as the Coulomb potential of the central nucleus in atoms. But such a central mean-field potential can be imagined as being built by the nucleons themselves and can again be constructed by the Hartree-Fock method. Traditionally in treating the many-nucleon problem, only configurations spanned by a finite set of active valence orbitals were considered. In the 1990's, work in so-called no-core shell models [57] became feasible. In such models, all A constituents in a A-particle nucleus are treated as active. The Hamiltonian is then diagonalised in a model space e.g. spanned by a finite harmonic oscillator basis. Nowadays, with realistic nucleon-nucleon interactions the ab-initio no-core shell model is applicable for light nuclei up to $A = 16$ [58]. For this purpose, the realistic hard-core short-ranged potentials have to be transformed with unitary operators and this is done e. g. with the Okubo-Lee-Suzuki procedure [59] [60] or the similarity renormalisation group (see section 2.4). The principle idea of shell models and no-core shell models is the basis on which I shall treat systems of resonantly interacting atoms in an external confinement and also ”free space” ^{4}He-atom clusters.

In this thesis only non-relativistic systems are studied. Accordingly, the starting point is the Hamiltonian consisting of the kinetic terms and interaction potentials. Here, I will concentrate on bosons with spin 0. In section 4 I consider systems with resonant interactions in an external confinement. For this purpose, the local EFT described in section 2.2.3 is used. Thus, the interaction potentials are just two- and three-body contact interactions. As such, the Hamiltonian is ill-defined and has to be regularised. The external confinement is idealised by an isotropic harmonic oscillator potential (HOP).

In a second application, the binding energies of ^{4}He-atom clusters without any confinement are to be determined in section 5. The interaction between helium atoms is described by a two-body ab-initio potential, the so-called LM2M2. Alternatively, an effective potential with schematic two-body and three-body parts is used. These potentials are transformed with the similarity-renormalisation-group (SRG) method (see section 2.4) in order to circumvent specific problems associated with the short range repulsion. In all situations I consider at most three-body interactions. All potentials considered are spherically symmetric. Hence, the relevant Hamiltonian is of the form

$$H = \sum_{i=1}^{A} \left(\frac{|\vec{p}_i|^2}{2m} + \frac{1}{2} m\omega^2 |\vec{x}_i|^2 \right) + \sum_{i<j}^{A} V_{ij} + \sum_{i<j<k}^{A} W_{ijk} \, . \tag{3.1}$$

For the application without external confinement the oscillator frequency can simply be set to $\omega = 0$. All A particles have the same mass m. V_{ij} denotes the interaction between particle i and j at the relative position $\vec{x}_{i,j} := \vec{x}_i - \vec{x}_j$ and with momentum $\vec{p}_{i,j} = -i\hbar\vec{\nabla}_{\vec{x}_{i,j}}$. Likewise, W_{ijk} is the three-body interaction between particles i, j and k.

In general, the spectrum of such a Hamiltonian cannot be found analytically and numerical methods are necessary. Suitable methods for such a Hamiltonian are shell-model approaches. In contrast to the no-core shell-model calculations in nuclear physics, I consider only bosons instead of fermions. The first step is to construct a basis for the Hilbert space. Thereafter, this infinite-dimensional basis is truncated by a constraint motivated physically and the model space is then the linear hull of the finite basis. Automatically, this implies a regularisation of the Hamiltonian. Thirdly, all matrix elements of the Hamiltonian are determined in the model space. Finally, the eigenvalues of the Hamiltonian are found numerically by diagonalisation.

In detail, I have used two different methods, both based on spherical oscillator functions. On the one hand, I work in the so-called J-scheme in Jacobi coordinates. On the other hand, I use the so-called M-scheme in one-particle coordinates. In the next section 3.1 the former procedure is explained. Subsequently, I outline the latter in section 3.2. Both approaches are compared in section 3.3.

3.1 J-Scheme Shell Model in Jacobi Coordinates

To begin with, I exploit the possibility to decouple the centre-of-mass dynamics for the oscillator potential. For this purpose, the Hamiltonian (3.1) is rewritten in Jacobi coordinates (see appendix A). Since one is only interested in the internal structure, the trivial centre-of-mass dynamics is omitted. By this procedure the A-particle problem is reduced to a $(A-1)$-particle problem for the internal excitations of the system; the uninteresting centre of mass excitations being separated. However matrix elements of the interactions terms will be more expensive to determine.

In a second step, a basis has to be determined for the Hilbert space of A identical bosons. The ”building blocks” for this basis are the spherical oscillator functions

$$\langle \vec{\rho} | nlm \rangle_b := \phi^b_{nlm}(\vec{\rho}) = \frac{1}{b^{3/2}} \phi^1_{nlm}(\vec{\rho}/b) \tag{3.2}$$

$$= \frac{1}{b^{3/2}} \langle \vec{\rho}/b | nlm \rangle = \frac{1}{b^{3/2}} R_{nl}(\rho/b) Y_{lm}(\hat{\rho}) \, . \tag{3.3}$$

For brevity, I shall write ϕ_{nlm} instead of ϕ^1_{nlm}. They are the eigenfunctions of a one-particle Hamiltonian H_{osc} with the isotropic harmonic oscillator potential:

$$H_{\text{osc}}\phi^b_{nlm}(\vec{\rho}) = \Big(-\frac{\hbar^2}{2m}\Delta_\rho + \frac{1}{2}m\omega^2|\vec{\rho}|^2\Big)\phi^b_{nlm}(\vec{\rho}) = \hbar\omega\Big(2n+l+\frac{3}{2}\Big)\phi^b_{nlm}(\vec{\rho})\ , \tag{3.4}$$

where ω is the oscillator frequency and $b := \sqrt{\hbar/(m\omega)}$ the oscillator length with the mass m of the particle. Here $Y_{lm}(\hat{\rho})$ are the spherical harmonics and the radial functions are explicitly given by

$$R_{nl}(r) = \mathcal{N}^{(\text{norm})}_{nl}\ r^l\ e^{-r^2/2}\ L^{(l+1/2)}_n(r^2)\ , \tag{3.5}$$

with the generalised Laguerre polynomials $L^{(l+1/2)}_n$ and the normalisation factor

$$\mathcal{N}^{(\text{norm})}_{nl} = \sqrt{\frac{(2n)!!2^{l+2}}{(2(n+l)+1)!!\sqrt{\pi}}}\ . \tag{3.6}$$

A possible basis describing the internal dynamics of the A-particle system in Jacobi coordinates simply consists of the product of $(A-1)$ oscillator functions in the Jacobi coordinates $\vec{s}^{(b)}_i = \vec{s}_i/b$:

$$\Big\{\bigotimes_{i=1}^{A-1} R_{n_i l_i}(s^{(b)}_i)Y_{l_i m_i}(\hat{s}_i)\Big\}\ . \tag{3.7}$$

However, an additional conservation law can be exploited. Since only problems with central potentials are addressed, the total angular momentum is conserved. Hence, it is worthwhile to work in a basis of coupled spherical harmonics which are eigenfunctions of the total angular momentum L. The quantum theory of angular momenta is described in detail in [61]. The expansion coefficients for the coupling are generically given by the Clebsch-Gordan coefficients $C^{LM}_{l_1m_1l_2m_2}$:

$$\big[Y_{l_1}(\hat{s}_1)\otimes Y_{l_2}(\hat{s}_2)\big]^L_{M=m_1+m_2} = \sum_{m_1,m_2} C^{LM}_{l_1m_1l_2m_2}Y_{l_1m_1}(\hat{s}_1)Y_{l_2m_2}(\hat{s}_2)\ . \tag{3.8}$$

The basis with the uncoupled spherical harmonics I shall call the M-scheme, because the product functions are eigenfunctions of the projections $\hat{l}_{3,i}$ with the quantum numbers m_i. In contrast, the coupled spherical harmonics belong to the so-called J-scheme, because the total angular momentum is a conserved quantum number and this is often called J. In this case, the basis is given by

$$\Big\{\big[\cdots\big[\big[R_{n_1l_1}(s^{(b)}_1)Y_{l_1}(\hat{s}_1)\otimes R_{n_2l_2}(s^{(b)}_2)Y_{l_2}(\hat{s}_2)\big]^{L_{12}}\otimes R_{n_3l_3}(s^{(b)}_3)Y_{l_3}(\hat{s}_3)\big]^{L_{123}}\otimes\cdots\big]^L_M\Big\}\ . \tag{3.9}$$

Since the angular momentum operator $\vec{L}$ is a generator of a symmetry transformation (rotations), the matrix elements are independent of M. Therefore, this quantum number is suppressed in the following.

This basis is the general basis for a physical system of A distinguishable particles. In the case of A identical bosons, the basis has to be symmetric under permutations of the constituents. In single particle coordinates the construction of a symmetric basis is trivial, but in the J-scheme in Jacobi coordinates it is more involved. The symmetric basis for the model space can be constructed iteratively starting from the symmetric basis for two particles. In the next section 3.1.1 this approach is outlined, see also [16] and [62]. Based on this, the Hamiltonian matrix elements can be calculated as outlined in section 3.1.3. In order to illustrate the procedure, the prescription is sketched in section 3.1.4 as a flow diagram.

3.1.1 Symmetric Basis

The iterative procedure starts with the construction of unnormalised symmetric states $\widetilde{\phi^{(2)}}_{nlm}(\vec{s}_1^{(b)})$ for the two-body sector. For this purpose I define the operator $P^{(2)} = (1 + T_{12})$ with the transposition T_{ik} between body i and k. This operator maps a two-body state ϕ to a unnormalised, symmetric state $\widetilde{\phi^{(2)}}$. Thus, one has for two particles

$$P^{(2)}\phi_{nlm}(\vec{s}_1^{(b)}) = \phi_{nlm}(\vec{s}_1^{(b)}) + \phi_{nlm}(-\vec{s}_1^{(b)}) = \begin{cases} 0 & \text{for } l \text{ odd,} \\ 2\phi_{nlm}(\vec{s}_1^{(b)}) & \text{for } l \text{ even,} \end{cases} =: \widetilde{\phi^{(2)}}_{nlm}(\vec{s}_1^{(b)}) \ . \tag{3.10}$$

Thus, an orthonormal basis for two particles with multi-index $\alpha(= nlm)$ is given by

$$\overline{\phi^{(2)}}_{\alpha}(\vec{s}_1^{(b)}) = \frac{1}{2}\,\widetilde{\phi^{(2)}}_{nlm}(\vec{s}_1^{(b)}) = \phi_{nlm}(\vec{s}_1^{(b)}) \quad \text{for } l \text{ even.} \tag{3.11}$$

In the next step, from the orthonormal two-body states the angular-momentum coupled mixed-symmetric three-body states are constructed as

$$\phi^{(3)}_{\text{MS}}(\alpha, n, l, L) = \left[\overline{\phi^{(2)}}_{\alpha} \otimes \phi_{nl}\right]^{L} . \tag{3.12}$$

Analogous to $P^{(2)}$ for $A = 2$, a map on the symmetric, unnormalised A-particle states is given by the operator

$$\begin{aligned} P^{(A)} &= (1 + T_{1A} + \dots + T_{(A-1)A})P^{(A-1)} \ , & (3.13) \\ &= (1 + \sum_{i=1}^{A-2} T_{(A-1)i}T_{(A-1)A}T_{i(A-1)} + T_{(A-1)A})P^{(A-1)} \ . & (3.14) \end{aligned}$$

With $P^{(A)}$ it is possible to calculate the transformation matrix $C^{(A-1)\to A}_{\text{sym}}$ from mixed-symmetric A-body states to (unnormalised) symmetric A-body states. Its matrix elements are given by the scalar product

$$C^{(A-1)\to A}_{\text{sym}}[z; \alpha', n_2', l_2', L'] := \left\langle \left[\overline{\phi^{(A-1)}}_{\alpha'} \otimes \phi_{n_2'l_2'}\right]^{L'} \middle| \left[\widetilde{\phi^{(A)}}_{z}\right] \right\rangle , \tag{3.15}$$

with multi-indices α' and z denoting the mixed-symmetric A-body state $\left[\overline{\phi^{(A-1)}}_{\alpha'} \otimes \phi_{n_2'l_2'}\right]^{L'}$ and the symmetric A-body state $\widetilde{\phi^{(A)}}_{z}$, respectively. This can be written as

$$\begin{aligned} &C^{(A-1)\to A}_{\text{sym}}[z; \alpha', n_2', l_2', L'] \\ &\quad = \left\langle \left[\overline{\phi^{(A-1)}}_{\alpha'} \otimes \phi_{n_2'l_2'}\right]^{L'} \middle| P^{(A)} \middle| \left[\overline{\phi^{(A-1)}}_{\alpha} \otimes \phi_{n_2 l_2}\right]^{L} \right\rangle , & (3.16) \\ &\quad = \left\langle \left[\overline{\phi^{(A-1)}}_{\alpha'} \otimes \phi_{n_2'l_2'}\right]^{L'} \middle| (1 + (A-1)T_{(A-1)A}) \middle| \left[\overline{\phi^{(A-1)}}_{\alpha} \otimes \phi_{n_2 l_2}\right]^{L} \right\rangle , & (3.17) \end{aligned}$$

where $z = \{\alpha, n_2, l_2, L\}$.

Our goal is to construct an orthonormal basis of symmetric A-body states $\overline{\phi^{(A)}}_{\omega}$. It is achieved by diagonalisation of the non-negative definite symmetric norm matrix

$$\mathcal{N}[z'; z] = \left\langle \widetilde{\phi^{(A)}}_{z} \middle| \widetilde{\phi^{(A)}}_{z'} \right\rangle . \tag{3.18}$$

This yields the diagonal matrix D of non-negative eigenvalues:

$$D = O \cdot \mathcal{N} \cdot O^T \ . \tag{3.19}$$

Vanishing eigenvalues do not correspond to linearly independent symmetric states and corresponding eigenstates are eliminated. Thus, we find a (non-square) transformation matrix B_{sym} from mixed-symmetric A-body states to orthonormal symmetric states:

$$B_{\text{sym}}^{(A-1)\to A}[\omega;\alpha',n_2',l_2',L'] = \frac{1}{\sqrt{D[\omega;j]}} O[j;z] C_{\text{sym}}^{(A-1)\to A}[z;\alpha',n_2',l_2',L'] \ , \tag{3.20}$$

where a sum over j and z with non-vanishing $D(w;j)$ is implied. Accordingly, the orthonormal basis of symmetric states is given by

$$\left|\overline{\phi^{(A)}}_{\omega}\right\rangle = B_{\text{sym}}^{(A-1)\to A}[\omega;\alpha,n_2,l_2,L] \left|\left[\overline{\phi^{(A-1)}}_{\alpha} \otimes \phi_{n_2 l_2}\right]^{L}\right\rangle \ . \tag{3.21}$$

In this way the orthonormal, symmetric states can be found iteratively. However, the determination of the matrix elements in equation (3.17) is not trivial, see in the next section 3.1.2.

3.1.2 Explicit calculation of $C_{\text{sym}}^{(A-1)\to A}$

The explicit calculation of $C_{\text{sym}}^{(A-1)\to A}$ involves a Talmi-Moshinsky transformation [63] and a change in the coupling scheme [61]. Equation (3.17) for $(A-1) \to A$ can be rewritten with the known transformation $B_{\text{sym}}^{(A-2)\to(A-1)}$ as

$$\begin{aligned} &C_{\text{sym}}^{(A-1)\to A}[\alpha,n_2,l_2,L;\alpha',n_2',l_2',L'] = \\ &\qquad B_{\text{sym}}^{(A-2)\to(A-1)}[\alpha;\gamma,n_1,l_1,L_\alpha] B_{\text{sym}}^{(A-2)\to(A-1)}[\alpha';\gamma',n_1',l_1',L'_{\alpha'}] \\ &\left\langle \left[\left[\overline{\phi^{(A-2)}}_{\gamma'}^{L'_{\gamma'}} \otimes \phi_{n_1',l_1'}\right]^{L'_{\alpha'}} \otimes \phi_{n_2' l_2'}\right]^{L'} \middle| (1+(A-1)T_{(A-1)A}) \middle| \left[\left[\overline{\phi^{(A-2)}}_{\gamma}^{L_\gamma} \otimes \phi_{n_1,l_1}\right]^{L_\alpha} \otimes \phi_{n_2 l_2}\right]^{L} \right\rangle \ . \end{aligned} \tag{3.22}$$

In order to calculate matrix elements of the operator $T_{(A-1)A}$, a transformation from the standard Jacobi coordinates $\vec{s}^{(b)}_{A-2}$ and $\vec{s}^{(b)}_{A-1}$ to new coordinates $\vec{\lambda}$ and $\vec{\mu}$ is performed (see Figure 3.1). It is an orthogonal transformation $\mathbb{R}^6 \to \mathbb{R}^6$ defined by

$$\begin{pmatrix} -\vec{\lambda} \\ \vec{\mu} \end{pmatrix} = \begin{pmatrix} \sqrt{\frac{A-2}{2(A-1)}} & -\sqrt{\frac{A}{2(A-1)}} \\ \sqrt{\frac{A}{2(A-1)}} & \sqrt{\frac{A-2}{2(A-1)}} \end{pmatrix} \cdot \begin{pmatrix} \vec{s}^{(b)}_{(A-2)} \\ \vec{s}^{(b)}_{(A-1)} \end{pmatrix} \ . \tag{3.23}$$

In the new coordinates, the operator $T_{(A-1)A}$ is diagonal and its matrix elements can be determined easily. In particular, the action of $T_{(A-1)A}$ on $\phi_{n_\lambda l_\lambda}(\vec{\lambda})$ is just the multiplication with the factor $(-1)^{l_\lambda}$.

First, however, the transformations of the coupled oscillator functions must be determined. For this purpose, the coupling scheme is changed by means of Wigner's 6j symbols [61]. Following this, the Talmi-Moshinsky transformation is exploited in the new coupling scheme. Details about Talmi-Moshinsky transformations are summarised in appendix B.

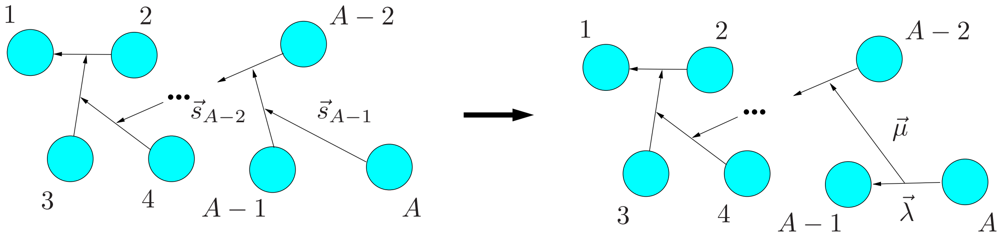

Figure 3.1: Talmi transformation from coordinates $\vec{s}^{(b)}_{(A-1)}$ and $\vec{s}^{(b)}_{(A-2)}$ to coordinates $\vec{\lambda}$ and $\vec{\mu}$.

Finally, the transformation can be written as

$$\begin{aligned}
&\Big[\big[\overline{\phi^{(A-2)}}^{L_\gamma}_{\gamma} \otimes \phi_{n_1,l_1}(\vec{s}^{(b)}_{(A-2)})\big]^{L_\alpha} \otimes \phi_{n_2 l_2}(\vec{s}^{(b)}_{(A-1)})\Big]^{L} = \\
&\qquad \sum_{L_{12}} (-1)^{L_\gamma+l_1+l_2+L} \sqrt{(2L_{12}+1)\,(2L_\alpha+1)} \begin{Bmatrix} L_\gamma & l_1 & L_\alpha \\ l_2 & L & L_{12} \end{Bmatrix} \\
&\sum_{\substack{l_\lambda,n_\lambda \\ l_\mu,n_\mu}} \Big(-1\Big)^{l_\lambda} \big\langle n_\lambda l_\lambda, n_\mu l_\mu; L_{12} \big| n_1 l_1, n_2 l_2 \big\rangle_{\frac{A}{A-2}} \Big[\overline{\phi^{(A-2)}}^{L_\gamma}_{\gamma} \otimes \big[\phi_{n_\lambda l_\lambda}(\vec{\lambda}) \otimes \phi_{n_\mu l_\mu}(\vec{\mu})\big]^{L_{12}}\Big]^{L} \,, \qquad (3.24)
\end{aligned}$$

with the Brody-Moshinsky brackets $\big\langle n_\lambda l_\lambda, n_\mu l_\mu; L_{12} \big| n_1 l_1, n_2 l_2 \big\rangle_{\frac{A}{A-2}}$. The transformation is stored in the matrix with elements

$$\begin{aligned}
&M^{(12)}[\alpha', n_2', l_2', L; \gamma, n_\lambda, l_\lambda, n_\mu, l_\mu, L_{12}] = \\
&\qquad \Big\langle \Big[\overline{\phi^{(A-2)}}^{L_\gamma}_{\gamma} \otimes \big[\phi_{n_\lambda l_\lambda} \otimes \phi_{n_\mu l_\mu}\big]^{L_{12}}\Big]^{L} \Big| \big[\overline{\phi^{(A-1)}}_{\alpha'} \otimes \phi_{n_2' l_2'}\big]^{L} \Big\rangle \,. \qquad (3.25)
\end{aligned}$$

In this way an orthonormal, symmetric basis $\overline{\phi^{(A)}}$ can be constructed in the J-scheme with Jacobi coordinates. In shell models, the next step is to truncate the basis and to determine all elements of the Hamiltonian in this finite basis.

3.1.3 Model Space and Elements of the Hamiltonian

Since solutions in the full Hilbert space are not accessible in general, a subspace, the model space is built. Here, the Hilbert space is restricted with the cutoff parameter N to the model space consisting of the linear hull of oscillator states $\{\bigotimes_{i=1}^{A-1} \phi_{n_i l_i m_i}(\vec{s}^{(b)}_i)\}$ with the energy eigenvalues $\sum_{i=1}^{A-1} \hbar\omega(2n_i + l_i + \frac{3}{2}) \leq \hbar\omega(N + (A-1)\frac{3}{2})$ for the unperturbed harmonic oscillator. Because the energy eigenvalues are independent of m_i, it does not matter, whether coupled or uncoupled wave functions are considered. Both model spaces are identical. Of course, only symmetric states are considered for identical bosons.

In the model space the matrix elements for the Hamiltonian are required. The Hamiltonian in equation (3.1) can be written in Jacobi coordinates without the centre-of-mass contribution as

$$H = \sum_{i=1}^{A-1} \hbar\omega\Big(-\frac{1}{2}\Delta_{s_i^{(b)}} + \frac{1}{2}\big|\vec{s}^{(b)}_i\big|^2\Big) + \sum_{i<j}^{A} V_{ij} + \sum_{i<j<k}^{A} W_{ijk} \,. \qquad (3.26)$$

Successively, I derive the elements of the Hamiltonian for the three different terms in the symmetric basis states $\left|\overline{\phi^{(A)}}_\omega\right\rangle$.

The first term, the sum over the harmonic oscillator contribution, is trivial. The basis state $\left|\overline{\phi^{(A)}}_\omega\right\rangle$ is by construction (see section 3.1.1) a linear combination of coupled oscillator functions in the Jacobi coordinates with the same total angular momentum and total energy, since the recoupling and the Talmi-Moshinsky transformation conserve both quantum numbers. Each basis state $\left|\overline{\phi^{(A)}}_\omega\right\rangle$ has a definite total angular momentum L_ω and energy expressed by N_ω. Accordingly

$$\left\langle\overline{\phi^{(A)}}_\omega\right|\sum_{i=1}^{A-1}\hbar\omega\Big(-\frac{1}{2}\Delta_{s_i^{(b)}}+\frac{1}{2}\big|\vec{s}_i^{\,(b)}\big|^2\Big)\left|\overline{\phi^{(A)}}_{\omega'}\right\rangle = \delta_{L_\omega,L_{\omega'}}\;\delta_{N_\omega,N_{\omega'}}\;\big(N_\omega+(A-1)3/2\big)\hbar\omega\;. \tag{3.27}$$

In order to calculate the second term, one has to realise that all terms in the sum over pairs yield the same contribution for a symmetric state. Hence, only the contribution of a single pair potential must be determined which is then multiplied by the number of pairs $\binom{N}{2}=\frac{N(N-1)}{2}$.

My construction of the symmetric states suggests that the potential contribution of the pair

$$V_{(A-1)A}(|\vec{x}_{(A-1)}-\vec{x}_A|)$$

is suited to determine this contribution. As shown in Figure 3.1 the distance $|\vec{x}_{(A-1)}-\vec{x}_A|$ is proportional to $|\vec{\lambda}|$ and one has for the potential

$$V_{(A-1)A}\big(|\vec{x}_{(A-1)}-\vec{x}_A|\big)=V_{(A-1)A}\big(\sqrt{2}|\vec{\lambda}|\big)\;. \tag{3.28}$$

With the help of the matrix $B_{\text{sym}}^{(A-1)\to A}$ and the transformation in equation (3.24), the symmetric state $\overline{\phi^{(A)}}_\omega$ can be expanded in wave functions depending on $\vec{\lambda}$ and $\vec{\mu}$. In these wave functions, the potential is diagonal in all quantum numbers apart from n_λ and l_λ. Thus, the problem reduces to the determination of

$$\left\langle\phi_{n_\lambda l_\lambda}\middle|V_{(A-1)A}\middle|\phi_{n'_\lambda l'_\lambda}\right\rangle\;. \tag{3.29}$$

The corresponding integral has to be calculated for the explicit potentials to be considered.

The calculation of the three-body interactions is more involved. Again, only the interaction for a specific triplet in the sum must be calculated explicitly and the result of the whole sum follows by combinatorics. The number of triplets is given by $\binom{N}{3}=\frac{N(N-1)(N-2)}{6}$. As for the two-body potentials, the construction of the symmetric states suggests considering a particular three-body contribution. Because the form of the wave function as a function of $\vec{\lambda}$ is known, the potential contribution $W_{(A-2)(A-1)A}$ is a good choice. However, $W_{(A-2)(A-1)A}$ is not only a function in $\vec{\lambda}$ and $\vec{\mu}$, but of $\vec{\lambda}$ and a combination of $\vec{\mu}$ and $\vec{s}_{(A-3)}$. Therefore, a further Talmi-Moshinsky transformation from the coordinates $\vec{\lambda}$, $\vec{\mu}$ and $\vec{s}_{(A-3)}$ to the coordinates $\vec{\lambda}$, $\vec{\kappa}$ and $\vec{\nu}$ as depicted in Figure 3.2 is performed. Of course, this implies further angular momentum recouplings with Wigner-6j symbols.

The corresponding orthogonal coordinate transformation is given by

$$\begin{pmatrix}\vec{\nu}\\ \vec{\kappa}\end{pmatrix}=\begin{pmatrix}\sqrt{\frac{A}{3(A-2)}} & -\sqrt{\frac{2(A-3)}{3(A-2)}}\\ \sqrt{\frac{2(A-3)}{3(A-2)}} & \sqrt{\frac{A}{3(A-2)}}\end{pmatrix}\cdot\begin{pmatrix}\vec{s}_{(A-3)}\\ -\vec{\mu}\end{pmatrix}\;. \tag{3.30}$$

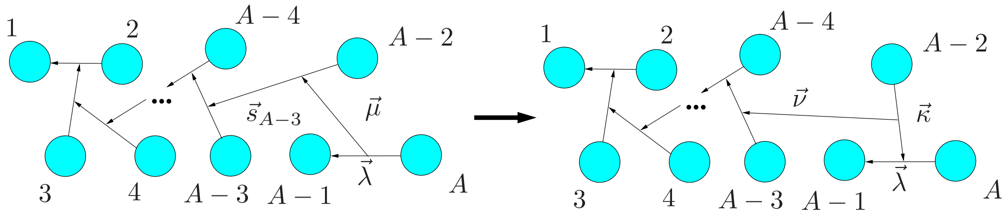

Figure 3.2: Talmi transformation from coordinates $\vec{s}_{(A-3)}$ and $\vec{\mu}$ to coordinates $\vec{\nu}$ and $\vec{\kappa}$

The transformation is stored in the matrix

$$M^{(123)}[\alpha', n_2', l_2', L; \gamma, n_\nu, l_\nu, n_\kappa, l_\kappa, n_\lambda, l_\lambda, L_{\lambda\kappa}, L_{123}] = \\ \left\langle \left[\overline{\phi^{(A-3)}}_{\gamma}^{L_\gamma} \otimes \left[\phi_{n_\nu l_\nu} \otimes \left[\phi_{n_\lambda l_\lambda} \otimes \phi_{n_\kappa l_\kappa}\right]^{L_{\lambda\kappa}}\right]^{L_{123}}\right]^{L} \middle| \left[\overline{\phi^{(A-1)}}_{\alpha'} \otimes \phi_{n_2' l_2'}\right]^{L} \right\rangle . \tag{3.31}$$

In the new coordinates the three-body Interaction $W_{A(A-1)(A-2)}$ is diagonal in all quantum numbers apart from n_λ, l_λ, n_κ, l_κ. Thus, the matrix elements depend only on the three-body subsystem and the following matrix elements has to be calculated with the explicit form of the interaction:

$$\left\langle \left[\phi_{n_\lambda l_\lambda} \otimes \phi_{n_\kappa l_\kappa}\right]^{L} \middle| W_{A(A-1)(A-2)} \middle| \left[\phi_{n_\lambda' l_\lambda'} \otimes \phi_{n_\kappa' l_\kappa'}\right]^{L} \right\rangle \tag{3.32}$$

3.1.4 Numerical Approach

In this section I illustrate the structure of my algorithm for the J-scheme shell model. Figure 3.3 shows a schematic flow diagram, which emphasises the important points.

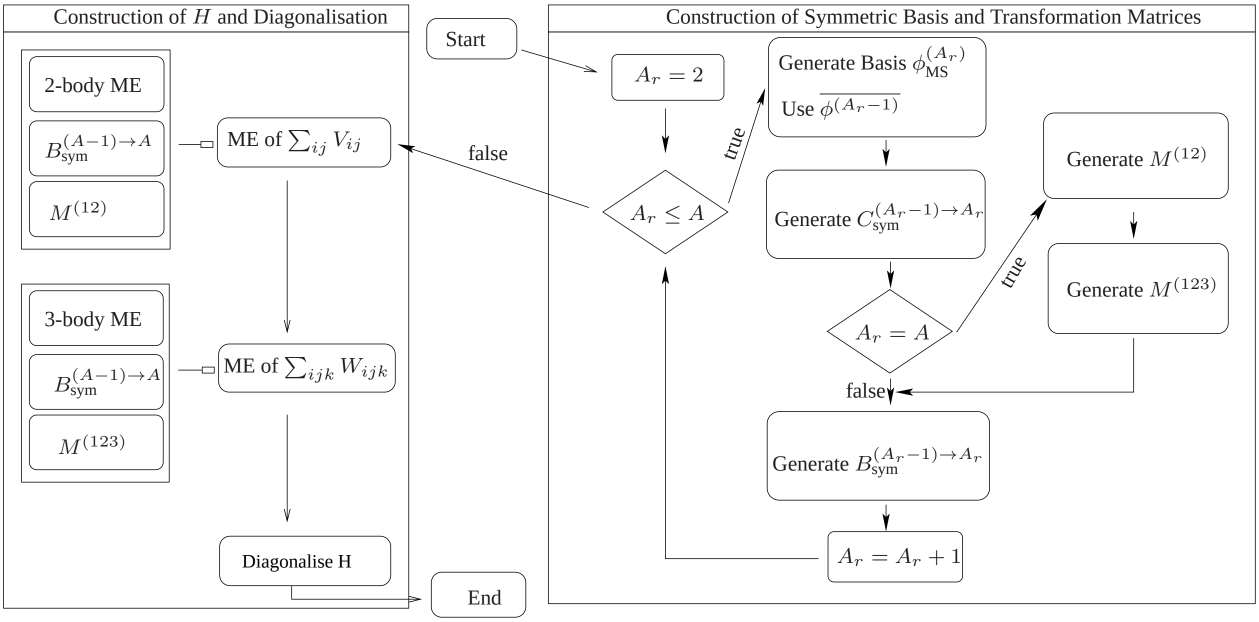

Figure 3.3: Schematic flow diagram for the J-scheme algorithm. Note that, the construction of the symmetric basis and transformation matrices $M^{(12)}$ and $M^{(123)}$ need to be done for each cutoff N only once.

Notably, the algorithm can be split into two parts. The first part, the construction of the symmetric basis with matrix $B_{\text{sym}}^{(A-1)\to A}$ and transformation matrices $M^{(12)}$ and $M^{(123)}$, needs to be calculated for a fixed cutoff N only once. For each specific interaction they can be reused in the second part.

In the first part the symmetric basis is iteratively determined using the approach described in section 3.1.1. At the beginning, the mixed-symmetric states $\phi_{MS}^{A_r}$ are generated from the known symmetric states $\overline{\phi^{(A_r-1)}}$ in equation (3.21). Afterwards, the matrix $C_{\text{sym}}^{(A_r-1)\to(A_r)}$ is constructed by using the procedure presented in section 3.1.2. In the last iteration cycle, the transformation matrices $M^{(12)}$ and $M^{(123)}$ are stored, because they are required to determine the elements of the Hamiltonian (ME). With equation (3.20) the matrix $B_{\text{sym}}^{(A_r-1)\to(A_r)}$ is calculated.

In the second part the contributions of the two-body and three-body interaction in the ME's of the Hamiltonian H can be calculated as outlined in section 3.1.3. For this purpose, one needs the two-body ME's in equation (3.29), the matrix $B_{\text{sym}}^{(A-1)\to(A)}$, and the matrix $M^{(12)}$ or the three-body ME's in equation (3.32) and $M^{(123)}$, respectively. The final step is the numerical diagonalisation of H which yields as a result the binding energies for a given cutoff N.

3.2 M-Scheme Shell Model in One-Particle Coordinates

An alternative approach is to construct the basis from the oscillator functions, given in equation (3.2), in one-particle coordinates. Thus here, the centre-of-mass dynamics is not separated. The A-boson system is really treated as an A-particle system and all excitations of the centre-of-mass are included.

Moreover, product states of single particle functions with projection quantum number m_i are used instead of the coupled angular momenta and total angular momentum L. Accordingly, this kind of basis is called M-Scheme. As a consequence, it is not possible to calculate the energy spectrum for a fixed L, but one determines automatically the energies for all possible L values for a fixed M. In the following subsections, the construction of the symmetric basis and the determination of matrix elements are outlined.

3.2.1 Symmetric Basis

The A-body sector of identical bosons is described in one-particle coordinates by A oscillator functions with quantum numbers n, l, and m, which are symmetric under permutation of bosons. For brevity, the quantum numbers are collected in a multi-index $\kappa_i = n_i, l_i, m_i$. Furthermore, an order of these multi-indices is defined by

$$\kappa_i < \kappa_j \text{ , if } \begin{cases} [n_i < n_j] \ , \\ [n_i = n_j] \wedge [l_i < l_j] \ , \\ [n_i = n_j] \wedge [l_i = l_j] \wedge [m_i < m_j] \ . \end{cases} \tag{3.33}$$

A generally non-symmetric A-body oscillator state is simply given by the tensor product of one-particle oscillator states:

$$\left|\kappa_1, \kappa_2, \ldots, \kappa_A\right\rangle \equiv \left|\kappa_1\right\rangle \otimes \left|\kappa_2\right\rangle \otimes \ldots \otimes \left|\kappa_A\right\rangle \ . \tag{3.34}$$

Note that these states mean oscillator functions with oscillator length $b = 1$ corresponding to dimensionless coordinates $\vec{x}_i/b$. The projector $S^{(A)}$ on an A-body symmetric state is defined by

$$S^{(A)} := \frac{1}{A!} \sum_{\sigma \in \mathcal{S}_A} \hat{\sigma} \ , \tag{3.35}$$

where $\hat{\sigma}$ is a permutation of the symmetric group $\mathcal{S}_A$ defined as

$$\hat{\sigma} \big| \kappa_1, \kappa_2, \ldots, \kappa_A \big\rangle := \big| \kappa_{\sigma(1)}, \kappa_{\sigma(2)}, \ldots, \kappa_{\sigma(A)} \big\rangle \ . \tag{3.36}$$

Normalised states are then given by

$$\big| \kappa_1, \kappa_2, \ldots, \kappa_A \big) = \left(\frac{A!}{\prod_\alpha n_\alpha !} \right)^{1/2} S^{(A)} \big| \kappa_1, \kappa_2, \ldots, \kappa_A \big\rangle \ , \tag{3.37}$$

with the occupation numbers of the one-particle states α. Note that an A-boson state is completely characterised by the κ's in arbitrary order. The symmetric state is described uniquely with the requirement

$$\kappa_1 \leq \kappa_2 \leq \ldots \leq \kappa_A \ . \tag{3.38}$$

Furthermore, the A-boson state is also uniquely specified by the occupation numbers n_α of each single particle state $\big|\alpha\big\rangle$. Consequently, the many-body state $\big|I\big)$ can be denoted in (at least) two different, but equivalent, ways

$$\big| I \big) \equiv \big| \kappa_1, \kappa_2, \ldots, \kappa_A \big) \equiv \big| n_1, n_2, \ldots, n_m \big) \ , \tag{3.39}$$

with the assumption that m different one-particle states exist and that $\kappa_1 \leq \kappa_2 \leq \ldots \leq \kappa_A$. In order to represent an A-body state in numerical calculations, the former representation is more appropriate since $A \ll m$ (see section 3.2.3).

Thus, in the M-scheme in one-particle coordinates the construction of symmetric states are trivial because the action of the projector $S^{(A)}$ is obvious.

3.2.2 Model Space and Matrix Elements of *H*

Apart from the centre-of-mass excitation I shall define the model space for the shell-model calculations in the same manner as for the J-scheme in Jacobi coordinates. With $N_i = (2n_i + l_i)$ the model space is defined as the linear hull of states $\big| \kappa_1, \kappa_2, \ldots, \kappa_A \big)$ with the restriction

$$\sum_{i=1}^{A} N_i \leq N \ , \tag{3.40}$$

where N is the cutoff parameter.

In order to calculate the contribution of the three terms in the Hamiltonian in equation (3.1), it is advantageous to rewrite these terms with creation and annihilation operators $a_\alpha^\dagger$ and a_α (see e.g. [64]); accordingly for the states we have:

$$a_\alpha^\dagger \big| n_1, n_2, \ldots, n_\alpha, \ldots, n_m \big) := \sqrt{n_\alpha + 1} \ \big| n_1, n_2, \ldots, (n_\alpha + 1), \ldots, n_m \big) \ , \tag{3.41}$$

$$a_\alpha \big| n_1, n_2, \ldots, n_\alpha, \ldots, n_m \big) := \sqrt{n_\alpha} \ \big| n_1, n_2, \ldots, (n_\alpha - 1), \ldots, n_m \big) \ . \tag{3.42}$$

With the definitions

$$V_A^{(1)} = \sum_{i=1}^{A} \hbar\omega\big(\frac{1}{2}\Delta_{x_i^{(b)}} + \frac{1}{2}|\vec{x}_i^{(b)}|^2\big) \ , \qquad V_A^{(2)} = \sum_{i<j}^{A} V_{ij} \ , \qquad V_A^{(3)} = \sum_{i<j<k}^{A} W_{ijk} \ , \tag{3.43}$$

the terms of the Hamiltonian can be expressed in the occupation number formalism as:

$$V_A^{(1)}\big|n_1,\ldots,n_m\big) = \sum_{\alpha,\alpha'} \big\langle\alpha'\big|\hbar\omega\big(\frac{1}{2}\Delta_{x^{(b)}} + \frac{1}{2}\big|\vec{x}_i^{(b)}\big|^2\big)\big|\alpha\big\rangle a_{\alpha'}^{\dagger} a_{\alpha}\big|n_1,n_2,\ldots,n_m\big) \ , \tag{3.44}$$

$$V_A^{(2)}\big|n_1,\ldots,n_m\big) = \frac{1}{2}\sum_{\beta\beta'\alpha\alpha'} \big\langle\alpha'\beta'\big|V\big|\alpha\beta\big\rangle a_{\alpha'}^{\dagger} a_{\beta'}^{\dagger} a_{\alpha} a_{\beta}\big|n_1,n_2,\ldots,n_m\big) \ , \tag{3.45}$$

$$V_A^{(3)}\big|n_1,\ldots,n_m\big) = \frac{1}{6}\sum_{\alpha\beta\gamma}\sum_{\alpha'\beta'\gamma'} \big\langle\alpha'\beta'\gamma'\big|W\big|\alpha\beta\gamma\big\rangle a_{\alpha'}^{\dagger} a_{\beta'}^{\dagger} a_{\gamma'}^{\dagger} a_{\alpha} a_{\beta} a_{\gamma}\big|n_1,n_2,\ldots,n_m\big) \ . \tag{3.46}$$

In this new notation it is clear that a many-body matrix element for the one-body, two-body or three-body operators can only be non-zero if initial and final states differ in the quantum numbers of at most one, two, or three one-particle states, respectively. Thus, a new abbreviation is introduced: e.g. the state $\big|(I-\alpha\beta;\alpha'\beta')\big)$ denotes the many-body state $\big|I\big)$, where a one-particle state α is substituted by α' and β by β'. In the next three paragraphs, the calculation of the many-body matrix elements for these three operators are explained in detail.

Many-Body Matrix Elements for the One-Body Operators: In this paragraph, I specify the many-body matrix elements for the harmonic oscillator terms. From equation (3.44) it follows that

$$\big((I-\mu;\nu)\big|V_A^{(1)}\big|I\big) = \sum_{\alpha,\alpha'} \big\langle\alpha'\big|\hbar\omega\big(\frac{1}{2}\Delta_{x^{(b)}} + \frac{1}{2}\big|\vec{x}_i^{(b)}\big|^2\big)\big|\alpha\big\rangle \ \big((I-\mu;\nu)\big|a_{\alpha'}^{\dagger} a_{\alpha}\big|I\big) \ , \tag{3.47}$$

$$= \ \delta_{\mu,\nu} \ \hbar\omega \ (N_\nu + A\,\frac{3}{2})\ n_\nu \ . \tag{3.48}$$

Many-Body Matrix Elements for the Two-Body Operators: With equation (3.45) a similar relation for the two-body operators can be derived:

$$\big((I-\alpha\beta;\gamma\delta)\big|V_A^{(2)}\big|I\big) = \frac{1}{2}\sum_{\mu\nu\rho\sigma} \big\langle\mu\nu\big|V\big|\rho\sigma\big\rangle \ \big((I-\alpha\beta;\gamma\delta)\big|a_{\mu}^{\dagger} a_{\nu}^{\dagger} a_{\rho} a_{\sigma}\big|I\big) \ , \tag{3.49}$$

$$\begin{aligned} =&\frac{1}{2}\sum_{\mu\leq\nu}\sum_{\rho\leq\sigma}(2-\ \delta_{\mu,\nu}\ )(2-\ \delta_{\rho,\sigma}\ )\frac{1}{4} \\ &\big\langle(\mu\nu+\nu\mu)\big|V\big|(\rho\sigma+\sigma\rho)\big\rangle\big((I-\alpha\beta;\gamma\delta)\big|a_{\mu}^{\dagger} a_{\nu}^{\dagger} a_{\rho} a_{\sigma}\big|I\big) \end{aligned} \quad . \tag{3.50}$$

The one-particle states in $\big|I\big)$ are sorted in ascending order. For the purpose of preserving this order, it is required that $\alpha \leq \beta$ and $\gamma \leq \delta$. Therefore the last term in the sum $\big((I-\alpha\beta;\gamma\delta)\big|a_{\mu}^{\dagger} a_{\nu}^{\dagger} a_{\rho} a_{\sigma}\big|I\big)$ does not vanish only if $\alpha = \rho$, $\beta = \sigma$, $\gamma = \mu$, and $\delta = \nu$. The term only depends on the occupation numbers and one has for the factors e. g.

$$\big((I-\alpha\beta;\gamma\delta)\big|a^\dagger_\gamma a^\dagger_\delta a_\alpha a_\beta\big|I\big) = \sqrt{(n_\gamma+1)(n_\delta+1)n_\alpha n_\beta}\ , \tag{3.51}$$

$$\big((I-\alpha\alpha;\gamma\delta)\big|a^\dagger_\gamma a^\dagger_\delta a_\alpha a_\alpha\big|I\big) = \sqrt{n_\gamma n_\delta(n_\alpha-1)n_\alpha}\ , \tag{3.52}$$

$$\big((I-\alpha\beta;\alpha\delta)\big|a^\dagger_\alpha a^\dagger_\delta a_\alpha a_\beta\big|I\big) = n_\alpha\sqrt{(n_\delta+1)n_\beta}\ , \tag{3.53}$$

$$\big((I-\alpha\alpha;\alpha\alpha)\big|a^\dagger_\alpha a^\dagger_\alpha a_\alpha a_\alpha\big|I\big) = (n_\alpha-1)n_\alpha\ . \tag{3.54}$$

For the calculation of the two-body matrix elements it is not necessary to calculate and store all four combinations, but it can be simplified with symmetric two-body states. For symmetric two-body states $\big|\tilde\mu\tilde\nu\big)$ with $\tilde\mu \le \tilde\nu$ it follows that

$$\big\langle(\mu\nu+\nu\mu)\big|V\big|(\rho\sigma+\sigma\rho)\big\rangle = 4\sum_{\tilde\mu\le\tilde\nu}\sum_{\tilde\rho\le\tilde\sigma}\big\langle\mu\nu\big|\big|\tilde\mu\tilde\nu\big)\ \big(\tilde\mu\tilde\nu\big|V\big|\tilde\rho\tilde\sigma\big)\ \big(\tilde\rho\tilde\sigma\big|\big|\rho\sigma\big\rangle\ . \tag{3.55}$$

Therefore, only the matrix elements $\big(\tilde\mu\tilde\nu\big|V\big|\tilde\rho\tilde\sigma\big)$ have to be precalculated and stored. In my implementation, I do not store the two-body matrix elements in one-particle coordinates, but I save memory and store them in Jacobi coordinates. Hence, a Talmi-Moshinsky transformation is necessary ”on-the-fly” to transform the matrix elements in the single-particle basis.

Many-Body Matrix Elements for the Three-Body Operators: Similarly, the many-body matrix elements of the three-body operators in equation (3.46) can be expressed as

$$\begin{aligned}
&\big((I-\alpha\beta\gamma;\delta\epsilon\eta)\big|V^{(3)}_A\big|I\big)\\
=&\frac{1}{6}\sum_{\mu\nu\rho}\sum_{\sigma\kappa\tau}\big\langle\mu\nu\rho\big|W\big|\sigma\kappa\tau\big\rangle\ \big((I-\alpha\beta\gamma;\delta\epsilon\tau)\big|a^\dagger_\mu a^\dagger_\nu a^\dagger_\rho a_\sigma a_\kappa a_\tau\big|I\big)\ ,
\end{aligned} \tag{3.56}$$

$$\begin{aligned}
=&\frac{1}{6}\sum_{\mu\le\nu\le\rho}\sum_{\sigma\le\kappa\le\tau}\big(1-\frac{1}{2}(\,\delta_{\mu,\nu}\ +\ \delta_{\nu,\rho}\,)+\frac{1}{6}\,\delta_{\mu,\nu}\ \delta_{\nu,\rho}\,\big)\big(1-\frac{1}{2}(\,\delta_{\sigma,\kappa}\ +\ \delta_{\kappa,\tau}\,)+\frac{1}{6}\,\delta_{\sigma,\kappa}\ \delta_{\kappa,\tau}\,\big)\\
&\big\langle(\mu\nu\rho+\nu\mu\rho+\rho\nu\mu+\mu\rho\nu+\rho\mu\nu+\nu\rho\mu)\big|W\big|(\sigma\kappa\tau+\kappa\sigma\tau+\tau\kappa\sigma+\sigma\tau\kappa+\tau\sigma\kappa+\kappa\tau\sigma)\big\rangle\\
&\big((I-\alpha\beta\gamma;\delta\epsilon\tau)\big|a^\dagger_\mu a^\dagger_\nu a^\dagger_\rho a_\sigma a_\kappa a_\tau\big|I\big)\ .
\end{aligned} \tag{3.57}$$

Instead of calculating all 36 combinations of three-body matrix elements, only the matrix elements of symmetric three-body states $\big|\tilde\mu\tilde\nu\tilde\rho\big)$ with $\tilde\mu \le \tilde\nu \le \tilde\rho$ have to be considered:

$$\begin{aligned}
&\big\langle(\mu\nu\rho+\nu\mu\rho+\rho\nu\mu+\mu\rho\nu+\rho\mu\nu+\nu\rho\mu)\big|W\big|(\sigma\kappa\tau+\kappa\sigma\tau+\tau\kappa\sigma+\sigma\tau\kappa+\tau\sigma\kappa+\kappa\tau\sigma)\big\rangle\\
&\qquad = 36\sum_{\tilde\mu\tilde\nu\tilde\rho}\sum_{\tilde\sigma\tilde\kappa\tilde\tau}\big\langle\mu\nu\rho\big|\big|\tilde\mu\tilde\nu\tilde\rho\big)\ \big(\tilde\mu\tilde\nu\tilde\rho\big|W\big|\tilde\sigma\tilde\kappa\tilde\tau\big)\ \big(\tilde\sigma\tilde\kappa\tilde\tau\big|\big|\sigma\kappa\tau\big\rangle\ .
\end{aligned} \tag{3.58}$$

Consequently, I store only the matrix elements of symmetric three-body states $\big(\tilde\mu\tilde\nu\tilde\rho\big|W\big|\tilde\sigma\tilde\kappa\tilde\tau\big)$. Again, they are stored in Jacobi-coordinates with coupled angular momenta in order to save memory. Accordingly Talmi-Moshinsky transformations will be required ”on-the-fly”.

3.2.2.1 Shift of Centre-of-Mass Excitations

We are interested in the internal excitation energies of an A-body system inside a harmonic oscillator potential with two- and three-body forces. Thus, possible excitations of the centre-of-mass in this sense are spurious. In order to identify and eliminate centre-of-mass excitations in the energy spectrum the spurious excitations are energetically shifted with an additional centre-of-mass potential h_α (see e.g. van Hees et al. [65]) containing the operator

$$H_{\text{CM}} := \frac{\left|\vec{P}\right|^2}{2M} + \frac{1}{2}M\omega^2\left|\vec{R}\right|^2 , \tag{3.59}$$

where $M := Am$, $\vec{R} := 1/A\sum_{i=1}^{A}\vec{x}_i$ and $\vec{P} = \sum_{i=1}^{A}\vec{p}_i$. The additional potential is defined by

$$h_\alpha := -H_{\text{CM}} + \alpha\left(H_{\text{CM}} - \frac{3}{2}\hbar\omega\right) \quad , \quad \alpha \in \mathbb{R} , \tag{3.60}$$

and due to the vanishing commutator $\left[H, h_\alpha\right]_- = 0$ the eigenenergies E_α of the operator

$$H_\alpha := H + h_\alpha \tag{3.61}$$

read

$$E_\alpha = \left[E - (\tilde{N} + 3/2\hbar\omega)\right] + \left[\alpha\tilde{N}\hbar\omega\right] , \quad \tilde{N} \in \mathbb{N} . \tag{3.62}$$

The term $\left(E - (\tilde{N} + 3/2\hbar\omega\right)$ is the value of the internal energy eigenvalue without the centre-of-mass energy. All states with excited centre-of-mass are thus shifted by the value $\alpha\tilde{N}\hbar\omega$.

At the end, the new Hamiltonian H_α can be rewritten in single-particle coordinates with the result

$$\begin{aligned} H_\alpha = -\frac{3}{2}\alpha\hbar\omega + \alpha\sum_{i=1}^{A}\left(\frac{|\vec{p}_i|^2}{2m} + \frac{1}{2}m\omega^2\left|\vec{x}_i\right|^2\right) \\ -\frac{(\alpha-1)}{A}\left(\frac{1}{2m}\sum_{\substack{i,j=1\\ i<j}}^{A}\left|\vec{p}_i - \vec{p}_j\right|^2 + \frac{1}{2}m\omega^2\sum_{\substack{i,j=1\\ i<j}}^{A}\left|\vec{x}_i - \vec{x}_j\right|^2\right) + V_A^{(2)} + V_A^{(3)} . \end{aligned} \tag{3.63}$$

I shall use Jacobi coordinates in order to determine the two-body part of the centre-of-mass oscillator potential. Note the factor 2 in the relation

$$\left|\vec{x}_1 - \vec{x}_2\right|^2 = 2\left|\vec{s}_1\right|^2 . \tag{3.64}$$

3.2.3 Numerical Procedure

In this section, I sketch the basics of the algorithm for generating the non-zero many-body matrix elements in the M-scheme. Furthermore, I indicate some prescriptions in order to accelerate the procedure. Figure 3.4 shows a schematic overview of the procedure.

At first, the basis for the model space is generated. Each basis vector is stored as an array of A ascending entries κ_i and these are numbered consecutively. In order to find the contributions of $V_A^{(2)}$ and $V_A^{(3)}$, the basic idea is to loop over all initial states $\big|I\big)$ in the basis and to find all possible

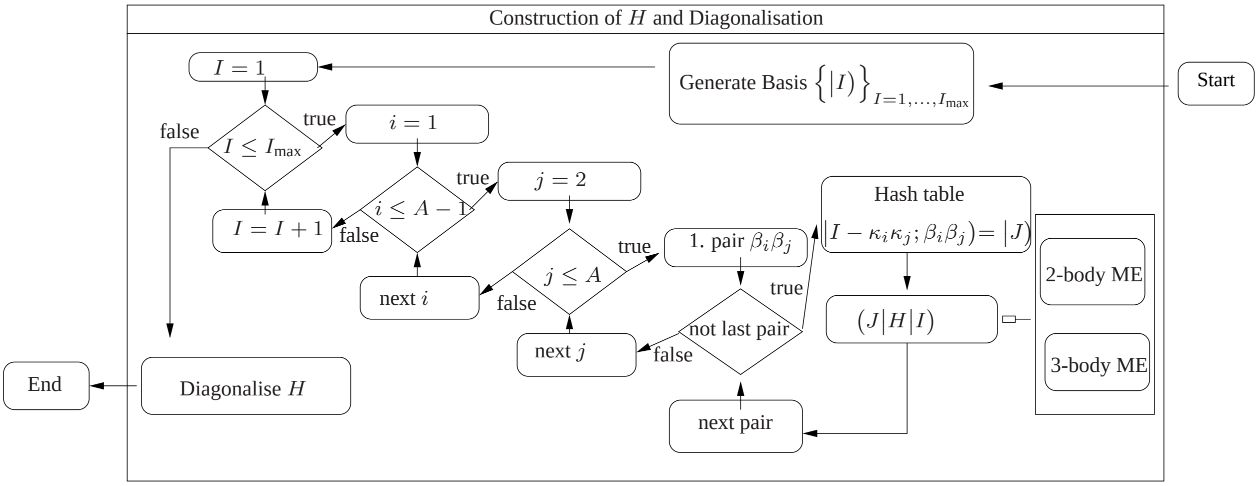

Figure 3.4: Schematic flow diagrom for the M-scheme algorithm.

final states $\big|F\big)$ that can be reached by two-body or three-body jumps, respectively. Explicitly, only the procedure for two-body potentials will be outlined.

In order to determine all matrix elements, the outer loop is over all initial many-body states $\big|I\big)$. With a loop over all pairs of particle indices $\sum_{i<j}^{A}$, each pair of one-particle states $\kappa_i\kappa_j$ is selected once and can be removed. Subsequently, all possible new pairs of one-particle states $\beta_i\beta_j$ are generated at this position. In this manner, the same final state is created several times and the final state $\big|(I-\kappa_i\kappa_j);\beta_i\beta_j\big)$ does not have the required property of ascending one-particle indexes in general. This can be dealt with by sorting the states. The solution of the former problem is explained below. In the next step, the precomputed two-body matrix elements in Jacobi-coordinates are read in and transformed to single-particle coordinates with Talmi-Moshinsky transformations. Afterwards, one has to map the constructed final state to the index in the many-body basis. For this step, hash tables are crucial. At the end, one has calculated all matrix elements $\big(F\big|V_A^{(2)}\big|I\big)$. In similar way, the three-body elements can be found and the required Hamiltonian $\big(F\big|H\big|I\big)$ is determined. The final step is the diagonalisation of the Hamiltonian.

Loop Over Permitted Final States: There are several constraints for the substitution of pairs $\kappa_i\kappa_j$ which must be considered. Because of the ascending order in many-body states, only pairs with $\beta_i \le \beta_j$ are relevant. Furthermore, the potentials conserve the total projection $M(\kappa_i\kappa_j) := (m_{\kappa_i} + m_{\kappa_j})$ and the parity $\Pi(\kappa_i\kappa_j) = (l_{\kappa_i} + l_{\kappa_j} \bmod 2)$ in the two-body system. Thus the selection rules $M(\beta_i\beta_j) = M(\kappa_i\kappa_j)$ and $\Pi(\kappa_i\kappa_j) = \Pi(\beta_i\beta_j)$ apply. At the end, only final states inside the model space, defined by the cutoff N, are allowed to be generated. Therefore, the total energy of the initial state N_I minus the energy of the pair $N_2(\kappa_i\kappa_j) := (2(n_{\kappa_i} + n_{\kappa_j}) + l_{\kappa_i} + l_{\kappa_j})$ plus $N_2(\beta_i\beta_j)$ must not be greater than N.

Loop Over Unique Final States: In order to guarantee that each permitted final state is produced exactly once, I choose the following procedure: The outer loop is over i and the inner loop over $j > i$. At first $j = i+1$, i.e. the pair $\kappa_i\kappa_{(i+1)}$ is selected and substituted by all permitted pairs $\beta_i\beta_{(i+1)}$. Subsequently, j is increased as long $j < A$. Note that the increment depends on the occupation numbers. For instance, for the initial state

$$\big|I\big) = \big|\kappa_1, \dots, \underbrace{\overset{i}{\overset{\downarrow}{\gamma}}, \overset{j}{\overset{\downarrow}{\gamma}}, \dots, \gamma}_{n_\gamma}, \underbrace{\delta, \delta, \dots, \delta}_{n_\delta}, \underbrace{\epsilon, \epsilon, \dots, \epsilon}_{n_\epsilon}, \dots, \kappa_A\big) \tag{3.65}$$

j is increased with the increment $(n_\gamma - 1)$. Otherwise, a pair $\gamma\gamma$ is substituted a second time and the same final states would be generated. Now, the pair $\gamma\delta$ is changed into all allowed pairs $\beta_i\beta_j$. Afterwards, j is increased with the increment n_δ and so on. If $j > A$, i is increased with the increment n_γ and j is again $(i+1)$ and so on.

3.3 Comparison of both Shell Models

In the last two sections I have introduced two different shell-model approaches, the M-scheme and J-scheme, to treat the A-boson system with two- and three-body interactions. In this section the merits and drawbacks are summarised.

To start with, the number of many-body states in the M-scheme and the J-scheme approach are compared. Due to separation of the centre-of-mass and exploiting of total-angular momentum conservation the number of relevant many-body states is much smaller in the J-scheme. In Figure 3.5 the number of states with total angular momentum and parity $J^P = 0^+$ or total angular momentum projection and parity $M^P = 0^+$ are shown in dependence of the cutoff parameter N for various A-body systems logarithmically. There are several orders of magnitude more basis states in the M-scheme for the same cutoff parameter. Thus, the most elaborate task in the two schemes is different. In the M-scheme the most time-consuming part is the diagonalisation of the many-body Hamiltonian. For example for twelve particles a (120000×120000)-matrix is to be diagonalised just for the cutoff parameter $N = 14$ in contrast to a 4500×4500-matrix in the J-scheme.

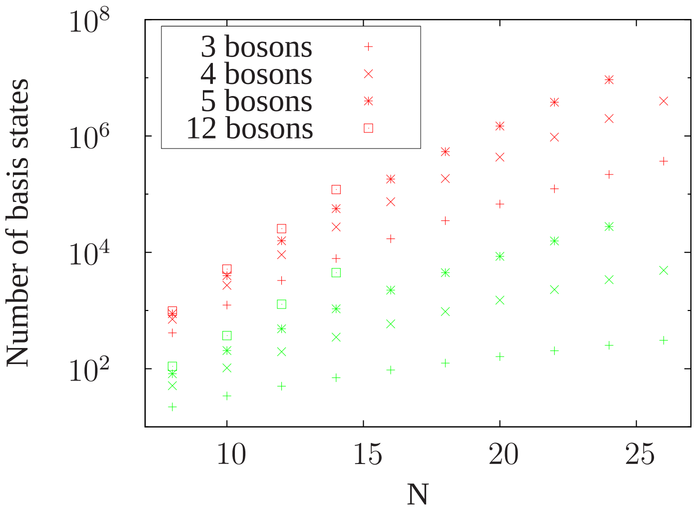

Figure 3.5: Number of many-body basis states versus the cutoff parameter N. Different point types differentiate the number of bosons. Green points correspond to the J-scheme basis-states with $J^P = 0^+$ and red points to the $M^P = 0^+$ states for the M-scheme.

For the J-scheme the most time-consuming task is the iterative construction of the symmetric basis and of the corresponding transformation matrices (see Figure 3.3). The scaling behaviour of the runtime of this first part in the algorithm is depicted versus the cutoff parameter N for various A-boson systems in Figure 3.6. More interesting than the absolute runtime (which depends on the hardware) is the scaling behaviour reflected in the scope of the double logarithmic plot. As expected the scope is increasing with A due to the higher complexity of the problem. Thus, an enhancement in N would result in a massive larger runtime for large A-boson systems. The runtime of the second part of the algorithm is added as filled dots. Remarkably, the scopes are similar to the corresponding first parts but the absolute runtime is smaller by an order of magnitude.

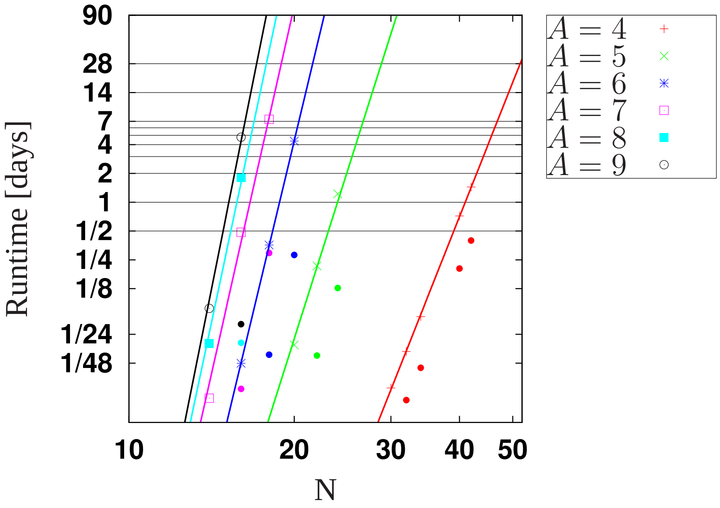

Figure 3.6: Runtime of the algorithm for the construction of the symmetric basis with total angular momentum and parity $L^P = 0^+$ versus the cutoff parameter N for various A. The filled dots without linear fit mark the runtime for the rest of the algorithm including construction of the Hamiltonian and its diagonalisation.

From this the most eminent advantage of the J-scheme in comparison to the M-scheme follows. As illustrated in Figure 3.3 the J-scheme algorithm can be split. The most elaborate first part is independent of the specific two- and three-body interaction and the coupling constant. Hence, the first part must be calculated for given N and A only once. Its results, the symmetric basis and the transformation matrices, are stored and reused for the second part. Therefore, the J-scheme is definitely the favourable prescription to treat and analyse specific interactions globally, i.e. with several coupling constants combinations, for several oscillator lengths etc.

The benchmarking of these two schemes for a single completely specified interaction is not clear. The advantage of the M-scheme is that the most time-consuming problem is a standard problem which is highly parallelisable. Owing to the size and the spareness of the huge symmetric matrix in the M-scheme it is possible to find some extreme eigenvalues with Krylov subspace methods in combination with QR-decomposition [66], e.g. Lanczos procedures. There are a multitude of implemented and optimised routines which are offered also in parallelised versions in the message-passing-interface (MPI) standard, e.g. ARPACK or BLZPACK.

The results in the following sections are produced in the J-scheme, since several interactions and the dependence on some parameters are investigated. Occasionally, some J-scheme results were compared with M-scheme results and they were found to numerically coincide at least to eight decimal places.

Chapter 4

Few Bosons in Traps

In this section, I consider a system of bosons confined by a harmonic oscillator potential (HOP) in the scaling limit. The two- and three-body systems which I studied in my diploma thesis [16] are cited for completeness. Other results are partially published in [67] and [62].

4.1 Framework in the Scaling Limit

Within the shell-model approach, the eigenvalues of the Hamiltonian of equation (3.26) are determined for contact interactions $V(\vec{s}_1^{(b)}) = g^{(2)}\delta^{(3)}(\vec{s}_1^{(b)})$ and $W(\vec{s}_1^{(b)}, \vec{s}_2^{(b)}) = g^{(3)}\delta^{(3)}(\vec{s}_1^{(b)})\delta^{(3)}(\vec{s}_2^{(b)})$ with Jacobi coordinates $\vec{s}_i^{(b)} = \vec{s}_i/b$ (see appendix A). As mentioned before, the model space is restricted with a cutoff N and the coupling constants $g^{(2)}$ and $g^{(3)}$ are renormalised to specific observables. My strategy follows Stetcu et al. [68–70] where an effective theory for short-range nuclear forces in the framework of the no-core shell model was formulated. The cutoff N is identified with a high energy (ultraviolet) cutoff of the effective theory: Usually a momentum cutoff Λ is defined in effective theories to regularise the integral equation and one finds a linear dependence of observables on $1/\Lambda$ in first order of the theory. Because of the relation $p \propto \sqrt{E}$ between momentum p and energy E, one expects errors for the binding energies for systems with confinement of the order $1/\sqrt{N + (A-1)3/2}$. Here $(A-1)3/2$ is the zero-point energy of the internal motion in HOP.

In contrast to the momentum cutoff Λ used in free space, the regulator N also implies an infrared cutoff. In the literature there are two definitions of the IR-cutoff for an oscillator basis. Both the expression $\beta/\sqrt{N + (A-1)3/2}$ [71, 72], which quantifies the maximum size of structures that can be captured in the given basis, or alternatively the oscillator length β itself [73] have been interpreted as an IR-cutoff. In my calculations, the harmonic oscillator represents a physical trap and thus β is a physical parameter. The trap acts like a finite box that confines the system. In this case, only the first definition seems appropriate and I expect errors of order $1/\sqrt{N + (A-1)3/2}$ due to the infrared cutoff. These errors have the same scaling behaviour with N as the errors from the ultraviolet cutoff and vanish for $N \to \infty$.

Matrix Elements of V and W: The matrix elements of the two-body potentials V with the harmonic oscillator wave functions $\phi_{nlm}(\vec{s}_1^{(b)}) = \langle \vec{s}_1^{(b)} | nlm \rangle$ are given by

$$\langle nlm | V | n'l'm' \rangle = g^{(2)} \phi_{n00}(0) \phi_{n'00}(0)\, \delta_{l,0}\ \delta_{l',0}\ \delta_{m,0}\ \delta_{m',0}\ . \tag{4.1}$$

Analogously, the matrix elements of the three-body interaction W are given by

$$\begin{aligned} &\langle n_1 l_1, n_2 l_2; LM | V | n_1' l_1', n_2' l_2'; L'M' \rangle = \\ &\qquad g^{(3)} \phi_{n_1 00}(0) \phi_{n_1' 00}(0) \phi_{n_2 00}(0) \phi_{n_2' 00}(0)\, \delta_{l_1,0}\ \delta_{l_2,0}\ \delta_{l_1',0}\ \delta_{l_2',0}\ \delta_{L,0}\ \delta_{L',0}\ \delta_{M,0}\ \delta_{M',0}\ , \end{aligned} \tag{4.2}$$

where the three-body wave function is defined by

$$\left[\phi_{n_1 l_1 m_1}(\vec{s}_1^{(b)}) \otimes \phi_{n_2 l_2 m_2}(\vec{s}_2^{(b)})\right]^L_M = \langle \vec{s}_1^{(b)}, \vec{s}_2^{(b)} | n_1 l_1, n_2 l_2; LM \rangle\ . \tag{4.3}$$

The value of oscillator functions at the origin is non-vanishing for $l = 0$ only and is given by

$$\phi_{n00}(\vec{s}_1^{(b)} = 0) = \frac{1}{\pi^{3/4}} \left(\frac{\Gamma(n + \frac{3}{2})}{\Gamma(\frac{3}{2}) \Gamma(n+1)} \right)^{1/2} = \left(\frac{(2n+1)!!}{\pi^{3/2}\, n!\, 2^n} \right)^{1/2}\ . \tag{4.4}$$

Renormalisation of $g^{(2)}$: The coupling constant $g^{(2)}$ has to be renormalised by an observable in the two-body sector such as a given energy level $E^{(2)}$ or alternatively the scattering length a. The relation between $g^{(2)}$ and $E^{(2)}$ for a given cutoff N can be found analytically by exploiting the separability of the interaction. With the definition $f_n := \phi_{n00}(0)$, the matrix elements in the two-body sector for $l = 0$ are given by

$$\langle n | H^{(2)} | n' \rangle = \hbar\omega \left(2n + \frac{3}{2} \right) \delta_{n,n'} + g^{(2)} f_n f_{n'}\ . \tag{4.5}$$

In the model space corresponding to N, the solution $|\psi_{E^{(2)}}\rangle$ of the eigenvalue problem with the eigenvalue $E^{(2)}$ is expanded in oscillator functions

$$|\psi_{E^{(2)}}\rangle = \sum_{n=0}^{N/2} c_n^{E^{(2)}} |n\rangle\ . \tag{4.6}$$

Applying the Hamiltonian to Eq. (4.6) and projecting on the oscillator state $|k\rangle$, one obtains

$$\left(2k + \frac{3}{2} \right) c_k^{E^{(2)}} + \sum_{n=0}^{N/2} \frac{g^{(2)}}{\hbar\omega} f_k f_n c_n^{E^{(2)}} = \frac{E^{(2)}}{\hbar\omega} c_k^{E^{(2)}}\ . \tag{4.7}$$

Solving for $c_k^{E^{(2)}}$ and reinserting the result in Eq. (4.7), one finds the running of the coupling constant $g^{(2)}(N)$ with N:

$$\frac{\hbar\omega}{g^{(2)}(N)} = -\sum_{n=0}^{N/2} \frac{f_n^2}{2n + \frac{3}{2} - E^{(2)}/(\hbar\omega)}\ . \tag{4.8}$$

For given N the two-body spectrum can easily be calculated by diagonalisation. As an example, Figure 4.1 shows the result if one uses the ground state binding energy $E_0^{(2)}$ as renormalisation energy: here $E_0^{(2)} = -1\ \hbar\omega$. The dots at position 0 refer to the exact result determined by equation (2.40). The corresponding scattering length is $a \approx 1.046\, b$ with the oscillator length b. It is clear from this figure, that the model-space results for the excited states approach the exact values in the limit $N \to \infty$. Note that the ground state energy is constant by construction.

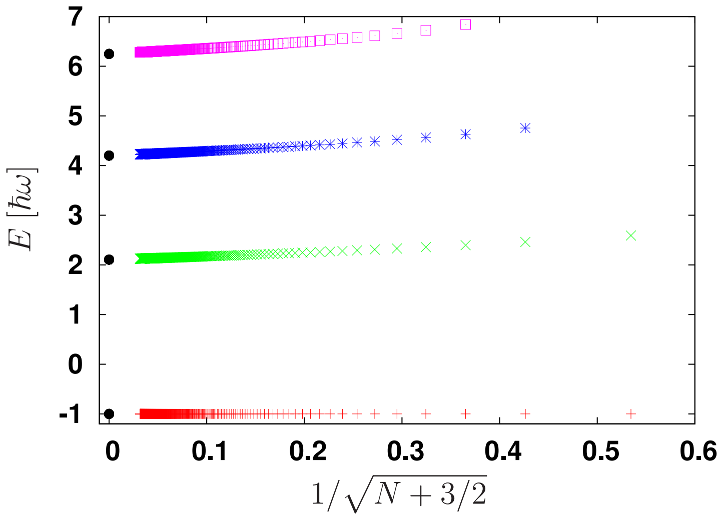

Figure 4.1: Energy spectrum for two bosons in a harmonic confinement in the scaling limit with angular momentum $l = 0$ and renormalisation energy $E^{(2)} = E_0^{(2)} = (-1)\,\hbar\omega$. The dots refer to the exact results determined by equation (2.40).

Renormalisation of $g^{(3)}$: As for $g^{(2)}$, the three-body coupling constant $g^{(3)}$ has to be renormalised for each N characterising the model space. The three-body coupling constant $g^{(3)}$ can be fixed by an energy of the three-body system $E^{(3)}$. Again, the separability of the interaction is exploited for the explicit renormalisation: Let the solution $\left|\alpha_N\right\rangle$ for the three-body system in the model space without the three-body interaction W for some value of N be given by the expansion in harmonic oscillator basis states as

$$\left|\alpha_N\right\rangle = \sum_{n_1 l_1, n_2 l_2, L} Z_N\left(\alpha_N; n_1 l_1, n_2 l_2, L\right) \left|n_1 l_1, n_2 l_2, L\right\rangle , \tag{4.9}$$

with coefficients $Z_N\left(\alpha_N; n_1 l_1, n_2 l_2, L\right)$. The corresponding energy eigenvalues are denoted by $D_N(\alpha_N)$. Note that the eigenstates are degenerate in the total angular momentum projection M. With these states, I calculate the matrix elements for the complete Hamiltonian including the three-body interaction

$$\begin{aligned}\langle\alpha_N\left|H^{(3)}\right|\alpha'_N\rangle &= D_N(\alpha_N)\,\delta_{\alpha_N,\alpha'_N} \\ &+ g^{(3)}(N)\Big(\sum_{n_1,n_2} Z_N\left(\alpha_N; n_1 0, n_2 0, 0\right) f_{n_1} f_{n_2}\Big)\Big(\sum_{n'_1,n'_2} Z_N\left(\alpha'_N; n'_1 0, n'_2 0, 0\right) f_{n'_1} f_{n'_2}\Big) .\end{aligned} \tag{4.10}$$

Requiring the energy of the state $\left|\alpha_N\right\rangle$ to be $E^{(3)}$ for given N, the renormalisation condition for the three-body coupling follows:

$$\frac{1}{g^{(3)}(N)} = -\sum_{\alpha_N} \frac{\Big(\sum_{n_1,n_2} Z_N\left(\alpha_N; n_1 0, n_2 0, 0\right) f_{n_1} f_{n_2}\Big)^2}{D_N(\alpha_N) - E^{(3)}} . \tag{4.11}$$

Note that the expansion coefficients $Z_N\left(\alpha_N; n_1 0, n_2 0, 0\right)$ as well as the eigenvalues $D_N(\alpha_N)$ explicitly depend on N. The full spectrum in a model space for given N can then be determined with these coupling constants by diagonalisation of the Hamiltonian matrix. The general strategy for calculating the Hamiltonian matrix for a system of A identical bosons was described in chapter 3.

4.2 Energy Spectra in the Scaling Limit

After the renormalisation of the coupling constants, it is possible to calculate the energy spectra of the A-body sector for various cutoffs N. In this section results up to $A = 7$ are presented.

4.2.1 Three-Body Sector

To start with, I compare the model-space results in the three-body sector with the exact results in the unitary limit described by equations (2.41) and (2.43).

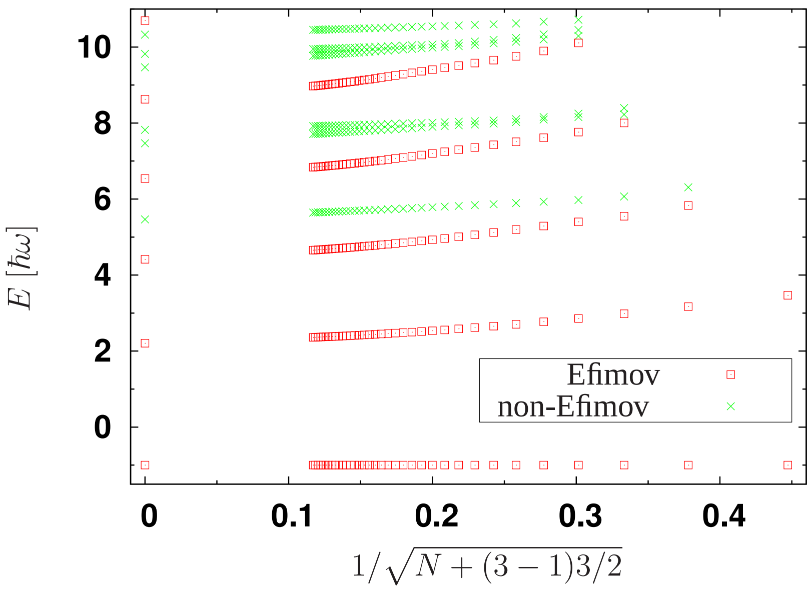

Figure 4.2: Energy spectrum for completely symmetric states of three bosons in a harmonic trap with total angular momentum and parity $L^P = 0^+$ as a function of N and exact analytical results from [18] given at $\lim N \to \infty$. Efimov-like states are indicated by squares, other states are indicated by crosses.

In Fig. 4.2, I show the spectrum for positive parity and total angular momentum $L = 0$ as a function of the cutoff $N \leq 70$. For each N the 3-body interaction was adjusted such that the 3-body ground state has energy $E^{(3)} = (-1)\ \hbar\omega$. As shown by Werner and Castin [18] and mentioned in section 2.3.2, there are two different types of states. On the one hand, there are states independent of the three-body potential W (crosses). On the other hand, there are states which depend on $V^{(3)}$ (squares) and are called Efimov-like. These Efimov-like states are the analogues in the trap of the Efimov states without confinement. The exact results are given at $N \to \infty$. Remarkably, in the model space the non Efimov-like states are not completely independent of W and the coupling constant $g^{(3)}$. The dependence is an artifact of the regularisation method with the cutoff N. Nevertheless, the dependence is in general much weaker than for the Efimov-like states.

For the non-Efimov-like states a linear extrapolation seems appropriate for $N \to \infty$. The Efimov-like states, however, show a definite curvature. In this case, a quadratic term has to be included in the extrapolation. Typical extrapolation errors for Efimov-like states are of order $2 - 3\%$ and less than 1% for the other states.

4.2.2 Four-Body Sector

I now turn to the system of four bosons with angular momentum and parity $L^P = 0^+$. This system is of high experimental interest and the behaviour of the bound states in free space is well known [74, 75]. Figure 4.3 shows the calculated spectrum in the unitary limit as a function of N again for $E^{(3)} = (-1)\ \hbar\omega$. For most of the states there is a strong N dependence and an extrapolation prescription is essential. Efimov-like states are extrapolated with a quadratic polynomial with the constraint that it has no extremum for positive arguments. Some of the extrapolations are shown by the solid lines in Fig. 4.3. Since the exact results are not known, I estimate the uncertainty from the extrapolation conservatively as being equal to the energy shift from the last calculated value to the extrapolated value. This prescription should give an upper bound on the extrapolation uncertainty. Remarkably, with this procedure the estimated uncertainty of the ground is very small and the extrapolation of the ground state has a positive slope in contrast to all other extrapolations. In section 4.3.4.2, this issue will be revisited.

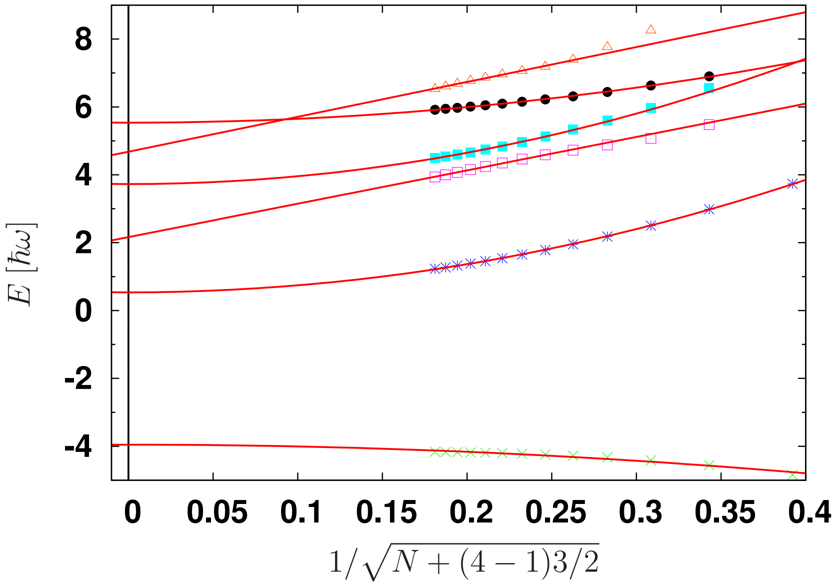

Figure 4.3: Spectrum for symmetric 0^+ states of four identical bosons in the unitary limit for $E^{(3)} = (-1)\ \hbar\omega$ as a function of N. The solid lines indicate the extrapolation to $N = \infty$.

I am now in the position to study the structure of the three- and four-body spectra. In the original Efimov plot, the three-body spectrum is studied for fixed three-body interaction W while the two-body ground-state energy $E^{(2)}$ or, equivalent, the scattering length a is varied [6, 13]. Since there is no four-body interaction at leading order, this plot can be extended to the four-body system and has been studied extensively in free space [74, 75]. I will compare the spectra in the trap with the free space results. In Fig. 4.4, the extrapolated spectra of the symmetric 0^+ four-body states for various $\epsilon^{(2)}$ are shown by filled dots. The three-body interaction is fixed by the requirement, that the three-body ground state lies at $E^{(3)} = (-1)\ \hbar\omega$ in the unitary limit. Additionally, the three-body Efimov-like states are shown as squares. The dotted lines give the upper bound on the extrapolation uncertainties for the lowest two four-body states. The higher excited states are connected by dashed lines to guide the eye. Their extrapolation error is similar but not shown explicitly. The harmonic confinement has a strong effect on the spectrum. Compared to free space, it is no longer true that two four-body states are related to each trimer state. Moreover, the levels appear to be mutually

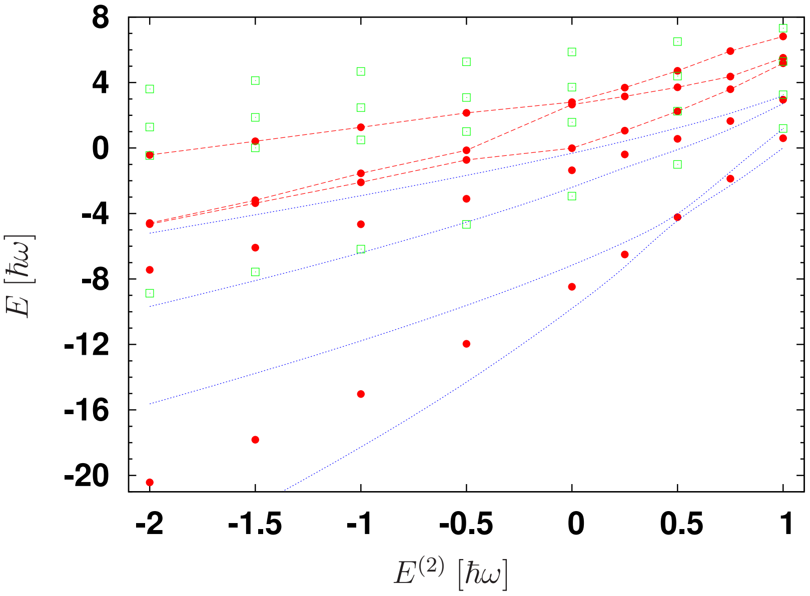

Figure 4.4: Extrapolated spectra of the symmetric 4-body states 0^+ for various $E^{(2)}$ (circles) and 3-body Efimov-like states (squares). The 3-body interaction is fixed such that $E^{(3)} = -1\ \hbar\omega$ in the unitary limit $E^{(2)} = 0.5\ \hbar\omega$. The dotted lines give the upper bound on the extrapolation error for the two lowest states. The dashed lines are guides to the eye.

perturbed: There are various avoided crossings of four-body states, e.g. between the fourth and fifth state around $E^{(2)} \approx 0\ \hbar\omega$ and possibly also between the second and third state. These avoided level crossings could be studied experimentally by varying $E^{(2)}$ using Feshbach resonances.

The dependence on $E^{(2)}$ can be translated into a dependence on the scattering length a using equation (2.40). For $(-2) \leq E^{(2)}/(\hbar\omega) \leq 0$, the scattering length is essentially zero. When $E^{(2)}$ is varied from zero to one, however, the scattering length grows to become infinite at $E^{(2)} = 1/2\ \hbar\omega$, jumps to minus infinity and approaches a negative value close to zero at $E^{(2)} = 1\ \hbar\omega$. This is the most interesting region from the point of universality and corresponds to the usual Efimov plot in free space. In this region, the scattering length is much larger than all other length scales and the effective theory is expected to describe systems of real atoms with van der Waals interactions. The discrete scale invariance of the three- and four-body spectra in free space has disappeared in Fig. 4.4. It would be interesting to approach the free space limit by making the trap wider and wider in experiment in order to see how the discrete scaling symmetry is restored. In the theoretical calculation, taking this limit is computationally very expensive since the absolute value of the energy cutoff for fixed N vanishes as $\beta \to \infty$. Cold atom experiments could serve as a quantum simulator to study this question.

4.2.3 Systems with more Bosons

In this section, I present some results for the five-, six-, and seven-boson system.

In Figure 4.5 a part of the energy spectrum of the five-body states $L^P = 0^+$ is depicted as a function of the cutoff N for $E^{(2)} = E^{(3)} = 0.5\ \hbar\omega$. Calculations are feasible with cutoffs of at most $N = 20$. The extrapolation is done with the typical quadratic polynomial. Remarkably, the behaviour of the ground state is peculiar: it depends on N concavely, in contrast to the excited

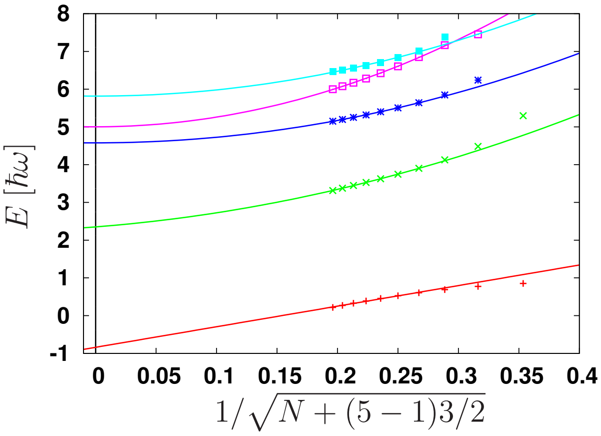

Figure 4.5: Energy spectrum of five-body states $L^P = 0^+$ as a function of the cutoff N in the unitary limit. The three-body interaction is adjusted to fix a three-body Efimov-like state at the energy $E^{(3)} = 0.5\ \hbar\omega$. The extrapolation is usually done with a quadratic polynomial. Due to the concave dependence of N of the ground state, this state is linear extrapolated.

states. In consequence, the extrapolation with the quadratic polynomial is problematic and the energy of the ground state is estimated with a linear extrapolation of the last eigenvalues. The first and second excited state are well described with a quadratic polynomial and conservative uncertainties can be estimated as described above. For higher states there are level crossings for $N \leq 20$ and also in the extrapolated region $N > 20$. But, crossings in the latter region inhibit the extrapolation or compromise its validity. Consequently, for these states extrapolated values have large uncertainties.

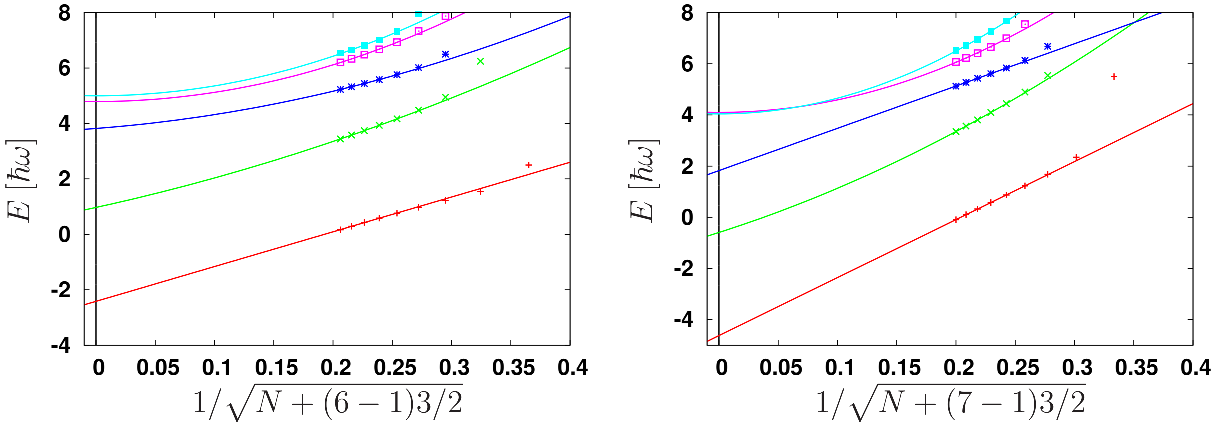

Figure 4.6: Energy spectrum of states with $L^P = 0^+$ versus the cutoff parameter $N \leq 16$ in the unitary limit and $E^{(3)} = 0.5\ \hbar\omega$. The extrapolation is done with a quadratic polynomial. **Left panel**: $A = 6$. **Right panel**: $A = 7$.

As an example for the six-body and seven-body system, Figure 4.6 shows the energy spectrum of states with total angular momentum and parity $L^P = 0^+$ in the unitary limit for $E^{(3)} = 0.5\ \hbar\omega$. All states are extrapolated with the typical convex quadratic polynomial. The maximum cutoff parameter is for both particle system $N = 16$. Note again that extrapolations crossing each other carry larger uncertainties due to possible interaction between these states. An example for this are the adjacent third and fourth excited states for the system with seven bosons $A = 7$.

In summary it can be stated, that the convergence to the exact results is slow and and one has to rely on the extrapolation in the cutoff N. The reason for this ill-conditioned behaviour is the singular nature of the contact interactions. In order to cushion this problematic effect, the genuine contact interactions are approximated by smoothed functions in the following.

4.3 Smeared Contact Interaction

Some results of this section are previously published in [62]. The central point in this section is, that the contact interaction is regularised by smearing. This means, that the contact interactions are replaced by (narrow) Gaussians with width ϵ. (The notation $\epsilon^{(b)} := \epsilon/b$, where b is the oscillator length, is used throughout.) In order to preserve the separability of the interaction the contact interaction

$$\left\langle \vec{s}^{(b)} \middle| V \middle| \vec{s}^{(b)\prime} \right\rangle = g^{(2)} \delta^{(3)}(\vec{s}^{(b)}) \delta^{(3)}(\vec{s}^{(b)} - \vec{s}^{(b)\prime}) = g^{(2)} \delta^{(3)}(\vec{s}^{(b)}) \delta^{(3)}(\vec{s}^{(b)\prime}) \tag{4.12}$$

is substituted by

$$\left\langle \vec{s}^{(b)} \middle| V_\epsilon \middle| \vec{s}^{(b)\prime} \right\rangle = g^{(2)} (2\pi |\epsilon^{(b)}|^2)^{-3/2} e^{-\frac{|\vec{s}^{(b)}|^2}{2|\epsilon^{(b)}|^2}} \; (2\pi |\epsilon^{(b)}|^2)^{-3/2} e^{-\frac{|\vec{s}^{(b)\prime}|^2}{2|\epsilon^{(b)}|^2}} \,, \tag{4.13}$$

and the three-body contact interaction

$$\left\langle \vec{s}_1^{\,(b)}, \vec{s}_2^{\,(b)} \middle| W \middle| \vec{s}_1^{\,(b)\prime}, \vec{s}_2^{\,(b)\prime} \right\rangle = g^{(3)} \delta^{(3)}(\vec{s}_1^{\,(b)}) \delta^{(3)}(\vec{s}_1^{\,(b)\prime}) \delta^{(3)}(\vec{s}_2^{\,(b)}) \delta^{(3)}(\vec{s}_2^{\,(b)\prime}) \tag{4.14}$$

is replaced by

$$\left\langle \vec{s}_1^{\,(b)}, \vec{s}_2^{\,(b)} \middle| W_\epsilon \middle| \vec{s}_1^{\,(b)\prime}, \vec{s}_2^{\,(b)\prime} \right\rangle = g^{(3)} (2\pi |\epsilon^{(b)}|^2)^{-6} \; \exp\Big(- \frac{|\vec{s}_1^{\,(b)}|^2 + |\vec{s}_2^{\,(b)}|^2 + |\vec{s}_1^{\,(b)\prime}|^2 + |\vec{s}_2^{\,(b)\prime}|^2}{2|\epsilon^{(b)}|^2} \Big) \,. \tag{4.15}$$

The case of contact interactions is then recovered in the limit $\epsilon^{(b)} \to 0$.

4.3.1 Matrix Elements and Renormalisation

The calculation of the matrix elements in the oscillator basis for the smeared contact interaction is very similar to those for the genuine contact interaction. According to appendix C.1, the two-body matrix elements can be written as

$$\left\langle n_1 l_1 m_1 \middle| V_\epsilon \middle| n_1' l_1' m_1' \right\rangle = \frac{g^{(2)}}{(1 + |\epsilon^{(b)}|^2)^3} \Big(\frac{1 - |\epsilon^{(b)}|^2}{1 + |\epsilon^{(b)}|^2} \Big)^{n_1 + n_1'} \phi_{n_1 00}(0) \phi_{n_1' 00}(0) \; \delta_{l_1,0} \; \delta_{l_1',0} \; \delta_{m_1,0} \; \delta_{m_1',0} \;, \tag{4.16}$$

$$= \frac{g^{(2)}}{(1 + |\epsilon^{(b)}|^2)^3} \Big(\frac{1 - |\epsilon^{(b)}|^2}{1 + |\epsilon^{(b)}|^2} \Big)^{n_1 + n_1'} \frac{1}{\pi^{\frac{3}{2}}} \sqrt{\frac{(2n_1 + 1)!!}{n_1! 2^{n_1}}} \sqrt{\frac{(2n_1' + 1)!!}{n_1'! 2^{n_1'}}} \; \delta_{l_1,0} \; \delta_{l_1',0} \; \delta_{m_1,0} \; \delta_{m_1',0} \;, \tag{4.17}$$

where the value of the oscillator function at the origin is given by

$$\phi_{n00}(0) = \frac{1}{\pi^{3/4}} \left(\frac{\Gamma(n + \frac{3}{2})}{\Gamma(\frac{3}{2}) \Gamma(n + 1)} \right)^{1/2} = \left(\frac{(2n + 1)!!}{\pi^{3/2} \, n! \, 2^n} \right)^{1/2} \,. \tag{4.18}$$

Likewise, the matrix elements of the smeared three-body contact interaction are given by

$$\big\langle n_1 l_1, n_2 l_2, LM \big| W_\epsilon \big| n_1' l_1', n_2' l_2', L'M' \big\rangle = \frac{g^{(3)}}{(1+|\epsilon^{(b)}|^2)^6} \left(\frac{1-|\epsilon^{(b)}|^2}{1+|\epsilon^{(b)}|^2} \right)^{n_1+n_2+n_1'+n_2'} \phi_{n_1 0}(0) \phi_{n_2 0}(0) \phi_{n_1' 0}(0) \phi_{n_2' 0}(0) \delta_{l_1,0}\, \delta_{l_1',0}\, \delta_{l_2',0}\, \delta_{l_2,0}\, \delta_{L,L'}\, \delta_{L,0}\, \delta_{M,M'}\, \delta_{M,0} \;. \tag{4.19}$$

In the next step, the coupling constants $g^{(2)}$ and $g^{(3)}$ have to be renormalised with respect to the regulator N. As for the genuine contact interactions these coupling constants are fixed with a specific two-body and three-body energy $E^{(2)}$ and $E^{(3)}$. Since the smeared interactions are also separable, only the coefficients in the renormalisation equations (4.8) and (4.11) for the coupling constants $g^{(2)}$ and $g^{(3)}$ have to be modified. With the new definition

$$f_{n\epsilon} := \begin{cases} \phi_{n00}(0)\,, & \text{for contact interactions (i.e. } \epsilon^{(b)} = 0\text{),} \\ (1+|\epsilon^{(b)}|^2)^{-3/2} \left(\frac{1-|\epsilon^{(b)}|^2}{1+|\epsilon^{(b)}|^2} \right)^n \phi_{n00}(0)\,, & \text{for smeared contact interactions.} \end{cases} \tag{4.20}$$

the renormalisation equations yield

$$\frac{\hbar\omega}{g^{(2)}(N)} = -\sum_{n=0}^{N/2} \frac{f_{n\epsilon}^2}{2n+\frac{3}{2}-\frac{E^{(2)}}{\hbar\omega}}\,, \tag{4.21}$$

and

$$\frac{1}{g^{(3)}(N)} = -\sum_{\alpha_N} \frac{\left(\sum\limits_{n_1,n_2} Z_{N\epsilon}\left(\alpha_N; n_1 0, n_2 0, 0\right) f_{n_1\epsilon} f_{n_2\epsilon} \right)^2}{D_{N\epsilon}(\alpha_N) - E^{(3)}}\,. \tag{4.22}$$

Note that the eigenvalues $D_{N\epsilon}$ and the corresponding eigenvectors $Z_{N\epsilon}$ now explicitly depend on the range of the interaction ϵ as well as the cutoff N. Subsequently in section 4.3.4, the energy spectra for various bosonic systems will be discussed. Prior to this, the next sections are devoted to the behaviour of the running coupling constants $g^{(2)}(N)$ and $g^{(3)}(N)$ and an error analysis.

4.3.2 Running of Coupling Constants

In this subsection, I study the running of the coupling constants $g^{(2)}(N)$ and $g^{(3)}(N)$ for contact interactions in detail. Stetcu et al. [77] rewrote the sum in Eq. (4.8) in terms of Γ-functions and the generalised hypergeometric function ${}_3F_2$. They found an explicit relation for $g^{(2)}(N)$ from which the behaviour for large N can be obtained.

Here, I provide an alternative and much shorter derivation of the behaviour of $g^{(2)}(N)$ for large values of N using an integral representation of the sum in Eq. (4.8). For $E^{(2)} < 3/2\;\hbar\omega$ each term in the sum is positive and the denominator grows monotonously. I examine the behaviour for very large N. With the Euler-Maclaurin formula [97] the sum can be approximated as an integral

$$-\frac{\hbar\omega}{g^{(2)}(N)} = \sum_{n=0}^{N/2} \frac{\phi_{n00}^2(0)}{2n+\frac{3}{2}-E^{(2)}/(\hbar\omega)} \tag{4.23}$$

$$= \frac{1}{\pi^{3/2}} \int_1^{N/2} \frac{\Gamma(x+3/2)\,\mathrm{d}x}{\Gamma(3/2)\Gamma(x+1)(2x+\frac{3}{2}-E^{(2)}/(\hbar\omega))} + \mathcal{O}(1)\,, \tag{4.24}$$

where $\phi_{n00}(0)$ was substituted with Eq. (4.18). The quotient of Gamma functions can be expanded in x,

$$\frac{\Gamma(x+3/2)}{\Gamma(3/2)\Gamma(x+1)} = \frac{1}{\Gamma(3/2)}\sqrt{x} + \mathcal{O}\left(1/\sqrt{x}\right) \ . \tag{4.25}$$

Inserting this expansion in Eq. ((4.23)) and integrating, I find

$$\frac{g^{(2)}(N)}{\hbar\omega} = -\frac{\pi^2}{\sqrt{2}}\frac{1}{\sqrt{N}} + \mathcal{O}\left(1/N\right) \ . \tag{4.26}$$

Thus the coupling constant vanishes as $1/\sqrt{N}$. Identifying $\sqrt{N}$ with the momentum cutoff Λ, this is consistent with the renormalisation in free space [78]. I thus expect the leading errors from finite N in the effective theory to scale with $1/\sqrt{N}$.

For $E^{(2)} < 3/2\ \hbar\omega$ the coupling rapidly approaches zero as N is increased. In the case that $E^{(2)} > 3/2\ \hbar\omega$, the terms in the sum in Eq. (4.23) are negative at first until $n > (E^{(2)}/(2\hbar\omega) - 3/4)$. The coupling $g^{(2)}(N)$ as a function of $N \in \mathbb{R}$ thus develops a minimum for $N \to (E^{(2)}/(2\hbar\omega) - 3/4)$ and has a pole as N is increased further. For even larger N it approaches zero as well.

For smeared contact interactions an additional damping factor appears. For Eq. (4.23), one has

$$-\frac{\hbar\omega}{g^{(2)}(N)} = \frac{1}{(1+|\epsilon^{(b)}|^2)^3}\sum_{n=0}^{N/2}\frac{\phi_{n0}^2(0)}{(2n+\frac{3}{2}-\frac{E^{(2)}}{\hbar\omega})}\left(\frac{1-|\epsilon^{(b)}|^2}{1+|\epsilon^{(b)}|^2}\right)^{2n} \tag{4.27}$$

$$= \frac{1}{\pi^{3/2}(1+|\epsilon^{(b)}|^2)^3}\int_0^{N/2}\mathrm{d}x\,\frac{\Gamma(x+3/2)}{\Gamma(3/2)\Gamma(x+1)(2x+\frac{3}{2}-\frac{E^{(2)}}{\hbar\omega})}\left(\frac{1-|\epsilon^{(b)}|^2}{1+|\epsilon^{(b)}|^2}\right)^{2x} + \mathcal{O}(1) \ . \tag{4.28}$$

The integral now converges to a constant for $N \to \infty$ exponentially at a fixed value of $\epsilon^{(b)}$. Thus, the coupling constant converges to a finite number. Note that the larger $\epsilon^{(b)}$ is, the faster the coupling constant converges and the energy spectrum becomes independent of N. This result reflects the additional regularisation of the contact interaction by the smearing.

The inset of Fig. 4.7 illustrates the behaviour of the running coupling constant $\sqrt{N}g^{(2)}$ for $\epsilon^{(b)} = 0$. I show $\sqrt{N}\,g^{(2)}$ in the unitary limit for the renormalisation energies $E^{(2)} = 0.5\ \hbar\omega$ (ground state) and $E^{(2)} = 16.5\ \hbar\omega$ (eighth excited state). In the case of $E^{(2)} = 0.5\ \hbar\omega$, the running coupling $\sqrt{N}\,g^{(2)}$ has already converged to a constant value for small values of N and shows no structure. For $E^{(2)} = 16.5\ \hbar\omega$, the situation is as described above. The coupling constant approaches zero for N around 14 where the denominator of the right hand side of Eq. (4.23) changes sign. Furthermore, it changes from large positive to large negative values around $N = 21$. This behaviour can be understood by looking at the spectrum for $E^{(2)} = 16.5\ \hbar\omega$ shown in Fig. 4.7. For small values of N, the model space is not large enough to describe the deeply-bound ground state adequately. The behaviour of the coupling constant $\sqrt{N}\,g^{(2)}$ is exactly such that this new state enters the renormalised spectrum from minus infinity keeping the other states unchanged. In the continuum case, a similar behaviour is observed for the three-body spectrum [78, 79]. For larger values of N, when the model space is large enough to describe the ground state, the running coupling $\sqrt{N}\,g^{(2)}$ approaches the same value for both cases.

For the coupling constant $g^{(3)}$ the situation is more complicated. The eigenvalues $D_N(\alpha)$ as well as the eigenstates now depend on the cutoff parameter N. Therefore it is not straightforward to derive the leading-order behaviour of $g^{(3)}$ analytically. As mentioned earlier, Werner et al. have provided

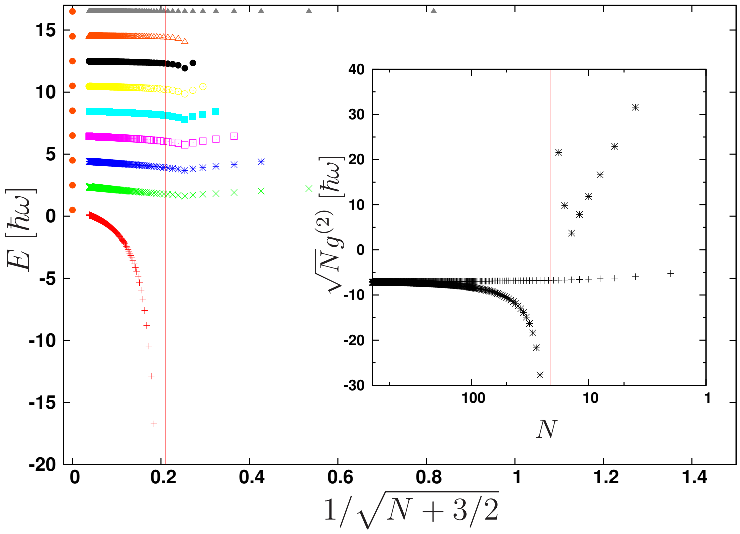

Figure 4.7: Energy spectrum in the two-body sector for $E^{(2)} = 16.5\ \hbar\omega$. The dots on the left show the exact energies. The inset shows the running coupling constants $\sqrt{N}\, g^{(2)}$ in the unitary limit for renormalisation energies $E^{(2)} = 0.5\ \hbar\omega$ and $E^{(2)} = 16.5\ \hbar\omega$ depicted with pluses and stars, respectively.

a semi-analytic solution for the three-body problem in a harmonic trap in the unitary limit [18]. Again, these results for the energy spectrum are used to benchmark my three-body calculations.

In the left panel of Fig. 4.8 the spectrum in the unitary limit for a three-body renormalisation energy $E^{(3)} \approx 1.76\ \hbar\omega$ is depicted as a function of N. At $N = 16$ a new three-body state enters the spectrum of the model space from minus infinity. For large N this state approaches the exact eigenenergy at $-4\ \hbar\omega$. In the inset, the corresponding coupling constant $g^{(3)}$ is shown. As in the two-body case, the coupling constant diverges, here around $N = 16$, and changes from large positive to large negative values. The three-body spectrum and the coupling constant in the continuum case show the same behaviour [78]. The phenomena are the same as in the two-body case discussed above. In the right panel of Fig. 4.8, I present the energy spectra for the renormalisation

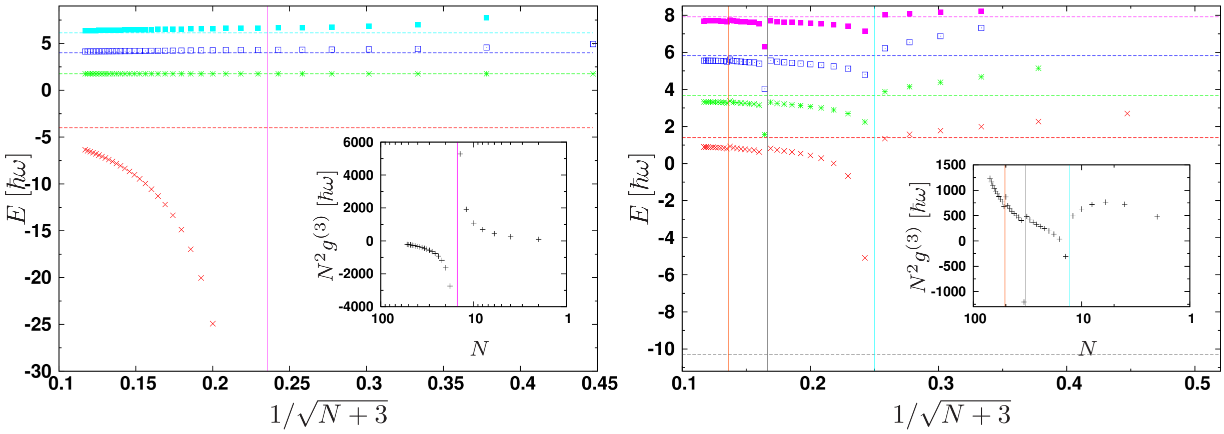

Figure 4.8: **Left panel**: Energy spectrum of Efimov-like states in the three-boson sector in the unitary limit ($E^{(2)} = 0.5\ \hbar\omega$) for $E^{(3)} \approx 1.76\ \hbar\omega$. The dashed lines indicate the exact energies [18]. **Right panel**: Energy spectrum for Efimov-like states in the unitary limit $E^{(2)} = 0.5\ \hbar\omega$ with $E^{(3)} \approx 16.14\ \hbar\omega$ for contact interactions. The running coupling constants $N^2\, g^{(3)}$ corresponding to both cases are shown in the insets. Poles are indicated by vertical solid lines.

$E^{(3)} \approx 16.14\ \hbar\omega$. This renormalisation energy belongs to the following energy spectrum in the full Hilbert space with energy values $E/(\hbar\omega)$: $\cdots$, -5319.28, -10.29, 1.4, 3.68, 5.82, 7.92, 9.99, 12.05, 14.10, 16.14, $\cdots$. The states with energies lower than 1.4 cannot be found inside the feasible model spaces for this renormalisation energy. Remarkably, the states approach the exact energies but at specific values of the cutoff marked by vertical lines the spectrum rearranges. The smallest value of N corresponds to the appearance of a ground state at energy 1.4.

At the two largest cutoff values marked, there are small discontinuities in the energy. These discontinuities are artifacts of the renormalisation method and do not correspond to new states entering the spectrum. Because of the finite model space, not only the Efimov-like states but also the universal states depend very weakly on the three-body interaction. In the special case when for a given cutoff $\bar{N}$ the renormalisation energy $E^{(3)}$ exactly coincides with the eigenvalue of a universal state corresponding to another spectrum with renormalisation energy $\bar{E}^{(3)}$, the computer code used erroneously renormalises to the spectrum characterised by $\bar{E}^{(3)}$. The energy values in the neighbourhood of such points should therefore be discarded.

In the inset of the right panel of Fig. 4.8, the behaviour of the corresponding coupling constant is shown. The coupling constant has a salient behaviour at three positions indicated by the vertical lines. At the smallest value of N where the ground state enters into the spectrum from below, the coupling changes from large positive to large negative values. The approximate pole which is expected at this position due to the discrete nature of the cutoff N is strongly distorted on the right wing due to finite cutoff effects. At the two larger values of N, there are discontinuities due to the renormalisation artifacts discussed above. Moreover, for even larger N the coupling approaches an approximate pole corresponding to the addition of a new ground state at energy $E = (-10.29)\ \hbar\omega$. This pole is not reached in my calculation; it would require a larger N.

4.3.3 Analysis of Uncertainties

There are various sources of uncertainties in my calculation. In this subsection, I perform a detailed analysis of these uncertainties.

First, there are corrections due to the ultraviolet cutoff parameter N. The considerations in subsection 4.3.2 showed that the finite model space also implies an infrared cutoff which vanishes as N is increased. The errors due to both cutoffs show the same scaling behaviour in N. Therefore, one expects corrections in the energy eigenvalues of order $1/\sqrt{N + (A-1)3/2}$ for large N. The shift of N by $(A-1)3/2$ under the square root takes into account the zero-point energy of the free A-body system. I can extract the scaling behaviour of these corrections from the error analysis introduced by Lepage [11]. In Fig. 4.9, I show the deviation of the lowest three-body energy eigenvalues from the exact values in the unitary limit $E^{(2)} = 0.5\ \hbar\omega$ with three-body renormalisation energy $E^{(3)} = -1\ \hbar\omega$. The double-logarithmic plot shows a linear dependence of the energy differences on $\log(N+3)$ for large N values. From a linear fit to the five largest values of N, I find a slope of $s \approx -0.6$ for the first four Efimov states above the state used for renormalisation. The small difference to the expected value of $s = -0.5$ could be due to contamination from higher order corrections. As a consequence, the cutoff dependence for contact interactions is in agreement with power counting arguments based on identifying the momentum cutoff Λ in the continuum theory with $\sqrt{N + (A-1)3/2}$. A similar power law dependence of the leading corrections to three-body energies for contact interactions was observed by Furnstahl et al. [80].

In the case of smeared contact interactions, one finds an exponential dependence on $\sqrt{N}$. In the

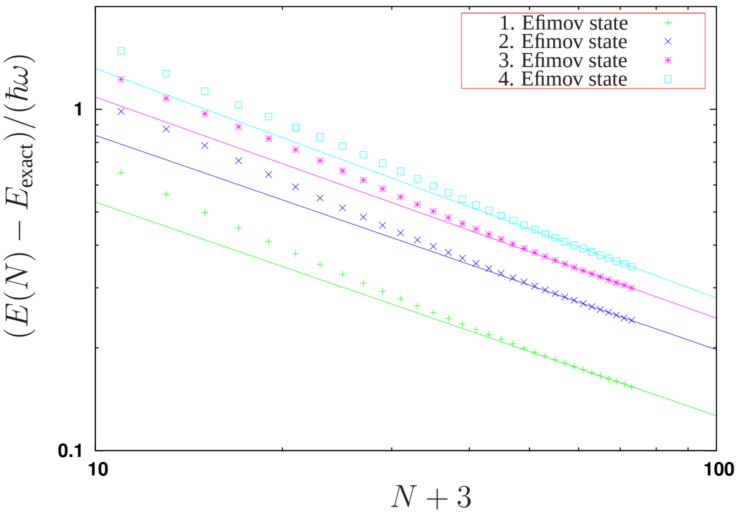

Figure 4.9: Corrections in energy eigenvalues as a function of $N+3$ with $A=3$, $E^{(2)} = 0.5\ \hbar\omega$, $E^{(3)} = -1\ \hbar\omega$.

two-body sector, I consider model spaces with cutoffs up to $N = 700$. In a Lepage plot of $\log(|E_N - E_\infty|)$ one finds for large cutoffs a slope of approximately $s = -0.5$. This implies that for large N the calculated energies behave as

$$E_N \approx E_\infty + c_1 e^{-c_2\sqrt{N}} \ . \tag{4.29}$$

Thus the smearing changes the leading corrections from an inverse power law to an exponential behaviour.

The convergence properties of variational calculations using basis expansions have been studied already in the 1970's [81, 82]. More recently, the convergence properties of ab initio calculations of light nuclei in a harmonic oscillator basis were investigated [73, 83]. Due to their singularity, one expects the contact interactions to behave quite differently, but it is interesting to compare the results with smeared interactions to those of Refs. [73, 83]. However, one has to keep in mind that I consider a physical trapping potential instead of a mere basis expansion. Moreover, in my calculation the effective interaction is renormalised at each N in order to keep the energies of a given two- and three-body state fixed.

My results show the same exponential dependence on the ultraviolet cutoff and on the infrared cutoff $\lambda_{sc} \propto 1/\sqrt{N+3/2}$ as observed by Coon et al. for the Idaho N3LO potential [73]. Furnstahl et al. [83], in contrast, observed a Gaussian dependence on the UV cutoff

$$E_N \approx E_\infty + A_0 e^{-A_1(\sqrt{N})^2} \ , \tag{4.30}$$

using similarity renormalisation group (SRG)-evolved chiral interactions, but their dependence on the infrared cutoff is consistent with mine. For fixed infrared cutoff and an ultraviolet cutoff below the ultraviolet scale of the potential, a Gaussian dependence was also observed in [73]. A better understanding of these observations requires further study.

While extracting the energies for genuine contact interactions from smeared contact interactions, there are also errors due to the width parameter ϵ which corresponds to a finite interaction range. The corresponding two-body problem in free space is separable and can be solved analytically. In my calculations, I determine the coupling constants from matching to energy levels in the oscillator.

One two-body energy level $E^{(2)}$ is kept constant in each model space and the coupling constant $g^{(2)}$ is determined from this matching condition (cf. Eq. (4.8)). One finds:

$$\frac{\hbar\omega}{g_N^{(2)}(\epsilon)} = -\Big(\big(1+|\epsilon^{(b)}|^2\big)\sqrt{\pi}\Big)^{-3} \sum_{n=0}^{N/2} \frac{\left(\frac{1-|\epsilon^{(b)}|^2}{1+|\epsilon^{(b)}|^2}\right)^{2n} \frac{(2n+1)!!}{n!\,2^n}}{2n+\frac{3}{2}-E^{(2)}/(\hbar\omega)}\,, \tag{4.31}$$

$$\xrightarrow{N\to\infty} \big(\big(1+|\epsilon^{(b)}|^2\big)\sqrt{\pi}\big)^{-3} \left(2\frac{E^{(2)}}{\hbar\omega}-3\right)^{-1} {}_2\mathrm{F}_1\left(\frac{3}{2},\frac{3}{4}-\frac{E^{(2)}}{2\hbar\omega};\frac{7}{4}-\frac{E^{(2)}}{2\hbar\omega};\frac{(|\epsilon^{(b)}|^2-1)^2}{(|\epsilon^{(b)}|^2+1)^2}\right)\,, \tag{4.32}$$

where ${}_2\mathrm{F}_1(a,b;c;z)$ denotes a hypergeometric function. The limit $N\to\infty$ yields the coupling constant in the full Hilbert space.

The width $\epsilon^{(b)}$ is used as a smearing parameter and the behaviour for small $\epsilon^{(b)}$ is interesting. Expanding the first and second line of Eq. (4.31), one finds:

$$\begin{aligned} g_\infty^{(2)}(\epsilon^{(b)}) &= -2\pi^{\frac{3}{2}}\,\epsilon^{(b)} - \frac{4\pi^2\Gamma(\frac{3}{4}-\frac{E^{(2)}}{2\hbar\omega})}{\Gamma(\frac{1}{4}-\frac{E^{(2)}}{2\hbar\omega})}\,|\epsilon^{(b)}|^2 \\ &\quad - 2\pi^{\frac{3}{2}}\left(1+4\frac{E^{(2)}}{\hbar\omega}+\frac{4\pi\Gamma(\frac{3}{4}-\frac{E^{(2)}}{2\hbar\omega})^2}{\Gamma(\frac{1}{4}-\frac{E^{(2)}}{2\hbar\omega})^2}\right)|\epsilon^{(b)}|^3 + \mathcal{O}(|\epsilon^{(b)}|^4)\,, \end{aligned} \tag{4.33}$$

$$g_N^{(2)}(\epsilon^{(b)}) = c_0(N,E^{(2)}) + c_2(N,E^{(2)})|\epsilon^{(b)}|^2 + \mathcal{O}(|\epsilon^{(b)}|^4)\,. \tag{4.34}$$

Remarkably, the results for finite and infinite N differ fundamentally since the limits $\epsilon^{(b)}\to 0$ and $N\to\infty$ do not commute. For $N\to\infty$, the coupling constant depends linearly on $\epsilon^{(b)}$ in leading order and vanishes for $\epsilon^{(b)}\to 0$. For finite N, the leading term is independent of $\epsilon^{(b)}$ and the first correction is of order $|\epsilon^{(b)}|^2$. The constant term in $\epsilon^{(b)}$ is a consequence of regularisation with N but the vanishing of the correction linear in $\epsilon^{(b)}$ is unexpected. The expansion parameter $c_0(N,E^{(2)})$ vanishes like $1/\sqrt{N}$ for $N\to\infty$.

The corresponding two-body energies show a similar behaviour. First, the value of $g^{(2)}$ is fixed for a given $\epsilon^{(b)}$ and $E^{(2)}$. The other energies $E_i^{(2)}$ can then be calculated numerically using a root-finding algorithm. For $N=\infty$ and small $\epsilon^{(b)}$ the energies $E_i^{(2)}(\epsilon^{(b)},E^{(2)})$ depend linearly on $\epsilon^{(b)}$. In order to extract the results for a zero-range contact interaction from a calculation with smeared interactions, a linear extrapolation in $\epsilon^{(b)}$ is thus appropriate. For finite N, however, the dependence of the excitation energies $E_i^{(2)}(\epsilon^{(b)},E^{(2)},N)$ on $\epsilon^{(b)}$ is different. For $\epsilon^{(b)}\to 0$, one finds $|E_i^{(2)}(\epsilon^{(b)},E^{(2)},N)-E_i^{(2)}(0,E^{(2)},N)| \propto |\epsilon^{(b)}|^2$ and an extrapolation in $\epsilon^{(b)}$ does not reproduce the result for a zero-range contact interaction. The $\epsilon^{(b)}$-dependence of the energies is illustrated schematically in Fig. 4.10. In order to extract the contact interaction results from smeared interactions, it is therefore important to extrapolate in N first (or use numerically converged values) and then extrapolate to $\epsilon^{(b)}=0$ in a second step.

The variation of the energies with $\epsilon^{(b)}$ can be interpreted as a dependence on the effective range r_0 of the two-body interaction. The effective range parameters in terms of the effective coupling constant $g^{(2)}$ in the continuum case are (See Appendix C.2):

$$\frac{b}{a} = \frac{\sqrt{2}\pi}{g^{(2)}/(\hbar\omega)} + \frac{1}{\sqrt{2\pi}\epsilon^{(b)}} \qquad \text{and} \qquad \frac{r_0}{b} = \sqrt{2}\left(\frac{2\epsilon^{(b)}}{\sqrt{\pi}} - \frac{4\pi|\epsilon^{(b)}|^2}{g^{(2)}/(\hbar\omega)}\right)\,. \tag{4.35}$$

These relations are valid in the full Hilbert space but not in the restricted model space characterised by finite N. Analogous to the case without a trap, my numerical results and equation (4.35) then

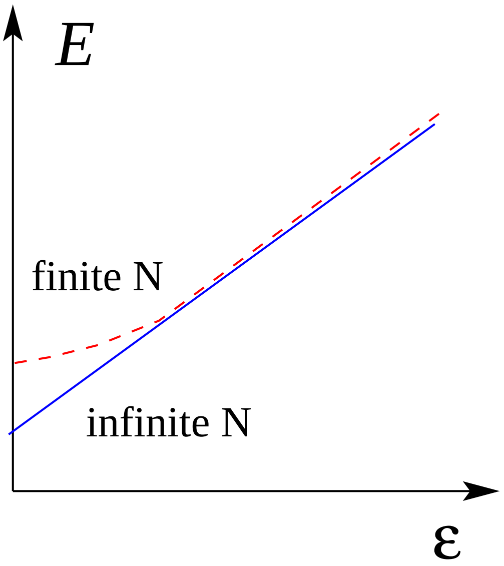

Figure 4.10: Schematic dependence of energies on the smearing parameter $\epsilon^{(b)}$ for finite N (dashed line) and infinite N (solid line).

imply that the leading corrections to the energies $E_i^{(2)}$ for contact interactions are linear in the effective range r_0.

I have also studied the $\epsilon^{(b)}$-dependence in the three-body sector. In the left panel of Fig. 4.11, the corrections from finite $\epsilon^{(b)}$ for finite N are shown. I plot the deviation of results for smeared interactions with $\epsilon^{(b)} \neq 0$ from contact-interactions results with $N = 70$. I focus on the unitary limit for contact interactions, which corresponds to $E^{(2)} = 0.5\ \hbar\omega$. Note that I keep this two-body ground state energy constant while $\epsilon^{(b)}$ is changed. For finite $\epsilon^{(b)}$, the system is not exactly in the unitary limit anymore. For small $\epsilon^{(b)}$ there is a linear dependence in the double-logarithmic plot. The fit yields a slope of approximately $s = 2$ for the state presented, which implies a quadratic dependency of the corrections in $\epsilon^{(b)}$ for $\epsilon^{(b)} \to 0$ in agreement with the behaviour in the 2-body sector.

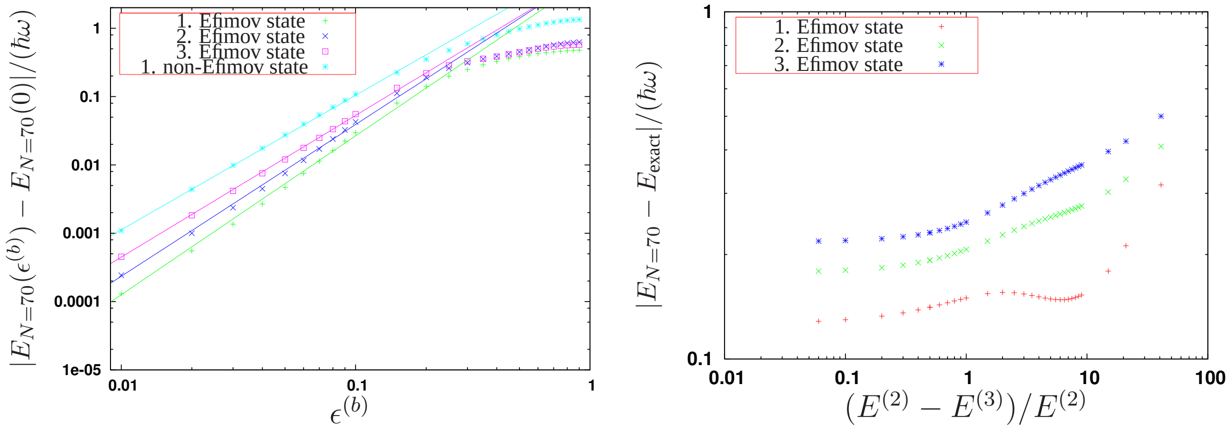

Figure 4.11: **Left panel**: Corrections in energy eigenvalues as a function of $\epsilon^{(b)}$ with $A = 3$, $E^{(2)} = 0.5\ \hbar\omega$, $E^{(3)} = 0.5\ \hbar\omega$. **Right panel**: Corrections as a function of $(E^{(2)} - E^{(3)})/E^{(2)}$ for the unitary limit with $A = 3$.

Finally, there are corrections from a mismatch in renormalisation energies $E^{(2)}$ and $E^{(3)}$. In an effective theory, only states with excitation energies small compared to the cutoff scale of the effective theory can be described. Clearly, the renormalisation energies must be chosen in this energy range. For $E^{(2)} \neq E^{(3)}$, we expect errors governed by $(E^{(2)} - E^{(3)})$ from the mismatch in the two- and three-body renormalisation energies. For contact interactions ($\epsilon^{(b)} = 0$), I have investigated the errors in $(E^{(2)} - E^{(3)})$ numerically. For this purpose, I chose the unitary limit and varied $E^{(3)}$. The right panel of Fig. 4.11 shows the deviation of the exact results from results in the model space for various $(E^{(2)} - E^{(3)})$. As expected, the corrections grow with increasing $|E^{(2)} - E^{(3)}|$. Thus in practise, it is desirable to choose $E^{(2)} \approx E^{(3)}$ to minimise this type of errors.

4.3.4 Energy Spectra

With these insights, now the energy spectra of A-boson systems are studied for $A = 3, 4, 5, 6$ in a trap. The spectra are obtained from two different numerical calculations:

(1) contact interactions and extrapolations in $1/\sqrt{N + (A-1)3/2}$ are studied as in section 4.2, and alternatively

(2) smeared contact interactions and linear extrapolations in the width parameter $\epsilon^{(b)}$ of the converged results in N are investigated.

The difference between the two methods will be used to estimate the errors in my calculation.

4.3.4.1 Three Identical Bosons

At first, the 3-boson sector is considered. In the left panel of Fig. 4.12, the eigenvalues of the first excited $L^\pi = 0^+$ state are shown as a function of the cutoff parameter $N \leq 70$ for various smearing parameters $\epsilon^{(b)}$ in oscillator lengths β. The corresponding renormalisation energies are $E^{(2)} = 0.5$ and $E^{(3)} = -1$. For small model spaces the results are identical for all interaction widths. With increasing interaction width ϵ the eigenvalues converge for smaller values of N. The converged

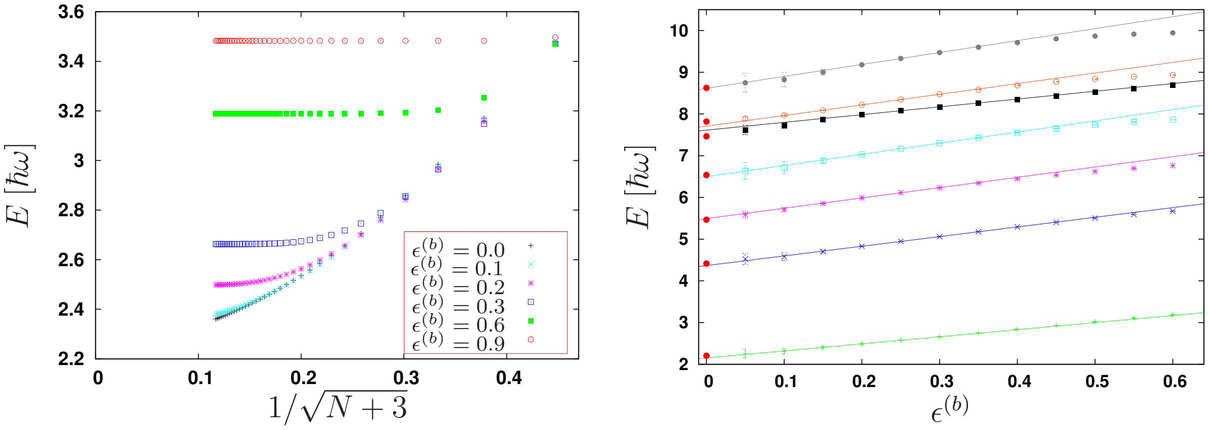

Figure 4.12: **Left panel**: Eigenvalue for the first excited $L^\pi = 0^+$ state with $A = 3$ as a function of N with $E^{(2)} = 0.5\ \hbar\omega$ and $E^{(3)} = -1\ \hbar\omega$ for various $\epsilon^{(b)}$. **Right panel**: The converged eigenvalues as a function of $\epsilon^{(b)}$. $L^\pi = 0^+$, $E^{(2)} = 0.5\ \hbar\omega$ and $E^{(3)} = -1\ \hbar\omega$. The points at $\epsilon/b = 0$ denote the exact eigenvalues from [18]. The dashed lines are linear fits to the values for $\epsilon/b \leq 0.3$ used to extrapolate to $\epsilon/b = 0$.

eigenvalues do not coincide with the results for contact interactions. However, as discussed in the previous section, the parameter ϵ can now be used as a extrapolation parameter instead of N.

The converged eigenvalues are given as a function of ϵ in the right panel of Fig. 4.12 for the five lowest $L^\pi = 0^+$ excited states. The solid lines are linear extrapolations of the data points for $\epsilon/b \leq 0.3$ and the results agree with the exact values known for contact interactions in the unitary limit [18] within 3% errors. The error bars of the data points are estimated by the difference of the eigenvalues related to the two highest cutoff parameters N, i.e. with these two eigenvalues the exact one is approximated by linear extrapolation and the error is estimated as the difference between the state with the highest cutoff parameter and the estimated one. In Fig. 4.12 the two model space sizes correspond to $N = 70$ and $N = 68$.

In Fig. 4.13, the spectra of Efimov-like states are depicted in the unitary limit ($E^{(2)} = 0.5\ \hbar\omega$) for $E^{(3)} = 0.5\ \hbar\omega$ and $E^{(3)} = -4\ \hbar\omega$ in order to illustrate the significance of the mismatch in renormalisation scales. With a linear extrapolation the exact values for $E^{(3)} = -4\ \hbar\omega$ are too low systematically. For larger $E^{(3)}$ the extrapolation in N achieves better results than a linear extrapolation in ϵ. This method clearly has larger errors for $E^{(3)} = -4\ \hbar\omega$.

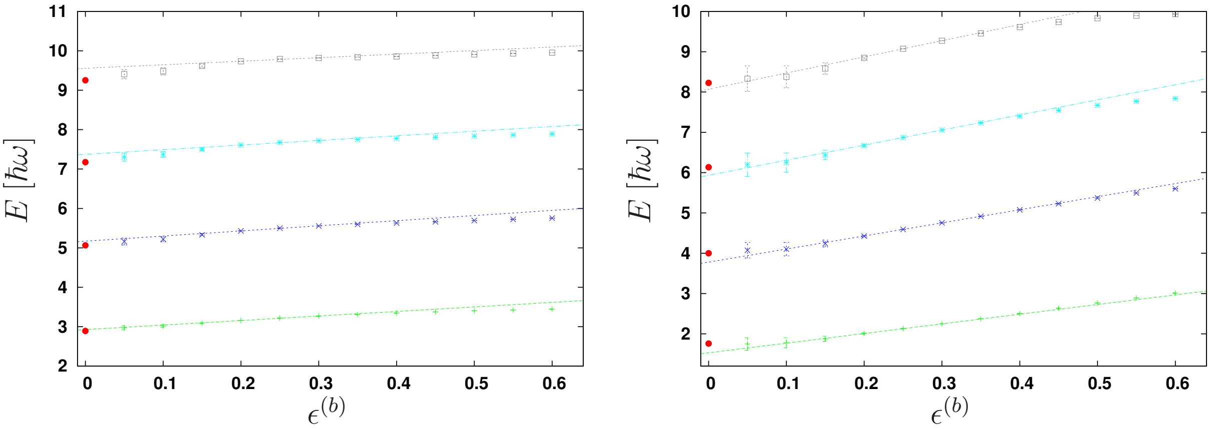

Figure 4.13: Spectrum of Efimov-like $L^\pi = 0^+$ states with $A = 3$ in the unitary limit as a function of ϵ. At $\epsilon/b = 0$ exact eigenenergies are drawn in. **Left panel**: Renormalisation energy $E^{(3)} = 0.5\ \hbar\omega$. **Right panel**: Renormalisation energy $E^{(3)} = -4\ \hbar\omega$.

Finally, Fig. 4.14 shows a non-unitary example with $E^{(2)} = -2\ \hbar\omega$. In the left panel the eigenvalues for the renormalisation energy $E^{(3)} = -1\ \hbar\omega$ are shown as a function of the width ϵ and in the right panel for $E^{(3)} = -5\ \hbar\omega$. The results are linearly extrapolated as in the unitary limit. At $\epsilon/b = 0$ the results for contact interactions extrapolated with a quadratic polynomial in $1/\sqrt{N+3}$ are added. The uncertainties from the extrapolation are estimated conservatively as the energy shift from the last calculated eigenvalues to the extrapolated one. Inside relative errors of 3.5% referred to the ground state with eigenenergy $-5\ \hbar\omega$ respectively $-1\ \hbar\omega$ both results coincide. This method clearly has larger errors for $E^{(3)} = -5\hbar\omega$.

4.3.4.2 Four Identical Bosons

In section 4.2.2, results for a 4-boson system have been presented with contact interactions. Here these calculations are revisited using smeared interactions. For instance, calculations for the unitary

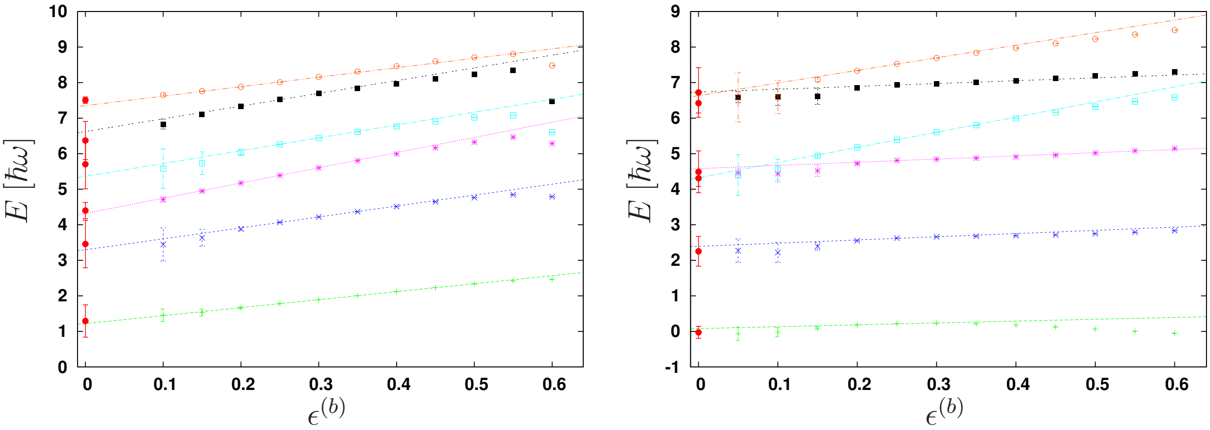

Figure 4.14: $L^\pi = 0^+$ eigenvalues for $A = 3$ as a function of ϵ with $E^{(2)} = -2\ \hbar\omega$. The points at $\epsilon/b = 0$ denote the extrapolated results for contact interactions. The lines are linear extrapolations to $\epsilon/b = 0$. **Left panel**: $E^{(3)} = -1\ \hbar\omega$. **Right panel**: $E^{(3)} = -5\ \hbar\omega$.

limit $E^{(2)} = 0.5\ \hbar\omega$ with $E^{(3)} = -1\ \hbar\omega$ with contact interactions $\epsilon/b = 0$ are compared to calculations with $\epsilon/b \neq 0$. In my calculation I can reach cutoff values up to $N = 26$ which is significantly smaller than in the three-body sector. In Fig. 4.15, the eigenenergies for the ground and for the first excited states are shown for various model-space sizes. The solid lines are extrapolations with quadratic polynomials in $1/\sqrt{N + (4-1)3/2}$. As in the three-body sector the eigenvalues converge in N more rapidly for larger smearing parameters ϵ. However, for smeared interactions the eigenvalues of the ground state increase at first until they reach a maximum and begin to decrease only afterwards. It is conceivable that for contact interactions and $\epsilon/b = 0.1$ the model spaces are too small in order to see the decrease of the eigenvalues. Thus, the extrapolation given in the left panel of Fig. 4.15 could have large systematic errors. Since contact interactions can behave quite differently from smeared interactions, however, a definite answer requires calculations at larger cutoffs N which however are beyond the scope of this work. If the renormalisation energies $E^{(2)}$ and $E^{(3)}$ are chosen equal, the non-monotonous behaviour in ϵ does not appear and becomes more pronounced only as the mismatch between $E^{(2)}$ and $E^{(3)}$ is increased. The excited states do not show the non-monotonous behaviour in ϵ at all. Their eigenvalues decrease monotonously with ϵ

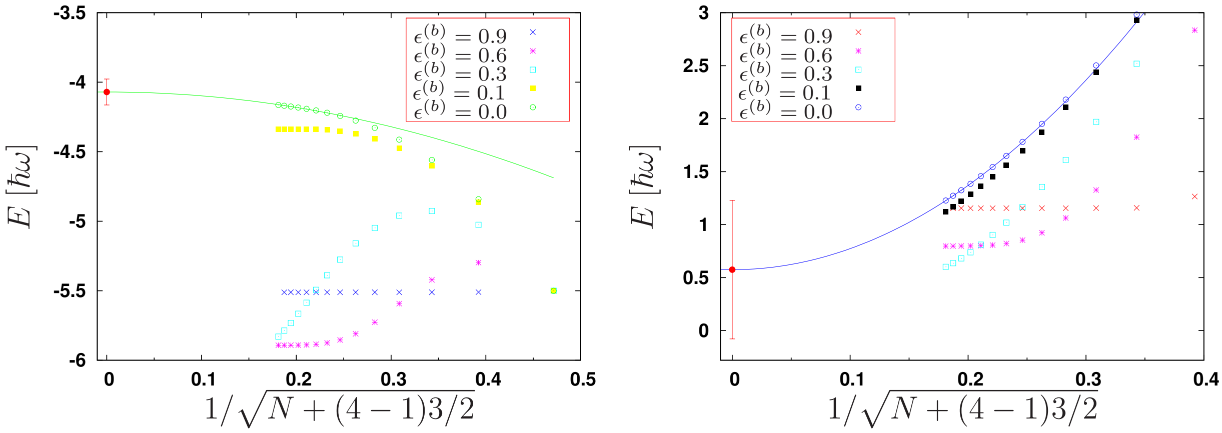

Figure 4.15: Four-boson $L^\pi = 0^+$ states with $E^{(2)} = 0.5\ \hbar\omega$ and $E^{(3)} = -1\ \hbar\omega$ for various smearing parameters ϵ as a function of $1/\sqrt{N + 4.5}$. **Left panel**: Ground state. **Right panel**: First excited state. Solid lines are polynomial extrapolations.

and for large ϵ they converge inside the model-space sizes considered here.

Fig. 4.16 (left panel) shows the converged or extrapolated eigenvalues as a function of ϵ for the three lowest states with renormalisation energies $E^{(2)} = 0.5\ \hbar\omega$ and $E^{(3)} = -1\ \hbar\omega$. In comparison to the three-body sector, the Hamiltonian can be diagonalised only in small model spaces (up to $N = 26$). Thus, just until $\epsilon/b = 0.35$ the eigenvalues have small error bars. The states are linearly extrapolated to $\epsilon/b = 0$. At $\epsilon/b = 0$ the eigenstates extrapolated via N with a quadratic polynomial in $1/\sqrt{N + (4-1)3/2}$ and their estimated uncertainties are shown. For $\epsilon/b < 0.25$ the eigenvalues for the ground states cannot be determined with acceptable accuracy. The extrapolated results differ significantly and are at odds with each other for the ground state. This is due to the non-monotonic behaviour of the ground state energy with ϵ/b discussed above. For the excited states this problem is absent and the results of the two extrapolations are compatible. In the right panel of Fig. 4.16, I show the results for $E^{(3)} = 0.5\ \hbar\omega$. Since $E^{(2)} = E^{(3)}$, one expects less uncertainties for a fixed ϵ than for the case $E^{(2)} \neq E^{(3)}$ (see section 4.3.3). In particular, the ground state energies show no non-monotonous dependence on ϵ and the extrapolations in ϵ and N are consistent.

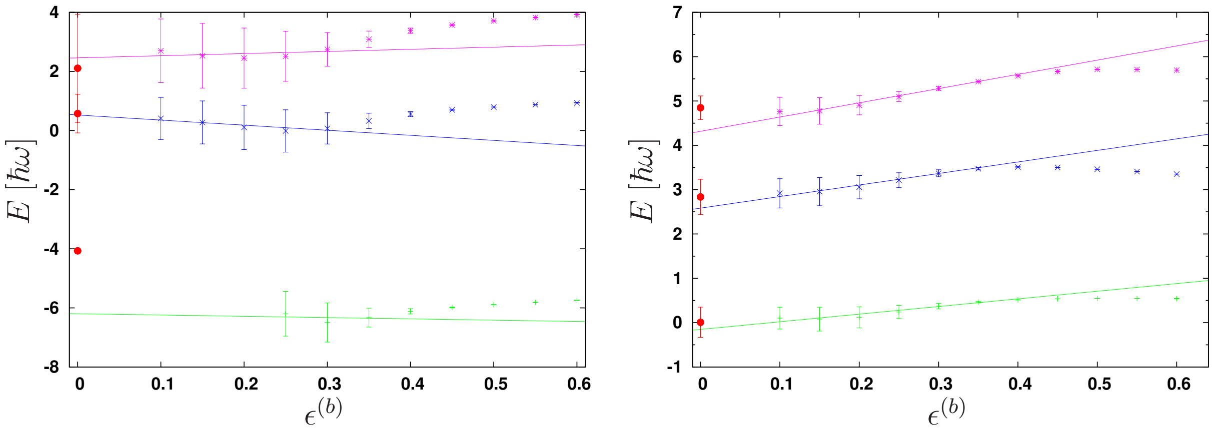

Figure 4.16: Lowest three energy states $L^\pi = 0^+$ for $E^{(2)} = 0.5\ \hbar\omega$ as a function of ϵ for $A = 4$. **Left panel**: $E^{(3)} = -1\ \hbar\omega$. **Right panel**: $E^{(3)} = 0.5\ \hbar\omega$. The eigenvalues are linearly extrapolated. At $\epsilon/b = 0$ extrapolated eigenvalues for contact interactions drawn in.

4.3.4.3 Five and Six Identical Bosons

The combined extrapolation technique is now applied to perform exploratory calculations of the spectra of five and six identical bosons. In order to keep the uncertainties as small as possible, the renormalisation energies are chosen to be identical, i.e. $E^{(2)} = E^{(3)} = 0.5\ \hbar\omega$. In particular, this removes the problem of the non-monotonous behaviour of the energies as a function of ϵ discussed above for the four-body system. The cutoff parameter is $N = 20$ for five bosons and $N = 16$ for six bosons.

The results for the three lowest energy $L^\pi = 0^+$ states with different smearing parameters ϵ are depicted in Fig. 4.17. Due to the small model spaces, the uncertainties are significantly larger than for three and four bosons. The eigenenergies for contact interactions are extrapolated in N with a polynomial of second order in $1/\sqrt{N + (A-1)3/2}$. They are shown at $\epsilon/b = 0$ with conservative error bands. These approximated eigenvalues are consistent with extrapolations in ϵ for smeared contact interactions inside the error bands. Thus I conclude that the combined extrapolation in N

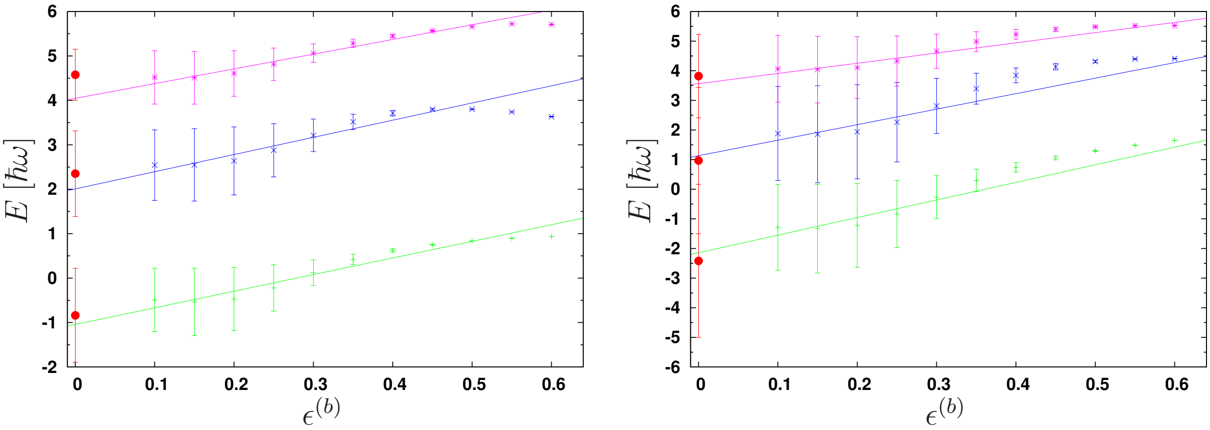

Figure 4.17: Lowest three energy states $L^\pi = 0^+$ for $E^{(2)} = 0.5\ \hbar\omega$, $E^{(3)} = 0.5\ \hbar\omega$ as a function of ϵ. **Left panel**: $A = 5$ ($N = 20$). **Right panel**: $A = 6$ ($N = 16$). The solid lines are linear extrapolations in ϵ. At $\epsilon/b = 0$ the eigenvalues extrapolated with a polynomial of second order in $1/\sqrt{N + (A-1)3/2}$ for contact interactions drawn in.

and ϵ makes calculations in five- and six-boson systems with moderate computational resources possible.

In Table 4.1, the extracted energies of the lowest three Efimov-like states are collected for the unitary limit ($E^{(2)} = 0.5\ \hbar\omega$) and a three-body ground state energy fixed to $E^{(3)} = 0.5\ \hbar\omega$ (cf. Figs. 4.13, 4.16, and 4.17). The numbers in the first two columns are the exact values for $A = 2$ and $A = 3$ rounded to two digits of accuracy. The values for the columns labelled $A = 4$, $A = 5$, and $A = 6$ are extracted from my calculations. Here the number in parentheses gives the difference in the last digit between the extrapolation in N and ϵ which can serve as an estimate of the numerical error. The spectra are much more compressed than the corresponding free space results [25, 74, 75, 84–86]. However, a similar pattern can be observed: starting from $A = 3$, every A-body state is accompanied by a corresponding $(A+1)$-body state. However, a second $(A+1)$-body state attached to the A-body state is not present in my calculation. It would be interesting to study the spectra also away from the unitary limit for fixed $E^{(3)}$ to investigate their systematics. However, due to the additional errors from the mismatch in $E^{(2)}$ and $E^{(3)}$ this is numerically more challenging.

$A = 2$	$A = 3$	$A = 4$	$A = 5$	$A = 6$
0.5	0.5	-0.1(2)	-0.9(2)	-2.3(3)
2.5	2.9	2.7(3)	2.2(3)	1.1(2)
4.5	5.1	4.6(5)	4.3(5)	3.7(3)

Table 4.1: Energies of the three lowest Efimov-like states in systems with $A = 3, 4, 5, 6$ for the renormalisation energies $E^{(2)} = 0.5\ \hbar\omega$ corresponding to the unitary limit and $E^{(3)} = 0.5\ \hbar\omega$. The column labelled $A = 2$ contains the three lowest two-body states. All energies are in units of $\hbar\omega$.

4.4 Conclusion

In this chapter I have studied the physical systems with up to seven identical bosons in a confining of the harmonic oscillator potential. Due to the assumption that the boson-boson scattering length dominates the effective range expansion, interactions between the bosons are approximated with two-body and three-body contact interactions, i.e. the scaling limit. The energy spectra of the A-boson systems have been determined with the shell-model approach introduced in chapter 3 in the model spaces spanned by finite oscillator bases for a given cutoff parameter N. Here, the running coupling constants $g^{(2)}(N)$ and $g^{(3)}(N)$ are renormalised and adjusted to reproduce two given energy states $E^{(2)}$ and $E^{(3)}$ in the two-body and three-body system.

To start with, I have referred to the spectrum for the three-boson system for the total angular momentum and parity $L^P = 0^+$. It consists of two types of states. There are states independent of the three-body interaction and the Efimov-like states, the analogues in the trap to the Efimov states without confinement. Afterwards, the spectrum for four-bosons and it dependence on the renormalisation energy $E^{(2)}$ has been investigated. The first part of this chapter has been completed with selected energy spectra for systems with up to seven bosons.

However, I have found a slow convergence of the energy spectrum in dependence of the cutoff parameter N. This problem has lead to the substitution of the contact interactions with narrow separable Gaussians with width ϵ, so-called smeared contact interactions. The new parameter ϵ has been used as another extrapolation parameter in order to determine the energy spectra and for various A-boson systems the results have been presented. Remarkably, this new approach indicates larger uncertainties in the N-extrapolated energy values for contact interactions than expected previously.

Additionally, the behaviour of the running coupling constants $g^{(2)}(N)$ and $g^{(3)}(N)$ has been studied. In particular, the consequences of different renormalisation energies has been investigated. Finally, in a detailed error analysis the interplay of the finite cutoff parameter N, and the finite width ϵ has been studied. It results in the following prescription to determine the energy values: Use converged results in the cutoff parameter N for finite width ϵ or extrapolate in the cutoff parameter N first and then extrapolate in the width ϵ linearly.

Chapter 5

Clusters of Helium Atoms

This chapter is devoted to physical systems without external confinements. I shall concentrate on the formation of ^{4}He-clusters consisting of A constituents. The following work is done in collaboration with Prof. Forssén, Chalmers University, Gothenburg. His research group delivers the matrix elements in the harmonic oscillator basis of two- and three-body interactions and evolved the genuine interactions with similarity renormalisation group (SRG) transformations.

5.1 Introduction

As mentioned in section 2.5.2, the existence of $^4\mathrm{He}_A$-atom clusters with A constituents could be shown by Schöllkopf et al. in experiments based on diffraction of helium clusters from a transmission grating [21]. Within their experiments the resolution is sufficient to separate cluster with different numbers of constituents. However, the binding energies of these clusters cannot be directly determined. Only the dimer binding energy E_2^B can be estimated by means of its measured size of $\langle r \rangle \approx 4$ Å to be around $E_2^B = 1.1^{+0.3}_{-0.2}$ mK [22].

This result is consistent with predictions by ab initio potentials like TTY or LM2M2 with $E_2^B = 1.30962$ mK [6] and $E_2^B = 1.302$ mK [25], respectively. For larger clusters there are no measurements of binding energies, only predictions based on such ab initio potentials exist. Results from several ab initio potentials are collected in [23].

For up to $A = 10$ atoms predictions for the ground state binding energies E_A^B based on the ab initio potential LM2M2 are calculated with Monte-Carlo methods by Blume et al. [24]. These predictions will be later used as benchmark results.

Furthermore, Gattobigio et al. [25] have proposed an effective parametric potential for the LM2M2 ab initio potential consisting of attractive Gaussian two-body potentials and a repulsive Gaussian three-body interactions. We call this effective potential the Pisa potential due to the research location of the majority of the research collaboration involved. With their technique described in [87] using the hyper-spherical harmonic expansion they determined predictions of binding energies for up to clusters of $A = 6$ atoms.

In the following sections we use the shell-model approach introduced in chapter 3 to calculate the binding energies of the ground states of $^4\mathrm{He}_A$ clusters with angular momentum and parity $L^P = 0^+$. The atom with the ^{4}He isotope as nucleus is a spinless boson. Thus, the spatial wave function of a $^4\mathrm{He}_A$ cluster has to be symmetric under permutation of atoms as assumed in this shell-model approach. To start with, the unevolved LM2M2 potential is used as the interaction between the A constituents in section 5.2. As we will see the slow convergence in the cutoff parameter N due to the hard core of the LM2M2 potential requires the SRG evolution of this potential. Results for various evolution parameter Λ are presented for up to $A = 10$ in section 5.3. Furthermore, the binding energies for up to twelve atoms are determined based on the Pisa potential in section 5.4. Depending on the strength of three-body interaction we distinguish between soft and hard Pisa potentials. For the soft Pisa potential results are summarised in section 5.4.1. The hard version of the Pisa potential is studied in section 5.4.2 and we will see in section 5.4.2.1 that this version has a slower convergence in the cutoff parameter N. Therefore the SRG-evolution is also utilised for this potential and the results are shown in section 5.4.2.2.

5.2 LM2M2 Potential

In this section, we present our results for atomic ^{4}He clusters consisting of up to ten constituents using the LM2M2 potential. The LM2M2 potential is an ab initio potential for ^{4}He atoms constructed by Aziz et al. [23, 88]. Its specification is given in appendix E. In the following the unit of length au means Bohr radius: 1 au $\approx 0.5 \cdot 10^{-10}$ m.

In the left panel of Fig. 5.1, we show the LM2M2 potential as a function of the distance between two ^{4}He atoms. Around $r = 3$ Å the potential has its minimum with a depth of about -11 K. At $r = 2.5$ Å the hard core starts and reaches the finite but huge value of $V(0) = 1.9$ MK at the origin. For $r \to \infty$ the potential approaches zero from below.

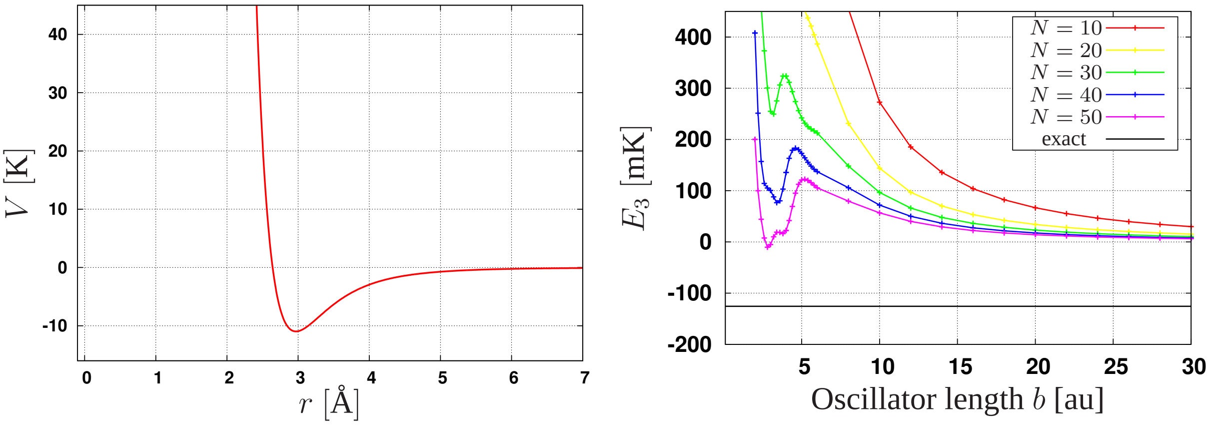

Figure 5.1: **Left panel**: LM2M2 potential in position space. **Right panel**: Spectrum with LM2M2 potential for the ground state of $^4\mathrm{He}_3$ as a function of the oscillator length b for various cutoffs N. Convergence couldn't be achieved. The horizontal solid line indicates the ground state energy $E_3 = -125.8$ mK from the literature [89].

Because of the hard core repulsion, the potential mixes the low and high energy regime strongly. As a consequence, we expect a slow convergence in the energy cutoff of the model space N. This is illustrated in the right panel of Fig. 5.1 where the ground state energy E_3 of the ^{4}He trimer $^4\mathrm{He}_3$ is presented as a function of the oscillator length b which here is a variational parameter. Up to $N = 50$, no convergence is achieved for the trimer energy. Except for the largest value of N, the trimer even seems to be unbound. The exact value for the binding energy in the literature is $E_3^B = 125.8$ mK according to Motovilov et al. [89].

Working with the genuine LM2M2 potential is therefore not a viable option and alternative strategies have to be applied. In the following, we will consider two such strategies:

(1) Use an SRG-evolved version of the LM2M2 potential. As discussed above, this will generate a softer potential accompanied by induced many-body forces that capture the physics of the hard core.

(2) Construct softer effective parametric two- and three-body potentials that reproduce the two- and three-body bound state energies of LM2M2 by adjusting the parameters. We will refer to this effective potential as the Pisa potential.

Both approaches will be discussed below.

5.3 SRG-Evolved LM2M2 Interaction

The SRG is a powerful technique to generate unitarily equivalent interactions with better convergence properties in many-body calculations. In the case of the LM2M2 potential the interaction is softened at the expense of introducing many-body forces.

We have evolved the LM2M2 interaction using the flow equation in Eq. (2.49) as outlined in section 2.4. It turns out that for the LM2M2 potential, the evolution of induced three- and higher-body forces is computationally very expensive since a large number of partial waves contributes. We were not able to carry out the evolution of the induced three-body forces far enough to achieve a significant softening of the two-body interaction.

In the following, as a pilot study we will therefore perform calculations of A-body systems with $A = 4$ up to $A = 10$ neglecting these induced many-body forces. Apart from the parameter of the ultraviolet cutoff of the model space N and the oscillator length b as a variational parameter, there is the SRG parameter Λ which specifies the evolution status. For $\Lambda = \infty$ the potential is unevolved and $\Lambda = 0$ corresponds to the furthest evolution. A variation of the SRG parameter Λ allows to estimate the error from the omitted induced forces in our calculations.

In the left panel of Fig. 5.2, we collect the eigenenergies for the model space with cutoff parameter $N = 30$ as a function of the oscillator parameter b for various Λ. There are minima in the energy for certain ranges of values b_{min} which become more pronounced and form broader plateaus as Λ decreases. In Table 5.1 the positions of the minima b_{min} are collected for various Λ.

Λ	5	1	0.75	0.5	0.25
b_{min}	3.8	4.8	5.6	8.0	10

Table 5.1: Positions of the minima b_{min} in the eigenenergies for $A = 4$ with SRG-evolved LM2M2 potential for various flow parameters Λ. Λ is given in units of $(\text{au})^{-1}$ and b_{min} in units of au.

The energies at the minima appear to converge to a certain value. In order to investigate this convergence, we plot the energies of the minima as a function of $1/N$ for different Λ in the right panel of Fig. 5.2. For $\Lambda \leq 1\ (\text{au})^{-1}$, the calculations have obviously converged but different Λ lead to different values for the binding energy. This spread is due to the missing induced three-body forces and can be used to estimate the error due to their omission.

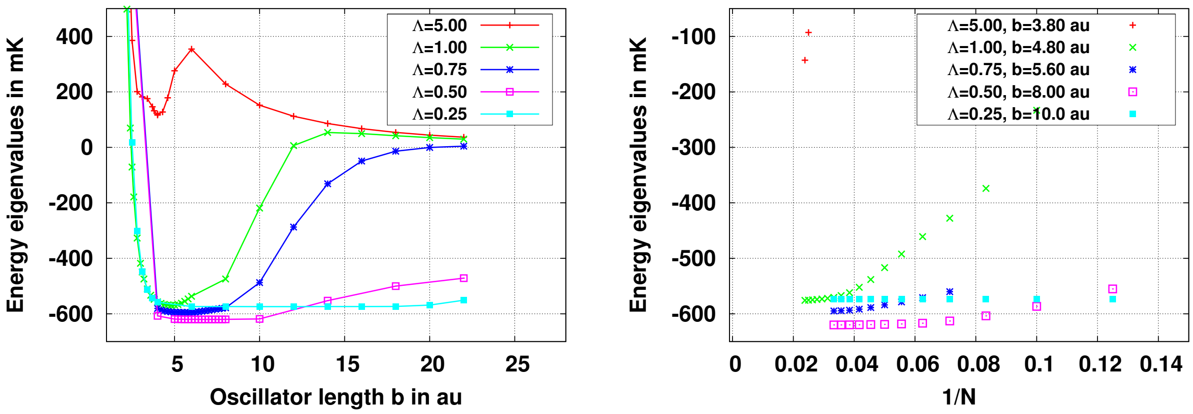

Figure 5.2: Ground state energy of $^4\mathrm{He}_4$ determined with SRG-transformed LM2M2 potential. **Left panel**: Energies as a function of b for cutoffs $N = 30$ for various Λ. **Right panel**: Energies as a function of $1/N$ for various Λ inside the minimum in b.

The determination of the estimated result for the full Hilbert space is based on extrapolation to $N \to \infty$. Since the exact relation between the energy eigenvalues and the cutoff N is unknown, we apply the procedure illustrated in Figure 5.3. The last two data points are extrapolated linearly to the infinite N limit. This gives our first estimate. The other estimate is given by the last data point itself. Our final value is the arithmetic average of these two points while their spread is taken as the uncertainty. We have tested this procedure in cases where convergence has been reached and found that the exact value is always reproduced within errors by this extrapolation.

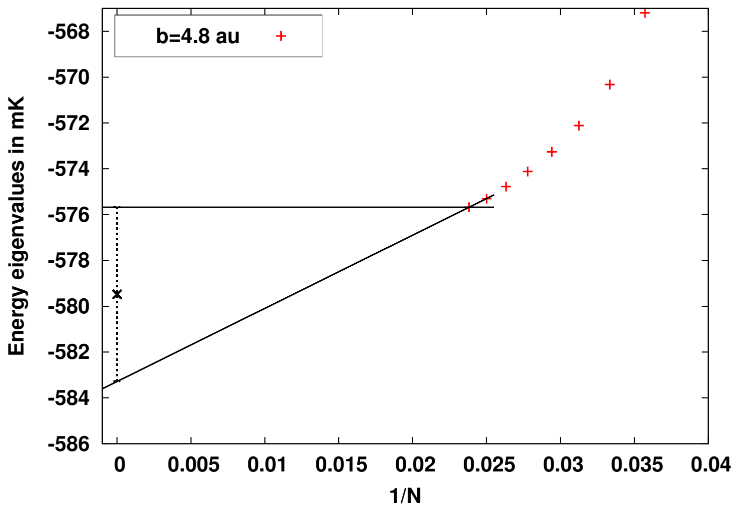

Figure 5.3: Illustration of the extrapolation procedure for the example of ground state energy of $^4\mathrm{He}_4$ based on the LM2M2 potential evolved up to $\Lambda = 1.0\ (\mathrm{au})^{-1}$. The oscillator length b is fixed at $b = 4.8$ au, see Table 5.1, and the cutoff parameter is $N = 42$.

In Table 5.2, we present the results for the binding energies of N-body clusters up to $N = 10$ for different values of Λ. For comparison the MC results of Blume et al. [24] for the genuine LM2M2 potential are also shown. Similar to calculations of nuclear few-body systems with SRG evolved potentials [90], there is no monotonous dependence of the calculated energies on Λ. As Λ is decreased, the energies at first deviate further from the presumably accurate MC result before they approach this value again at the smallest Λ calculated.

	N Λ	0.25	0.5	0.75	1.0	MC [24]
E_3^B	58	125.941 ± 0.013	134.710 ± 0.079	131.75 ± 0.26	129.7 ± 1.0	125.5
E_4^B	42	$573.839 \pm 4.3 \cdot 10^{-5}$	620.50 ± 0.47	598 ± 3.2	579.4 ± 4	559.7
E_5^B	24	1389.100 ± 0.002	1502.27 ± 0.22	1433 ± 20	1470 ± 160	1309
E_6^B	18	2584.050 ± 0.008	2789.3 ± 3.0	2690 ± 200	2610 ± 490	2329
E_7^B	16	4164.876 ± 0.002	4484 ± 12	4410 ± 650	-	3565
E_8^B	16	6135.4 ± 0.1	6578 ± 16	-	-	5044
E_9^B	14	8499.63 ± 0.03	9101 ± 61	-	-	6683
E_{10}^B	14	11253.54 ± 0.07	-	-	-	8509

Table 5.2: Binding energies E_A^B in [mK] for various evolution parameters Λ from $\Lambda = 0.25$ (au)$^{-1}$ up to $\Lambda = 1.0$ (au)$^{-1}$. For $\Lambda = 5.0$ (au)$^{-1}$ no binding energies could be determined with acceptable uncertainties. The numbers are the extrapolated results with their uncertainties for the oscillator length b with highest binding energies. For comparison the results from the Monte Carlo calculations made by Blume et al. [24] are shown in the last column.

5.4 Effective Pisa Potential

Beyond the SRG-transformation, an effective potential can be constructed by simple parametrisations in the form of short-ranged interactions. At leading order in the large scattering length then both a two-body and a three-body contact interaction are required. In the practical application, we follow the procedure used by Gattobigio et al. and choose a Gaussian potential as the regularised form of a contact term [25]. The strength and range are chosen to reproduce the binding energy E_2, the scattering length a and effective range r_0 of the LM2M2 potential. The three-body interaction is taken as a Gaussian-hyper-central three-body term designed to reproduce the LM2M2 three-body ground state energy E_3. Specifically, this so-called effective Pisa potential then consists of the two-body interaction

$$V_{\mathrm{G}}(r_{ij}) = V_0 e^{-\frac{r_{ij}^2}{R^2}} , \tag{5.1}$$

in the coordinate $r_{ij} := (\vec{x}_2 - \vec{x}_1)$ with $V_0 = -1.227$ K and $R = 10.03$ au as well as the three-body interaction

$$W_{\mathrm{G}}(\rho_{ijk}) = W_0 e^{-2\frac{\rho_{ijk}^2}{\rho_0^2}} , \tag{5.2}$$

in the hyper-radius $\rho_{ijk} := \sqrt{2/3(r_{ij}^2 + r_{ik}^2 + r_{jk}^2)}$. The parameter pair (W_0, ρ_0) is not unique. There is an infinite number of possible combinations which reproduce the LM2M2 ground state energy for $^4\mathrm{He}_3$. In the following, we consider three combinations collected in Table 5.3. The three-body interaction with parameters $\rho_0 = 14$ au and $W_0 = 422$ mK is relatively soft and long-ranged such that we expect fast convergence with respect to the cutoff parameter N. In the following this is called the soft Pisa potential. The other two parameter combinations are referred to as hard Pisa potentials.

5.4.1 Soft Pisa Potential

We start with the 4-boson system. Fig. 5.4 shows in the left panel the ground state of $^4\mathrm{He}_4$ as a function of the oscillator length parameter b for the soft Pisa potential. One expects a plateau

	W_0 [mK]	ρ_0 [au]
soft	422	14
hard	$306.9 \cdot 10^3$	4
hard	$3 \cdot 10^8$	2.2511

Table 5.3: Considered combinations of W_0 and ρ_0, which reproduce ground state energy E_3 of the LM2M2 potential.

at the minimal energy, which becomes broader for larger model spaces. Indeed, we find such a plateau around $b = 8$ au with an energy $E_4 = -568.8$ mK. This coincides with the result $E_4 = -568.79$ mK found in [25]. In comparison to Monte Carlo calculations with the genuine LM2M2 potential, published by Blume et al. in [24], there is a deviation of 10 mK or 1.8 %.

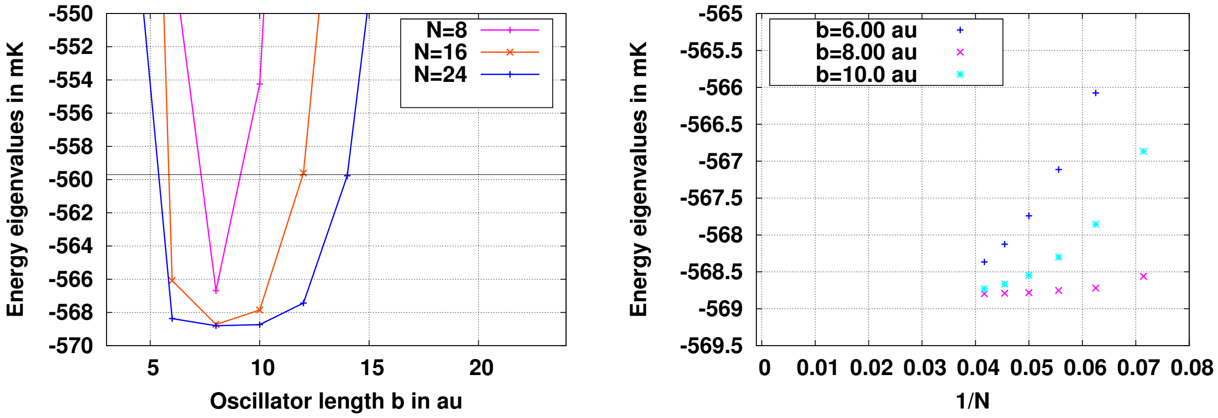

Figure 5.4: Ground state energy of ^{4}He$_4$ determined with Pisa Potential with $\rho_0 = 14$ au and $W_0 = 0.422$ K. **Left panel**: As a function of b for various cutoffs N. **Right panel**: As a function of N for various b. The Horizontal line is the result with genuine LM2M2 from Blume [24].

The determination of the estimated result for the full Hilbert space is again based on an extrapolation to $N \to \infty$. We apply the same procedure as for the SRG-evolved LM2M2 potential, i.e. the last two data points are extrapolated linearly to the infinite N limit. Our final value is the arithmetic average of the extrapolated values and the last data point, while their difference is taken as the uncertainty.

Using this extrapolation method, we have investigated A-particle systems of ^{4}He atoms up to $A = 12$. The results are collected in Table 5.4. Results from [25] and [24] are added for comparison. Only up to $A = 6$ results are published in [25]. For that region both results are approximately identical. Remarkable is the deviation from the Monte Carlo results: Until $A = 6$ the binding energies are larger for the effective Potential and differ from the MC results by less than 2 %. For $A > 6$ the binding energies are smaller and deviate approximately by 10 % for $A = 10$. The trend of this deviation can be explained by a combinatorial argument. The original LM2M2 is just a two-body interaction with a hard repulsive core. In contrast, the Pisa potential consists of an attractive two-body interaction and a repulsive three-body interaction. The number of pairs $N_P = 1/2A(A-1)$ and triplets $N_T = 1/6A(A-1)(A-2)$ depend on the particle number A differently. The number of pairs is larger or equal than the number of triplets until $A = 5$. For $A > 5$, the number of triplets and therefore the effect of the repulsive three-body interactions dominate the number of pairs and therefore the effects of the two-body interaction increasingly. This effect can be reduced by choosing a three-body interaction of shorter range ρ_0. The details of this interaction can then not be resolved by the more deeply bound systems with larger A. However, the price one has to pay is a slower convergence of the calculation. In the case of SRG-evolution the induced many-body forces thus become important at this point.

	Soft Pisa	Pisa [25]	LM2M2 with MC [24]	Pisa/MC
E_4^B	568.832 ± 0.036	568.79	559.7	$101.6\ \%$
E_5^B	1326.82 ± 0.18	1326.6	1309.3	$101.3\ \%$
E_6^B	2339.57 ± 0.72	2338.9	2329	$100.4\ \%$
E_7^B	3536.89 ± 0.76	-	3565	$99.2\ \%$
E_8^B	4858.4 ± 1.8	-	5044	$96.3\ \%$
E_9^B	6256.7 ± 3.8	-	6683	$93.7\ \%$
E_{10}^B	7699.3 ± 5.5	-	8509	$90.6\ \%$
E_{11}^B	9165.6 ± 3.5	-	-	-
E_{12}^B	10647 ± 5	-	-	-

Table 5.4: Binding energies determined with soft Pisa potential for system with $A = 4$ for up to $A = 12$ bosons. Energies are given in mK. **First column**: Soft Pisa potential with $\rho_0 = 14$ au and $W_0 = 0.422$ K. **Second column**: Results from [25]. **Third column**: Monte Carlo calculations for genuine LM2M2 potential done by Blume et al. [24]. **Fourth column**: Relative deviation of energies determined with Soft Pisa potential and Monte Carlo results of LM2M2.

In principle with the same approach systems with $A = 11$ and $A = 12$ can be examined. A cutoff of $N = 12$ here is still feasible. The best values of the oscillator length and the ground state energies can be estimated with the typical graphical analysis. Within error bars of 4 mK the binding energy of $^4\text{He}_{11}$ is found to be equal $E_{11} = (-9166 \pm 4)$ mK as extracted from the left panel in Figure 5.5 with extrapolation of N^{-1} to 0. From the right panel we likewise find $E_{12} = (-10647 \pm 5)$ mK.

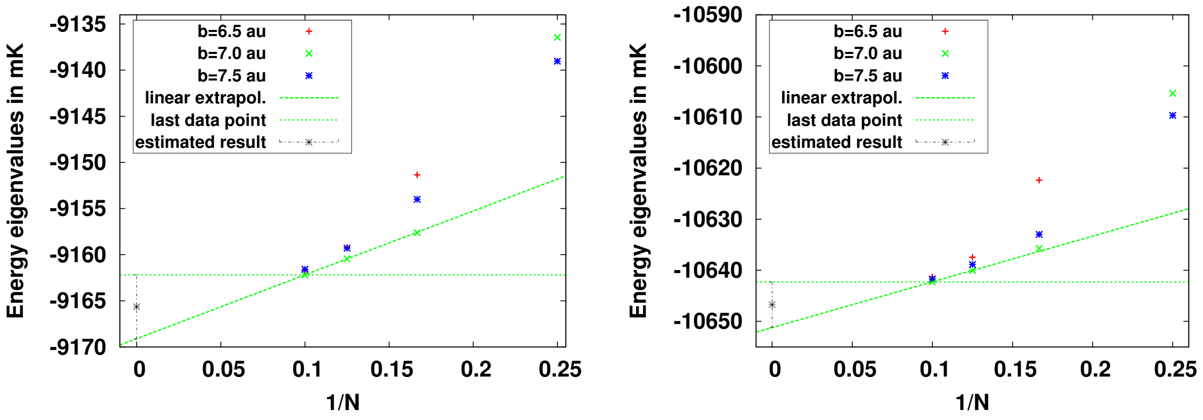

Figure 5.5: Ground state energy of $^4\text{He}_{11}$ and $^4\text{He}_{12}$ determined with the Pisa potential with $\rho_0 = 14$ au as a function of the cutoff parameter N. **Left panel**: $A = 11$. **Right panel**: $A = 12$.

We emphasise that these results are obtained with the effective Pisa potential and not with the genuine LM2M2 potential. As discussed above, this leads to a reduced binding compared to the genuine LM2M2 interaction. We expect from the results displayed in Table 5.4 that for $A = 11$ the deviation to MC results is of the order $15\ \%$ and for the $A = 12$ about $20\ \%$.

5.4.2 Hard Pisa Potentials

In this section the A-boson system is examined with the other parameter combinations for W_0 and ρ_0 listed in Table 5.3. Since these hard Pisa potentials are more similar to the original hard core LM2M2 potential, the deviation observed in the last section for the soft potential should be smaller at the expense of a slower convergence in N.

5.4.2.1 Unevolved Hard Pisa Potentials

To start with, the four boson system is studied with the unevolved hard Pisa potentials. In Figure 5.6 the results for the ground state energy of $^4\mathrm{He}_4$ are presented as a function of the oscillator length b for the hard Pisa potential with parameter $\rho_0 = 4$ au in the left panel and in the right panel with $\rho_0 = 2.2511$ au. Two features are clearly visible in this figure. At first, the position of the minimum depends on the interaction range. For $\rho_0 = 4$ au the minimum is around $b = 5.5$ au and for $\rho_0 = 2.2511$ au around $b = 4.5$ au. Secondly, the N dependence is the weaker for longer ranged interactions. As a consequence approximately converged results are not feasible for the hard Pisa potentials. Only with extrapolations correct results can be estimated, albeit with large uncertainties.

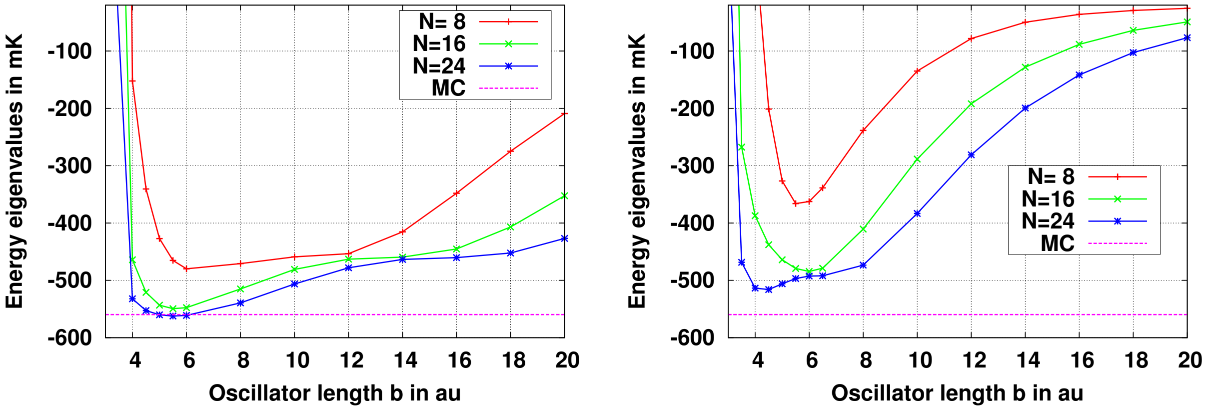

Figure 5.6: Ground state energy of $^4\mathrm{He}_4$ determined with the hard Pisa potential. **Left panel**: $\rho_0 = 4$ au. **Right panel**: $\rho_0 = 2.2511$ au.

As depicted in the left panel of Figure 5.7 the ground state energy eigenvalue for $\rho_0 = 4$ au is $E_4 = (-571.7 \pm 9.5)$ mK. Unfortunately, the model spaces are too small to investigate the discrepancy between the MC results with the genuine LM2M2 potential and results with soft Pisa interactions systematically by a study of the hard core versions. But, it is obvious that also for $\rho_0 = 4$ au the estimated binding energy is larger than the MC result and still compatible with the result with the soft Pisa potential.

In the right panel of Figure 5.7 the eigenenergies E_4 for $\rho_0 = 2.2511$ au are shown versus the inverse cutoff parameter $1/N$. We find an extrapolated energy eigenvalue $E_4 = (-586 \pm 69)$ mK. The uncertainties in the energy are larger than the difference between the soft Pisa result with $\rho_0 = 14$ au and the MC result.

But in spite of the large uncertainties, it is possible to make a statement about the errors caused by the discrepancy between the effective Pisa and the ab-initio LM2M2 potential in the many body sector. For instance, we consider the system with $A = 10$ bosons and the hard Pisa potential with parameter $\rho_0 = 4$ au. It is clear from Figure 5.8 that the estimated binding energy of $E_{10}^B =$

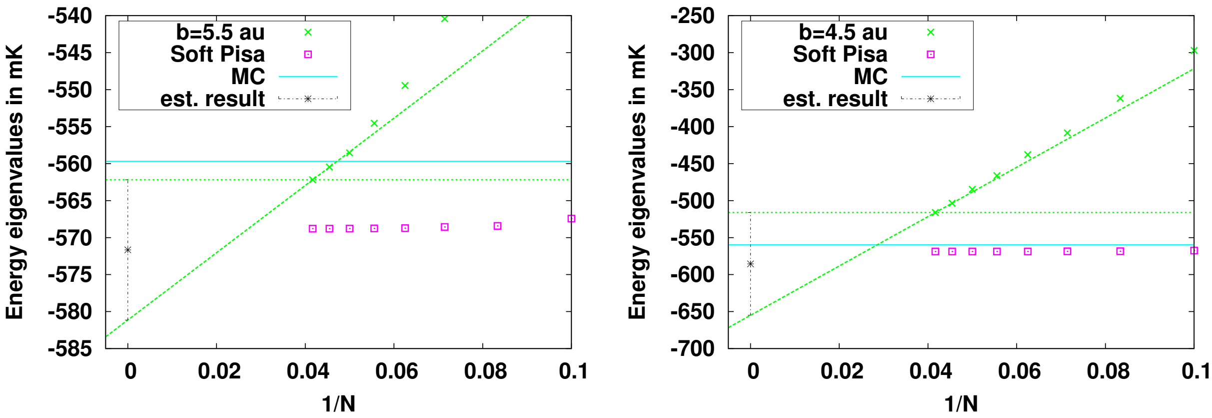

Figure 5.7: Ground state energy of ^{4}He$_4$ determined with the Pisa potential as a function of N. **Left panel**: $\rho_0 = 4$ au. **Right panel**: $\rho_0 = 2.2511$ au.

(7699.3 ± 5.5) mK for the soft Pisa potential and $E_{10}^B = (9335 \pm 1236)$ mK for the hard Pisa potential with $\rho_0 = 4$ are mutually exclusive. The hard Pisa potential indeed seems to produce binding energies more similar to the results with the LM2M2 potential obtained with Monte Carlo methods.

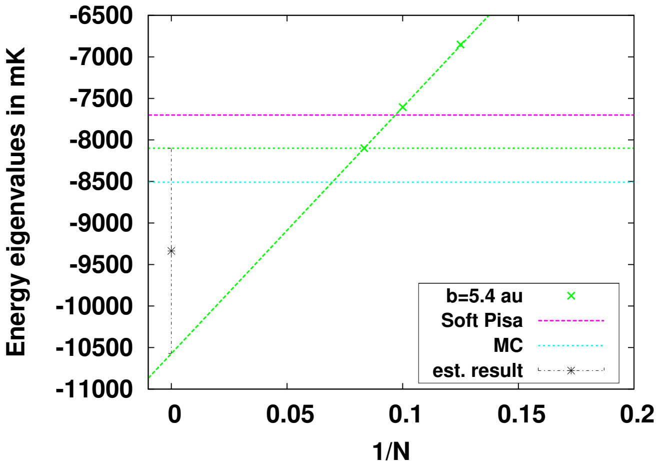

Figure 5.8: Ground state energy of ^{4}He$_{10}$ determined with the hard Pisa potential as a function of N with $\rho_0 = 4$ au.

Nevertheless, the slow convergence is a severe obstacle for the hard Pisa potential which becomes more and more severe for larger particle systems because of the necessity to use smaller and smaller model spaces. A possibility to guarantee a faster convergence is the SRG-evolution. As explained in section 2.4 here the hard Pisa potential is modified in order to separate high and low energy physics. In the next section results with the evolved potential are summarised.

5.4.2.2 SRG-Evolved Hard Pisa Potentials

In order to circumvent the problematic weak convergence in N for short interaction ranges, we apply the SRG-transformation to the hard Pisa Potentials with $\rho_0 = 4$ au or $\rho_0 = 2.2511$ au.

Note however, that there are two simplifications assumed here. Firstly, we neglect all induced forces apart from two- and three-body forces. They are supposed to be suppressed. Secondly, the three-body evolved forces are difficult to determine for higher angular momenta. Thus, we are forced to restrict the potential matrix elements which are used and by hand have to set the other elements to zero, specifically this means that only matrix elements are considered where the 3-body subsystems have total angular momenta $L_{12} \leq 4$ and that for the two Jacobi angular momenta $l_1 \leq 4$ and $l_2 \leq 4$ hold.

Before we will show results for the SRG-evolved Pisa potential, it is worthwhile to discuss the effect of this restriction in angular momenta. For this purpose, some genuine Pisa potentials results are compared.

Figure 5.9 shows the absolute values of the relative deviation $|\widetilde{E^B}_4 - E_4^B|/E_4^B$ of binding energies $\widetilde{E^B}_4$ and E_4^B. Here, $\widetilde{E^B}_4$ denotes the result with restrictions in angular momenta mentioned above and E_4^B the result without those. The left panel shows the deviations for the soft Pisa potential and the right one those for hard Pisa potential with $\rho_0 = 4$ au. Remarkably, the deviations are very small in comparison to uncertainties caused by the use of effective potentials and the involved extrapolations. For the hard as well as for the soft Pisa potential the relative deviations are smaller than one percent for all oscillator lengths in the range from $b = 2$ au to $b = 20$ au. The same behaviour is found for $A = 5$. The restriction $L_{12} \leq 4$, $l_1 \leq 4$ and $l_2 \leq 4$ for the 3-body interaction is thus empirically justified in order to simplify the SRG-evolution.

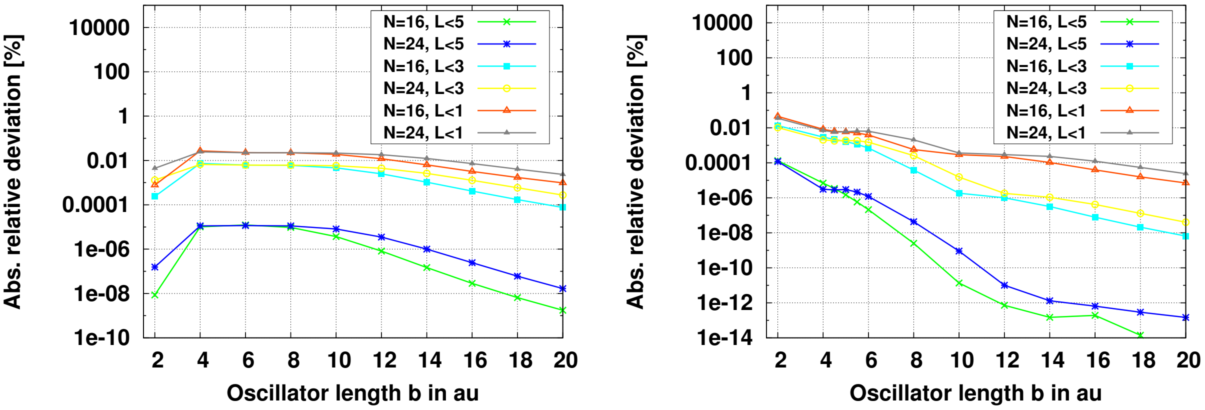

Figure 5.9: Relative deviation of binding energies calculated with and without restrictions in angular momenta for the 3-body interaction $L_{12} \leq c$, $l_1 \leq c$ and $l_2 \leq c$, see text. As a function of b for two different model spaces $N = 16$ or $N = 24$ three restrictions are shown with $c = 0,\ 2,\ 4$. **Left panel**: Soft Pisa potential. **Right panel**: Hard Pisa potential with $\rho_0 = 4$ au.

Returning to the SRG-transformed Pisa potential the binding energies for several boson systems are determined. As for the unevolved Pisa potential the four boson system is studied. As shown in the left panel of Figure 5.10 the binding energy E_4^B for the SRG-evolved hard Pisa potential with the flow parameter $\Lambda = 0.25\ (\text{au})^{-1}$ and width $\rho = 4$ au is $E_4^B = (560.96 \pm 0.05)$ mK. It is smaller than for the unevolved hard Pisa potential which led to the result $E_4^B = (571.7 \pm 9.5)$ mK.

In the right panel of Figure 5.10 the binding energies E_5^B are shown versus $1/N$ for $\rho = 4$ au and the SRG flow parameter $\Lambda = 0.25\ (\text{au})^{-1}$. In comparison to the unevolved hard Pisa potential with $\rho_0 = 4$ au, to the Monte Carlo calculations and to the soft Pisa potential with binding energies $E_5^B = (1341 \pm 59)$ mK, $E_5^B = 1309.3$ mK and $E_5^B = (1326.82 \pm 0.18)$ mK, respectively, the calculation with the evolved hard Pisa potential yield a smaller binding energy of $E_5^B = (1277.86 \pm 0.25)$ mK.

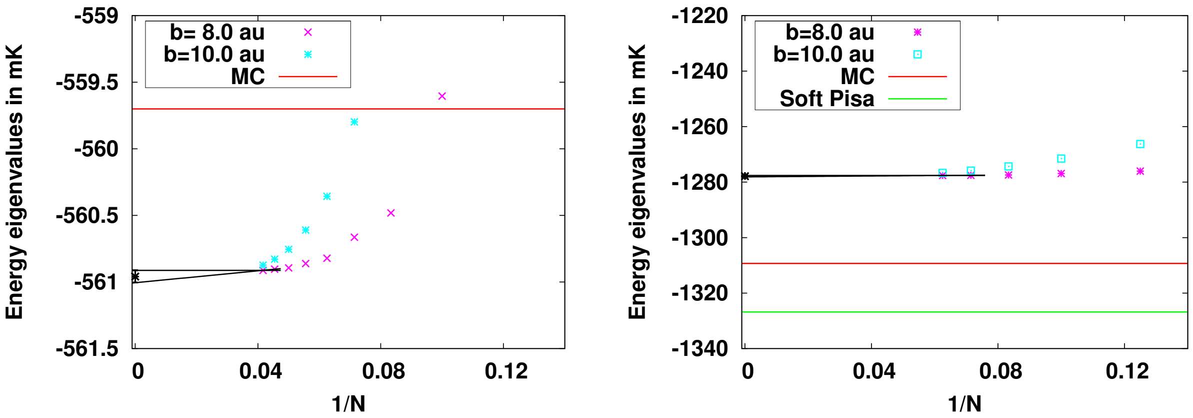

Figure 5.10: Energy eigenvalues for SRG-evolved hard Pisa potential with width $\rho_0 = 4$ au and flow parameter $\Lambda = 0.25\ (\mathrm{au})^{-1}$ versus $1/N$. The angular momenta are restricted with $L_{12} \leq 4$, $l_1 \leq 4$ and $l_2 \leq 4$. **Left panel**: $A = 4$. **Right panel**: $A = 5$

5.5 Conclusion

In this chapter we have studied ^{4}He-atom clusters with up to $A = 12$ constituents using the shell-model approach. Starting with the two-body ab-initio potential LM2M2 we found for binding energies E_A^B a very slow convergence in the cutoff parameter N. Therefore, the LM2M2 potential was unitarily transformed with the SRG evolution. Omitting the induced many-particle potentials binding energies for various flow parameter Λ was determined. The extracted binding energies strongly depend on the flow parameter and deviate from predictions based on Monte Carlo calculations with the unevolved LM2M2 potential. As in nuclear few-body systems with SRG-evolved potentials, we found no monotonous dependence on Λ. Hence, a prediction of binding energies is subject to large uncertainties.

Instead of using an effective potential constructed systematically with the SRG transformation, we also determined binding energies with the so-called Pisa potential which is an effective parametric potential constructed to reproduce the two- and three-body ground state binding energies consisting of a two- and a three-body Gaussian potential. We studied two different versions with a soft long-ranged or a hard short-ranged three-body potential. We calculated binding energies in finite model spaces for up to twelve atoms for the soft Pisa potential. The true binding energies could be estimated with small uncertainties with linear extrapolations. For up to ten ^{4}He atoms these results deviate less than $\Delta E/E = 10\ \%$ from results obtained by Monte-Carlo methods.

Finally, binding energies based on the hard Pisa potential were determined. Because of the strong short-range three-body force we found a slower convergence in the cutoff parameter N. Accordingly, the SRG transformation was also applied to the hard Pisa potential with three-body potentials. Due to the time-consuming SRG-evolution of three-body potentials a truncation in relative angular momenta was necessary. For this evolved potential binding energies with very small uncertainties were estimated by linear extrapolations.

Chapter 6

Miscellanea

In this chapter two miscellaneous topics are covered. At first, I outline the idea to determine the atom-dimer and dimer-dimer scattering length and effective range from the energy spectrum of fermions in a harmonic confinement. Secondly, a promising study to extract information about scattering resonances within the shell-model approach is presented.

6.1 Scattering Observables from Energy Spectra

The idea to determine elastic scattering quantities from the energy spectrum in a finite volume was firstly proposed by Lüscher [91, 92]. In lattice QCD the energy spectrum is generally calculated on a cubic lattice with the extent L with periodic boundary condition. If the range of interaction R is much smaller than the size of the box L, the scattering phase shift can be determined from the energy spectrum of discrete states. A recent review is given in [93]. For the energy splitting ΔE_n of the two-hadron states and the hadron masses m one finds the following so-called Lüscher relation:

$$p_n \cot\left(\delta(p_n)\right) = \frac{1}{\pi L} S\left[\left(\frac{p_n L}{2\pi}\right)^2\right] , \qquad S(x) := \sum_{\vec{j}}^{|\vec{j}|<\Lambda} \frac{1}{|\vec{j}|^2 - x} - 4\pi\Lambda , \tag{6.1}$$

where the splitting is given by $\Delta E_n = 2\sqrt{p_n^2 + m^2} - 2m$ and the limit $\Lambda \to \infty$ is understood. As a consequence, with the energy spectrum in the finite volume the energy-dependent phase shift $\delta(p_n)$ can be determined.

In 2010, Lüscher's idea was adapted to trapped particles in a harmonic potential by Stetcu et al. [77]. Moreover, Luu et al. used this approach for nucleon-nucleon scattering in a harmonic potential [94].

Following Jonsell's procedure to derive the energy spectrum of two trapped bosons with contact interactions [95], Stetcu et al. generalised the Busch formula derived for contact interactions to interactions with finite ranges

$$2\frac{\Gamma\left(-\frac{E}{2\hbar\omega} + \frac{3}{4}\right)}{\Gamma\left(-\frac{E}{2\hbar\omega} + \frac{1}{4}\right)} = \frac{b}{a}\left(1 - \frac{r_0 a}{b^2}\frac{E}{\hbar\omega} + \mathcal{O}\left(\left(\frac{E}{\hbar\omega}\right)^2\right)\right) , \tag{6.2}$$

with the oscillator length $b = \sqrt{\hbar/(\mu\omega)}$, the scattering length a and the effective range r_0. Similarly, Suzuki et al. considered the two-atom energy spectrum near Feshbach resonances at higher partial waves in 2009 [96].

Note that the oscillator length is defined with the reduced mass in this section, which belongs to the usage of standard relative coordinates. In former sections I used Jacobi coordinates and the oscillator length was defined by $b = \sqrt{\hbar/(m\omega)} = \sqrt{\hbar/(2\mu\omega)}$. In the next paragraph, I outline the derivation of equation (6.2).

Derivation of Equation (6.2)**:** Consider the situation where the oscillator length is much larger than the range of the interaction $b \gg R$. Additionally, consider only states with small energies E, i.e. $\sqrt{E/(\hbar\omega)}R/b \ll 1$. Now one observes that usually the effective range r_0 is of the same order of magnitude as R. In this situation the main point is that for distances $r \ll b$ the influence of the harmonic oscillator potential compared that of the short-ranged potential on the wave function can be neglected. Therefore, it is sensible to compare at distances $R < r \ll b$ the free wave function scattered on the potential without any confinement $\psi_{\text{sca}}(r)$ with the solution $\psi_{\text{osc}}(r)$ of the harmonic oscillator outside the range of the short range interaction.

For the sake of readability, I define the dimensionless variables $\xi := E/(\hbar\omega)$ and $\rho := r/b$. With the relation $\sqrt{2\xi} = bp$ between the energy and the momentum p the scattering wave function with energy ξ for $\rho > R/b$ and vanishing relative angular momenta reads

$$\psi_{\text{sca}}(\rho) = \frac{c_2}{\rho}\left[\sin\!\left(\sqrt{2\xi}\,\rho\right) + \tan\left(\delta_0\!\left(\sqrt{2\xi}\right)\right)\cos\!\left(\sqrt{2\xi}\,\rho\right)\right] . \tag{6.3}$$

For $\sqrt{2\xi}\rho \ll 1$ the trigonometric functions in the wave function $\psi_{\text{sca}}(\rho)$ can be expanded and this yields

$$\psi_{\text{sca}}(\rho) = c_2 \tan\left(\delta_0\!\left(\sqrt{2\xi}\right)\right)\frac{1}{\rho}\left(1 + \rho\sqrt{2\xi}\cot\left(\delta_0\!\left(\sqrt{2\xi}\right)\right) + \mathcal{O}\left(\left(\sqrt{2\xi}\rho\right)^2\right)\right) . \tag{6.4}$$

The solution with energy ξ and vanishing angular momentum of the Schrödinger equation with spherical oscillator potential with frequency ω is given in terms of the confluent hypergeometric function M [97] as

$$\psi_{\text{osc}}(\rho) = ce^{-|\rho|^2/2}\frac{1}{\rho}\left[M\left(\frac{1}{4} - \frac{\xi}{2}, \frac{1}{2}, |\rho|^2\right) - 2\rho\frac{\Gamma\left(\frac{3}{4} - \frac{\xi}{2}\right)}{\Gamma\left(\frac{1}{4} - \frac{\xi}{2}\right)}M\left(\frac{3}{4} - \frac{\xi}{2}, \frac{3}{2}, |\rho|^2\right)\right] . \tag{6.5}$$

For small $\rho \ll 1$ this function can be expanded and one finds

$$\psi_{\text{osc}}(\rho) = c\frac{1}{\rho}\left[1 - 2\rho\frac{\Gamma\left(3/4 - \xi/2\right)}{\Gamma\left(1/4 - \xi/2\right)} + \mathcal{O}\left(|\rho|^2\right)\right] . \tag{6.6}$$

Within the effective range expansion (ERE) the cotangent of the scattering phase reads

$$\cot\left(\delta_0\!\left(\sqrt{2\xi}\right)\right) = -\frac{1}{\sqrt{2\xi}}\frac{b}{a}\left(1 - \frac{r_0 a}{b^2}\xi\right) + \dots . \tag{6.7}$$

As long $\sqrt{2\xi}R \ll 1$, higher terms are suppressed. By comparison of $\psi_{\text{sca}}(\rho)$ and $\psi_{\text{osc}}(\rho)$ in equations (6.6) and (6.4) and with the ERE one finds the sought relation (6.2).

6.1.1 Atom-Dimer Scattering

Rotureau et al. suggested to apply formula (6.2) for the three-body sector in order to determine the atom-dimer scattering length a_{AD} and effective range r_{AD} [98]. For this purpose, they considered fermionic atoms having two spin states, i.e. the total spin of the system is $S = 1/2$, $M_s = \pm 1/2$. Hence, no three-body short-ranged interactions contribute.

To apply formula (6.2) to this case the oscillator length must be modified to $b_{AD} = \sqrt{\hbar/(\mu_{AD}\omega)}$ with the atom-dimer reduced mass $\mu_{AD} = 2m/3$. Secondly, the energy E should be inserted as follows: Since the threshold for the three-body system is now the ground state energy of the two-body system $E_{2,0}$, the relevant energy is then

$$\Delta E_{3,n} := E_{3,n} - E_{2,0} \; . \tag{6.8}$$

and one finds

$$2\frac{\Gamma\left(-\frac{\Delta E_{3,n}}{2\hbar\omega}+\frac{3}{4}\right)}{\Gamma\left(-\frac{\Delta E_{3,n}}{2\hbar\omega}+\frac{1}{4}\right)} \approx \frac{b_{AD}}{a_{AD}} - \frac{r_{AD}}{b_{AD}}\frac{\Delta E_{3,n}}{\hbar\omega} \; . \tag{6.9}$$

The energy $E_{2,0}$ coincides with the renormalisation energy $E^{(2)}$ in the shell-model approach.

The scattering length a_{AD} and the effective range r_{AD} can be determined with two three-body energies $E_{3,1}$ and $E_{3,2}$. Using the definition $f(x) := 2\Gamma\left(-\frac{x}{2\hbar\omega}+\frac{3}{4}\right)/\Gamma\left(-\frac{x}{2\hbar\omega}+\frac{1}{4}\right)$ one finds

$$\frac{b_{AD}}{a_{AD}} = \frac{\Delta E_{3;2} f(\Delta E_{3;1}) - \Delta E_{3;1} f(\Delta E_{3;2})}{\Delta E_{3;2} - \Delta E_{3;1}} \; , \tag{6.10}$$

$$\frac{r_{AD}}{b_{AD}} = \frac{f(\Delta E_{3;1}) - f(\Delta E_{3;2})}{\Delta E_{3;2} - \Delta E_{3;1}}\hbar\omega \; . \tag{6.11}$$

The next step is to test this approach for applicability and stability. Rotureau et al. in [98] argued that equation (6.9) is only valid if the atom-dimer relative momenta $\sqrt{\Delta E_{3;n}/(\hbar\omega)}$ are smaller than b/a. Hence, large scattering lengths are preferable. However, the size of the dimer is proportional to a and the dimer can only form inside the trap if a is small compared to the typical size of the trap b. Consequently, a/b must not be too large.

6.1.1.1 Atom-Dimer Scattering Length

In this section, the atom-dimer scattering lengths a_{AD} are determined with equation (6.10) for various two-body scattering lengths a. In order to test the approach, these values are compared with the reference value of the relation between the atom-dimer scattering length a_{AD} and the two-body scattering length a

$$\frac{a_{AD}}{a} = 1.18 \; , \tag{6.12}$$

predicted in numerous calculations summarised in [99].The shell-model approach is used to determine the required three-body energy spectrum. The spectrum is calculated for several values of the two-body scattering length a. Table 6.1 contains the renormalisation energies and the corresponding scattering lengths a considered.

$E^{(2)} = E_{2,0}$	0.49	0.0	-1	-2.5	-5	-10	-20	-50
a	56.8	1.48	0.68	0.44	0.32	0.22	0.16	0.10

Table 6.1: Renormalisation energies $E^{(2)}$ and scattering length a which are considered to test the expected relation $a_{AD}/a = 1.18$. The energies are given in units of $\hbar\omega$ and a in units of the oscillator length b.

In Figure 6.1 the ground and the first excited state with $L^P = 0^+$ are depicted for the three-body fermionic system with total spin $S = 1/2$ for various renormalisation energies $E^{(2)}$. The energy levels are shown as a function of the cutoff parameter $1/\sqrt{N + (3-1)3/2}$. The model space results are extrapolated to $N \to \infty$ with quadratic polynomials. The eigenvalues for large renormalisation energies $|E^{(2)}|$ have a larger curvature and a stronger dependence on the parameter N in comparison to the results for smaller $|E^{(2)}|$. Consequently, the extrapolated spectra for these large energies $|E^{(2)}|$ are less precisely determined. We shall see that this impedes an accurate determination of the relation a_{AD}/a.

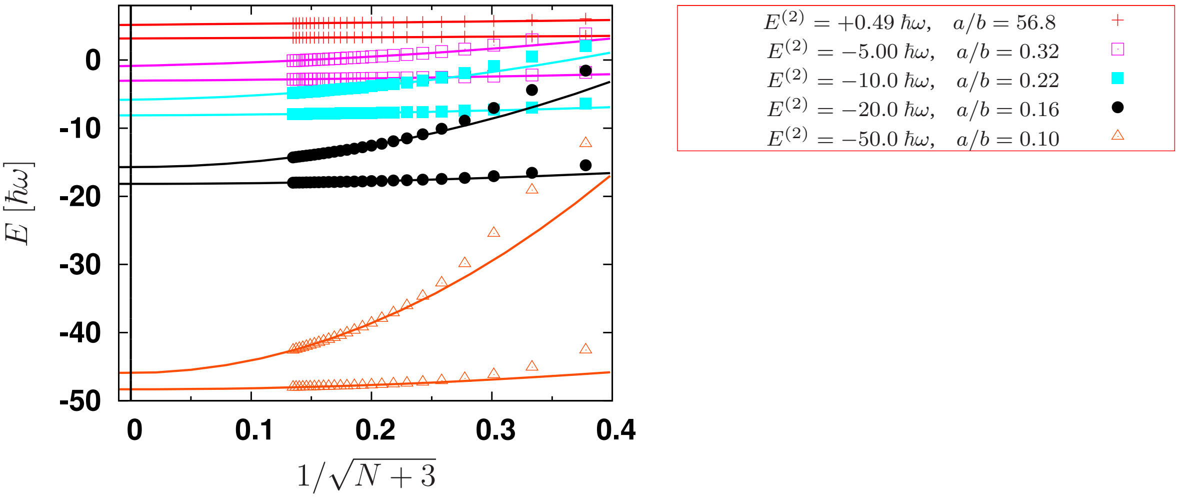

Figure 6.1: Ground and first excited states with $L^P = 0^+$ for the three-body fermionic system with $S = 1/2$. The energy levels are shown as a function of the cutoff N for several renormalisation energies $E^{(2)}$. The energies are extrapolated to $N \to \infty$ with quadratic polynomials.

In order to determine the atom-dimer scattering length a_{AD} for the various renormalisation energies $E^{(2)}$, the extrapolation functions for the energy levels of the ground state $E_{3;0}(N)$ and the first excited state $E_{3;1}(N)$ are used to determine $\Delta E_{3;0}(N)$ and $\Delta E_{3;1}(N)$. These two variables are inserted in equation (6.10) with the result $a_{AD}(N)$, i.e. a model space dependent atom-dimer scattering length.

The quantity $a_{AD}(N)/a$ is shown in Figure 6.2 as a function of N for various renormalisation energies $E^{(2)}$. The reference value $a_{AD}/a = 1.18$ is also displayed as a straight horizontal line. Note that the other lines are no direct extrapolations of $a_{AD}(N)$, but indicate the atom-dimer scattering length $a_{AD}(N)$ determined with the extrapolated energy values, see also Figure 6.1. One observes that there is a large discrepancy for the scattering length $a/b = 1.48$ (corresponding to $E^{(2)} = 0\ \hbar\omega$) between the reference value $a_{AD}/a = 1.18$ and the extrapolated value $\lim_{N\to\infty} a_{AD}(N)/a = 2.33$. This deviation could be interpreted as a consequence of the fact that the dimer could not form inside the trap due to its size of the order of magnitude of $a > b$. Moreover, the discrepancies become

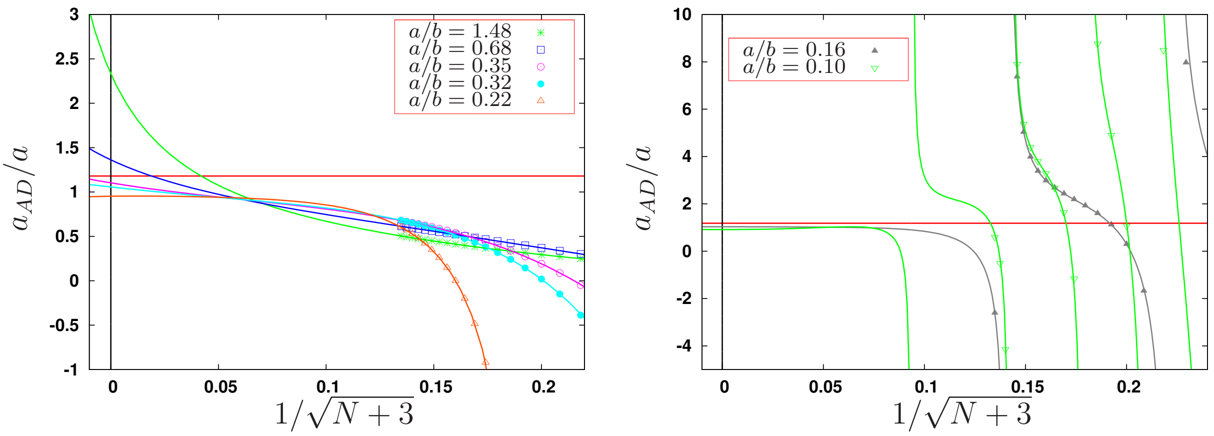

Figure 6.2: a_{AD} for various renormalisation energies $E^{(2)}$ (or scattering lengths a). The solid horizontal straight line indicate the reference value 1.18. The points are the energy spectra for specific cutoff parameter N and the lines correspond to the extrapolation polynomials. Both inserted in equation (6.10). **Left panel**: results for scattering length up to $a/b = 0.22$. **Right panel**: results for $a/b = 0.16$ and $a/b = 0.10$.

larger for very small scattering lengths, for example for the curve for $a/b = 0.22$ (corresponding to $E^{(2)} = -10\ \hbar\omega$), where $\lim_{N\to\infty} a_{AD}(N)/a < 1$.

The situation is even more complicated for smaller scattering lengths. In the right panel of Figure 6.2 the atom-dimer scattering length a_{AD} is depicted for the renormalisation energies $E^{(2)} = -20\ \hbar\omega$ and $E^{(2)} = -50\ \hbar\omega$. With the extrapolation in the energy eigenvalues the atom-dimer scattering for $N \to \infty$ is estimated. For these two renormalisation energies one finds approximately $a_{AD}(\infty)/a \approx 1.03$ and $a_{AD}(\infty) \approx 0.92$, respectively. In spite of the poles in equation (6.10) determining the atom-dimer scattering length, the values for $N \to \infty$ lie in the vicinity of the correct value at 1.18. Nevertheless, it seems delicate to assess the applicability of this equation also in this case.

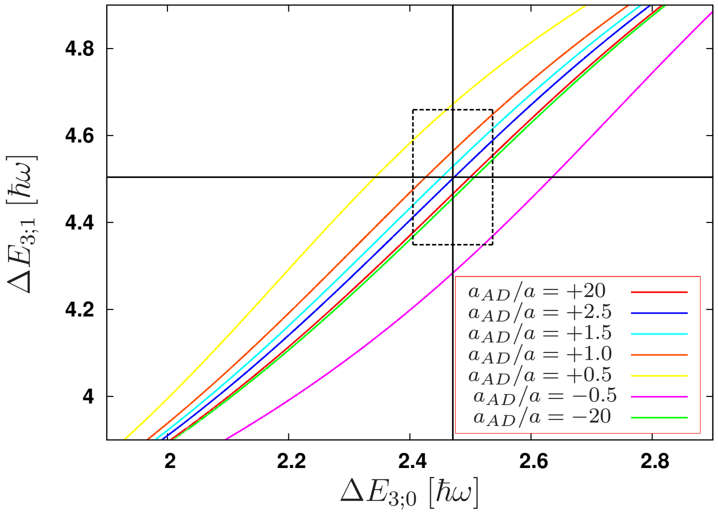

Figure 6.3: Contour plot of the ratio a_{AD}/a as a function of $\Delta E_{3;0}$ and $\Delta E_{3;1}$. $E^{(2)} = 0\ \hbar\omega$. The solid straight lines indicate the energies $\Delta E_{3;0}$ and $\Delta E_{3;1}$ extrapolated to $N \to \infty$. The rectangle enclosed by the dashed lines indicates the uncertainty region. One expects that this region contains the correct value.

Especially, one should notice, that the extrapolation of the energy eigenvalues itself contains uncertainties. In order to investigate the influence of these uncertainties on the estimated atom-dimer scattering length a_{AD} for various energies $E^{(2)}$, I show contour plots of the ratio a_{AD}/a as a function of $\Delta E_{3,0}$ and $\Delta E_{3,1}$ for various energies $E^{(2)}$. To start with, Figure 6.3 shows the contour plot for $E^{(2)} = 0\ \hbar\omega$ ($a/b = 1.48$). The solid horizontal or vertical straight lines represent the energies $\Delta E_{3;0}$ and $\Delta E_{3;1}$ extrapolated to $N \to \infty$, respectively. These extrapolated values carry uncertainties which are conservatively estimated as half of the distance between the extrapolated energy values and the corresponding eigenvalues determined with the largest cutoff parameter N. The uncertainty estimate is indicated in the following figures by a dashed rectangle. One thus expects, that the rectangle enclosed by the dashed lines represents the region which contains the correct value. Explicitly, in Figure 6.3 it is obvious that a prediction of the ratio a_{AD}/a is highly problematic. The intersection of the two black solid lines marks the position with the value $a_{AD}/a \approx 2.33$. However, in the vicinity of this point inside the uncertainty rectangle, there is a pole between the contour line $a_{AD}/a = 20$ and $a_{AD}/a = -20$. Hence, the predicted value has infinity large errors and it is impossible to conclude on the basis of my or of Rotureau's [98] results that equation (6.10) is not applicable for the scattering length $a/b = 1.48$.

In the next Figure 6.4 the contour plots for the renormalisation energies $E^{(2)} = -4\ \hbar\omega$ and $E^{(2)} = -10\ \hbar\omega$ are depicted. The intersection points again indicate the extrapolated energy values with the result $a_{AD}/a = 1.10$ and $a_{AD}/a = 0.95$. The main difference to the former plot for energy $E^{(2)} = 0\ \hbar\omega$ is that the rise in the vicinity of the pole is slower. As a consequence, the distances between the contour lines are more pronounced, particularly in the vicinity of the intersection point. Thus, the uncertainties in the results of the atom-dimer scattering length are smaller. However, the problem with the pole persists in a moderated form: Here, the pole is at the edge of the uncertainty rectangle estimated conservatively and not in the middle anymore.

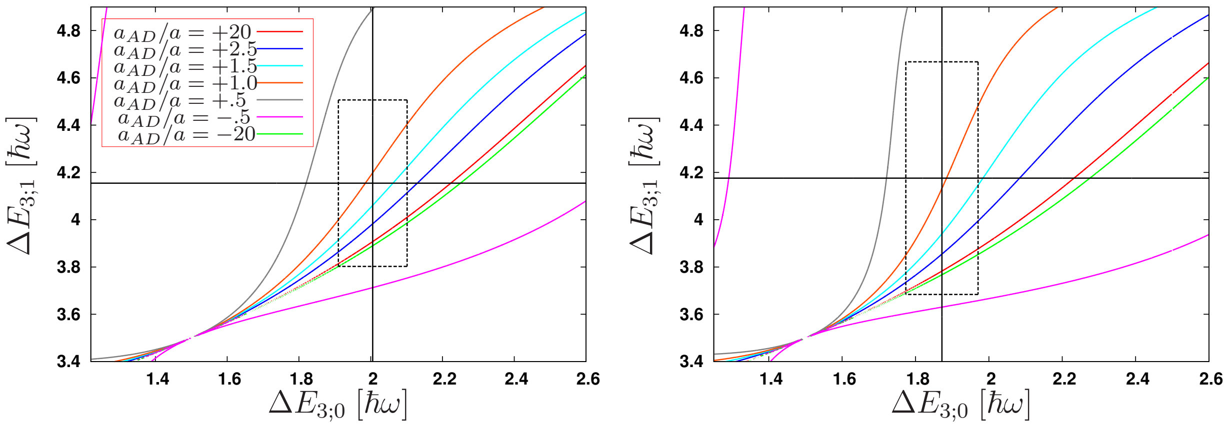

Figure 6.4: Contour plot of the ratio a_{AD}/a as a function of $\Delta E_{3;0}$ and $\Delta E_{3;1}$. The solid lines indicate the energies $\Delta E_{3;0}$ and $\Delta E_{3;1}$ extrapolated to $N \to \infty$. The rectangle enclosed by the dashed lines indicates the uncertainty region. One anticipates that this region contains the correct value. **Left panel**: $E^{(2)} = -4\ \hbar\omega$. **Right panel**: $E^{(2)} = -10\ \hbar\omega$.

Finally, the contour plot for the extremely negative renormalisation energy $E^{(2)} = -50\ \hbar\omega$ is shown in Figure 6.5. In this case, the contour lines are clearly separated which in principle is a favourable situation to determine the atom-dimer scattering length. But here the obstacle is the uncertainties in the extrapolated eigenvalues, in particular for the first excited state with value $\Delta E_{3;1} = (4.1 \pm 1.7)\ \hbar\omega$. As shown in the spectrum in Figure 6.2 the first excited state for $E^{(2)} = -50\ \hbar\omega$ has a large curvature and a strong dependence on N leading to a large uncertainty. This uncertainty prohibits an accurate determination of the atom-dimer scattering length a_{AD}.

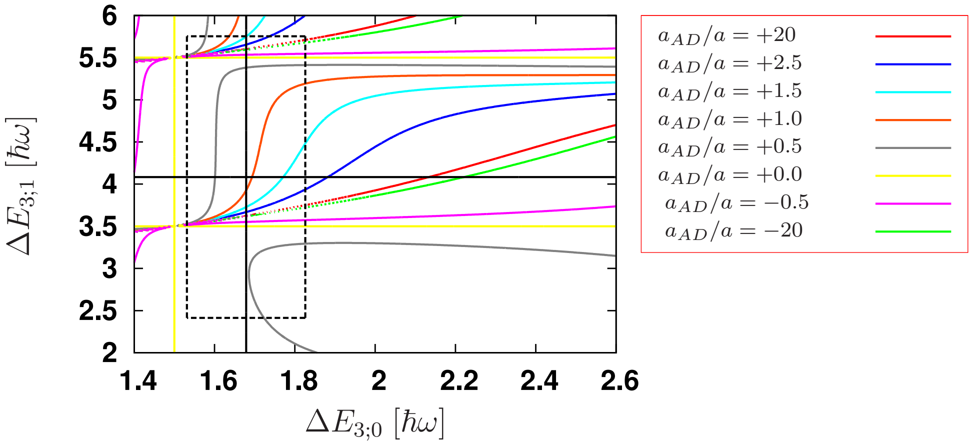

Figure 6.5: Contour plot of the ratio a_{AD}/a as a function of $\Delta E_{3;0}$ and $\Delta E_{3;1}$. $E^{(2)} = -50\ \hbar\omega$. The solid lines indicate the energies $\Delta E_{3;0}$ and $\Delta E_{3;1}$ extrapolated to $N \to \infty$. The rectangle enclosed by the dashed lines indicates the uncertainty region. One anticipates that this region contains the correct value.

6.1.1.2 Atom-Dimer Effective Range

This section considers the determination of the atom-dimer effective range r_{AD}. With Eqn. (6.11) also the effective range can be determined from the energy spectrum given in Figure 6.1. Two inconsistent predictions for the atom-dimer effective range r_{AD} were published by Grinyuk et al. [100] and by Stecher et al. [101]. Recently, the result of Grinyuk et al. has been confirmed by Bour et al. [99] who found that the ratio of the atom-dimer effective range r_{AD} and the scattering length a is given approximately by

$$\frac{r_{AD}}{a} \approx -0.0383\ . \tag{6.13}$$

Firstly, the N-dependent atom-dimer effective range $r_{AD}(N)$ is calculated for the typical scattering lengths a from the model-space spectra and their extrapolations. The results are shown in Figure 6.6. For all scattering lengths up to $a/b = 0.32$ the results are in the vicinity of the reference value. For smaller scattering lengths the discrepancies become large, particularly for the very small scattering length $a/b = 0.10$. In the next step, the influence of uncertainties in the extrapolation is studied. For this purpose, contour plots for r_{AD}/a are shown in the following figures as a function of the energies $\Delta E_{3;0}$ and $\Delta E_{3;1}$.

In the first contour plots in Figure 6.7 the results for the renormalisation energies $E^{(0)} = 0\ \hbar\omega$ $(a/b = 1.48)$ and $E^{(0)} = -4\ \hbar\omega$ $(a/b = 0.68)$ are shown. Note that the colours of the contour lines on the left and right side correspond to different levels. For large scattering lengths the function is very flat. Therefore, r_{AD}/a can be determined for $a/b = 1.48$ rather precisely. From the left panel one extracts a value of $r_{AD}/a = +0.035 \pm 0.28$ which is still compatible with the reference value of $r_{AD}/a = -0.0383$. From the right panel a value of $r_{AD}/a = 0.29^{+2.5}_{-5}$ can be extracted. Also this value is still compatible with the reference value, but it has much larger uncertainties.

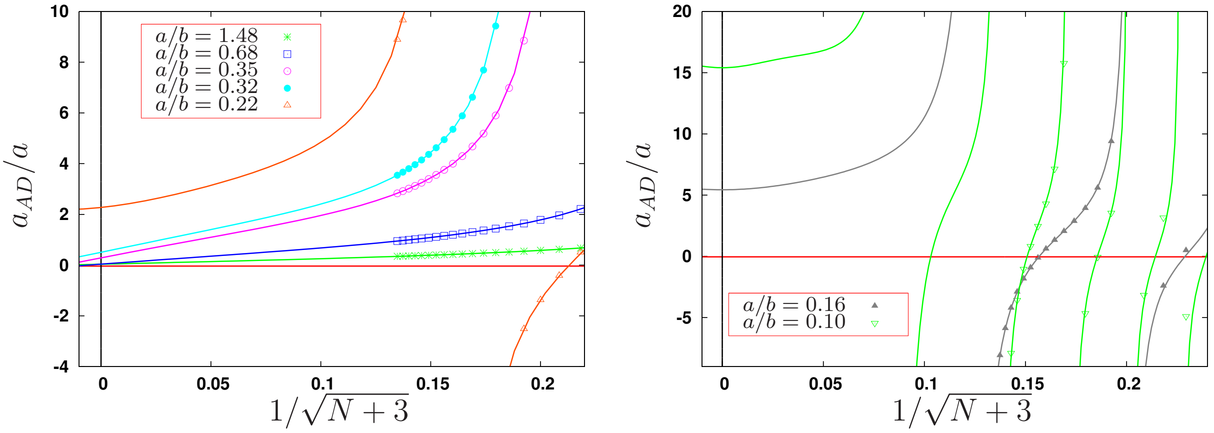

Figure 6.6: r_{AD} for various renormalisation energies $E^{(2)}$. The solid horizontal straight line represents the reference value $r_{AD}/a = -0.0383$. The points are the values for specific cutoff parameters N and the curves correspond to the extrapolation polynomials, both inserting in equation (6.10). **Left panel**: results for scattering length up to $a/b = 0.22$. **Right panel**: results for $a/b = 0.16$ and $a/b = 0.10$.

Finally, I consider the contour plots for renormalisation energies $E^{(2)} = -10\ \hbar\omega$ $(a/b = 0.22)$ and $E^{(2)} = -50\ \hbar\omega$ $(a/b = 0.10)$ in Figure 6.8. Obviously, the atom-dimer effective range cannot be determined with the intersection point due to two problems: Firstly, the extrapolations contain larger uncertainties and secondly, the contour lines lie closer together, i.e. the function is steeper.

6.1.1.3 Conclusion

In the last two sections I have investigated the applicability of equations (6.10) and (6.11) in order to determine the atom-dimer scattering length and effective range. In conclusion, it can be stated that values for a_{AD} and r_{AD} with acceptable error bands can be extracted only for a small range of two-body scattering lengths $0.32 < a/b < 0.68$. For other values the uncertainties are too large to make a statement. For $a/b > 1$ one expects that the dimer cannot form in the trap. However, the validity of the approach can neither be verified nor be excluded for these large scattering lengths due to uncertainties. The combination of poles in the functions and uncertainties in the extrapolations impede a conclusive statement concerning a possible inconsistency with the reference values. For very small scattering lengths the main problem for the determination of a_{AD} is the uncertainty in the extrapolations. In principle, the function (6.10) is rather flat in the region of small a/b which would guarantee a moderate propagation of uncertainties. In contrast, the dimer-atom effective range r_{AD} was found to show an opposite behaviour.

6.1.2 Dimer-Dimer Scattering

In this section, the former approach for dimer-atom scattering is adapted to the dimer-dimer scattering. The 4-body sector with two pairs of identical fermions is the appropriate system to investigate this scattering. There is no three-body interaction and no bound trimer. Therefore, it is not necessary to distinguish between dimer-dimer and trimer-atom scattering. In principle the dimer-dimer scattering length a_{DD} and effective range r_{DD} should be analogous to the equations (6.10) and (6.11). Only two things have to be changed. The threshold for the tetramer is the double dimer

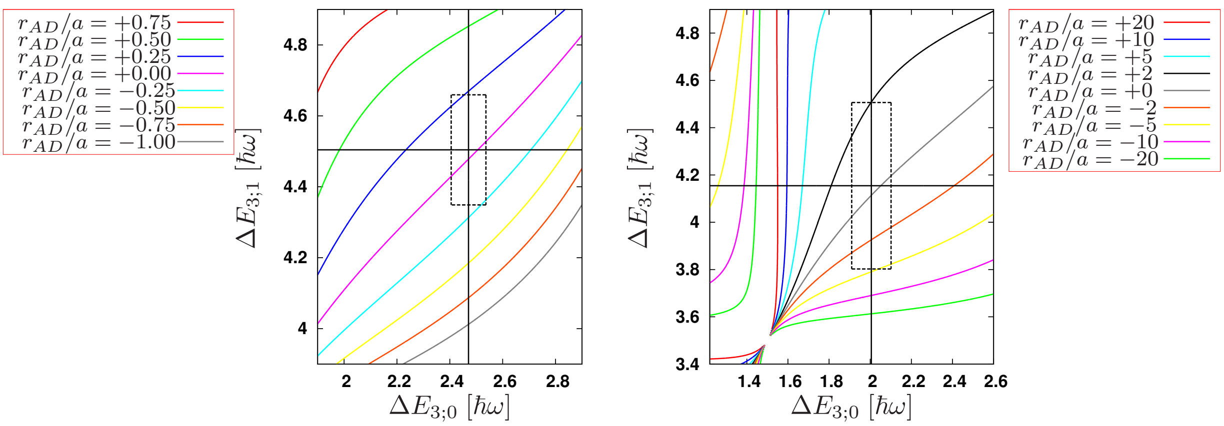

Figure 6.7: Contour plot of the ratio r_{AD}/a as a function of $\Delta E_{3;0}$ and $\Delta E_{3;1}$. The solid straight lines indicate the energies $\Delta E_{3;0}$ and $\Delta E_{3;1}$ extrapolated to $N \to \infty$. The rectangle enclosed by the dashed lines indicates the uncertainty region; one expects that this region contains the correct value. **Left panel**: $E^{(2)} = 0\ \hbar\omega$. **Right panel**: $E^{(2)} = -4\ \hbar\omega$.

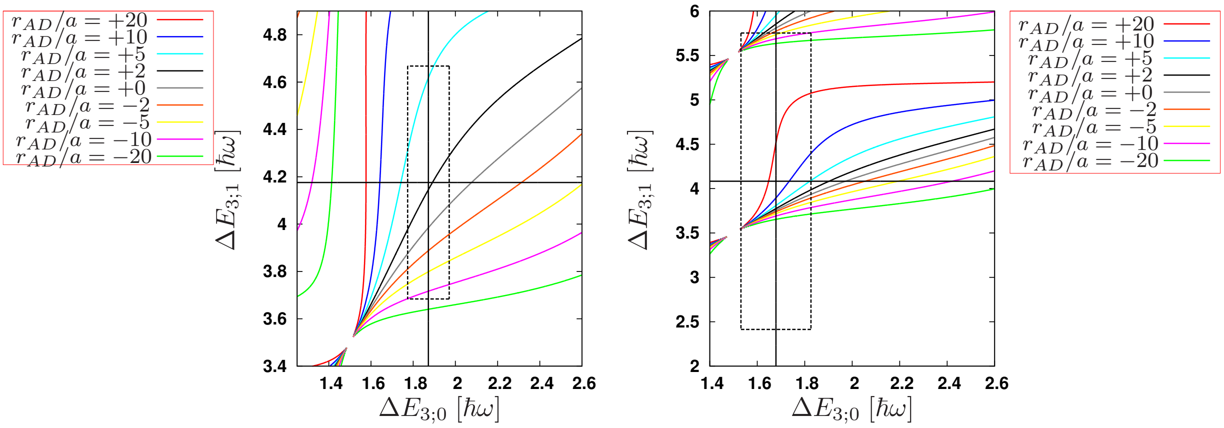

Figure 6.8: Contour plot of the ratio r_{AD}/a as a function of $\Delta E_{3;0}$ and $\Delta E_{3;1}$. The solid lines indicate the energies $\Delta E_{3;0}$ and $\Delta E_{3;1}$ extrapolated to $N \to \infty$. The rectangle enclosed by the dashed lines indicates the uncertainty region. One anticipates that this region contains the correct value. **Left panel**: $E^{(2)} = -10\ \hbar\omega$. **Right panel**: $E^{(2)} = -50\ \hbar\omega$.

energy. Thus the relevant energy is

$$\Delta E_{4;n} = E_{4,n} - 2E_{2,0}\ . \tag{6.14}$$

Additionally, the reduced mass of the dimer-dimer system is $\mu_{DD} = m$. The ratio between the oscillator lengths b and b_{DD} is given in this case by $b_{DD} = b/\sqrt{2}$.

With the shell-model approach the energy spectrum of this four-body system is calculated for various renormalisation energies $E^{(2)}$ and values of the cutoff parameter N. Afterwards, the ground state energies, the first excited state energies and their extrapolations are used to determine the scattering observables. The reference value is

$$a_{DD}/a = 0.6\ , \tag{6.15}$$

which was predicted by Petrov et al. [102]. Unfortunately, both difficulties arising from the uncertainties and poles in the functions are even more severe in the four-body sector. At first, it is more elaborate to calculate the energy spectra and consequently, only smaller values of cutoff parameter N are numerically tractable. Hence, the extrapolations, in particular for the first excited state, contain larger uncertainties. Secondly, the extrapolated combination of $\Delta E_{4;0}(\infty)$ and $\Delta E_{4;1}(\infty)$ lie often at awkward positions in the proximity of poles. As examples, the contour plots for $E^{(2)} = -0.5\ \hbar\omega$ $(a/b = 0.88)$ and $E^{(2)} = -1\ \hbar\omega$ $(a/b = 0.68)$ as well as $E^{(2)} = -4\ \hbar\omega$ $(a/b = 0.35)$ and $E^{(2)} = -5\ \hbar\omega$ $(a/b = 0.32)$ are presented in Figures 6.9 and 6.10, respectively.

In these figures the horizontal and vertical black lines mark extrapolated energy levels for $\Delta E_{4;0}(N)$ and $\Delta E_{4;1}(N)$. Their intersection points indicate the predicted value for the dimer-dimer scattering length a_{DD}/a. In Figure 6.9 one can extract the values $a_{DD}/a = 0.24$ and $a_{DD}/a = 0.03$ for $E^{(2)} = -0.5\ \hbar\omega$ and $E^{(3)} = -1\ \hbar\omega$, respectively. But one can recognise that the extracted values contain inestimable large uncertainties because of the poles in their vicinity. It is not possible to verify the adaption of equation (6.10) to the dimer-dimer scattering for these renormalisation energies.

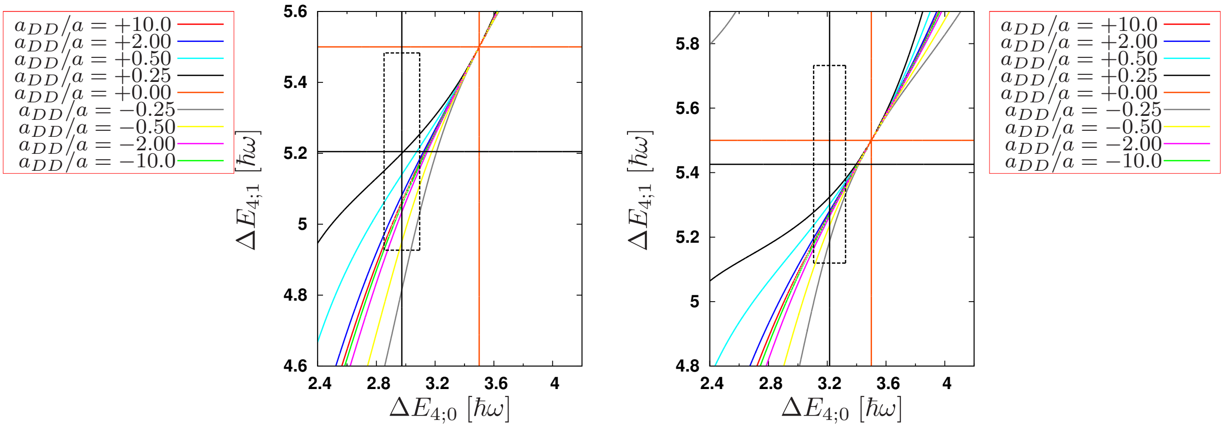

Figure 6.9: Contour plot of the ratio a_{DD}/a as a function of $\Delta E_{4;0}$ and $\Delta E_{4;1}$. The solid horizontal and vertical black lines indicate the energies $\Delta E_{4;0}$ and $\Delta E_{4;1}$ extrapolated to $N \to \infty$. The rectangle enclosed by the dashed lines indicates the uncertainty region. One anticipates that this region contains the correct value. **Left panel**: $E^{(2)} = -0.5\ \hbar\omega$. **Right panel**: $E^{(2)} = -1\ \hbar\omega$.

In Figure 6.10 the results for $E^{(2)} = -4\ \hbar\omega$ and $E^{(2)} = -5\ \hbar\omega$ are shown. For the dimer-dimer scattering length the value $a_{DD}/a = -0.037$ and $a_{DD}/a = 0.22$ can be found at the intersection point of the extrapolated energies. In contrast to the former situation, the uncertainties are now small. Particularly for the left panel, it follows that the result is inconsistent with the reference value $a_{DD}/a = 0.6$. Only at the lower edge the reference value lies in the uncertainty rectangle. To a lesser extent, this statement is correct for the right panel. Here the correct value lies slightly more in the middle of the uncertainty rectangle.

In conclusion, the extraction of dimer-dimer scattering observables for the four-body sector in a harmonic confinement seems to be problematic. For the example with $E^{(2)} = -4\ \hbar\omega$ one finds that the result contradicts the reference value. For the other renormalisation energies the large uncertainties in the results impede an interpretation. It thus remains doubtful if the adaption of the formula from the atom-dimer approach is indeed correct.

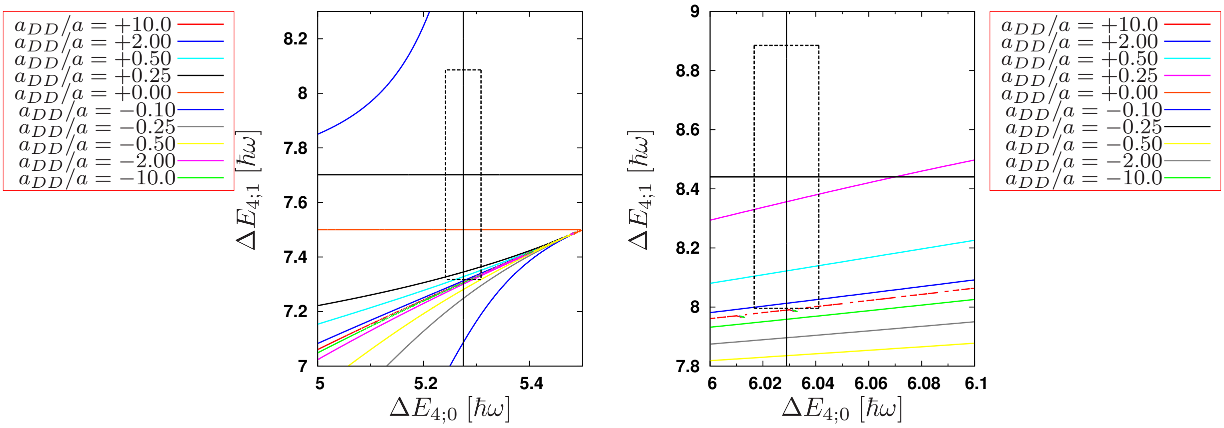

Figure 6.10: Contour plot of the ratio a_{DD}/a as a function of $\Delta E_{4;0}$ and $\Delta E_{4;1}$. The solid horizontal and vertical black lines indicate the energies $\Delta E_{4;0}$ and $\Delta E_{4;1}$ extrapolated to $N \to \infty$. The rectangle enclosed by the dashed lines indicates the uncertainty region. One anticipates that this region contains the correct value. **Left panel**: $E^{(2)} = -4\ \hbar\omega$. **Right panel**: $E^{(2)} = -5\ \hbar\omega$.

6.2 Description of Resonances with a Shell Model

In this section the possibility to study the energy and the width of resonances within the shell-model approach is investigated. For this purpose, the two-boson system with repulsive smeared contact interactions is considered. Due to the separability of the interaction the T-matrix itself is separable and in momentum space reads (see appendix C.2)

$$\langle \vec{p}|T(z)|\vec{p}\,'\rangle = \left(\frac{1}{g^{(2)}} - B(z)\right)^{-1} v(\vec{p})v(\vec{p}\,')\ , \tag{6.16}$$

where $v(\vec{p}) := \exp(-|\vec{p}|^2\epsilon^2/2)$ and

$$B(z) = \frac{m}{\pi^2}\int_0^\infty \mathrm{d}w\ \frac{w^2 e^{-\epsilon^2 w^2}}{2mz - w^2}\ . \tag{6.17}$$

With the substitution $z = (q^2 + i\Delta)/(2m)$ one finds from appendix D

$$\lim_{\Delta\downarrow 0} B(q^2 + i\Delta) = \frac{m}{\pi^2}(-\sqrt{\pi})\left(\frac{1}{2\epsilon} - qF(\epsilon q) + i\frac{\sqrt{\pi}}{2}pe^{-\epsilon^2 q^2}\right)\ , \tag{6.18}$$

where

$$F(x) := e^{-x^2}\int_0^x \mathrm{d}y\ e^{y^2} \tag{6.19}$$

is Dawson's integral.

A resonance at the energy $E_R = q^2/(2m)$ corresponds to a pole in the T-matrix $T(q^2)$ at momenta q with negative imaginary part in the vicinity of the real axis. On the real axis the resonance manifests in a peak of the on-shell T-matrix with the width Γ approximately described by the Breit-Wigner formula:

$$\langle p|T(E \approx E_R)|p\rangle \propto \frac{(\Gamma/2)}{(E - E_R)^2 + (\Gamma/2)^2}\ , \tag{6.20}$$

where $p = \sqrt{2mE}$.

Figure 6.11 shows the transition amplitude $t(p \leftarrow p)$ for the smeared contact interactions with the coupling constant $mg^{(2)}/\epsilon = 100$. One recognises a peak in the amplitude at the energy $E_R \approx 3.2\,\frac{1}{m\epsilon^2}$ with a width $\Gamma \approx 0.2\frac{1}{m\epsilon^2}$.

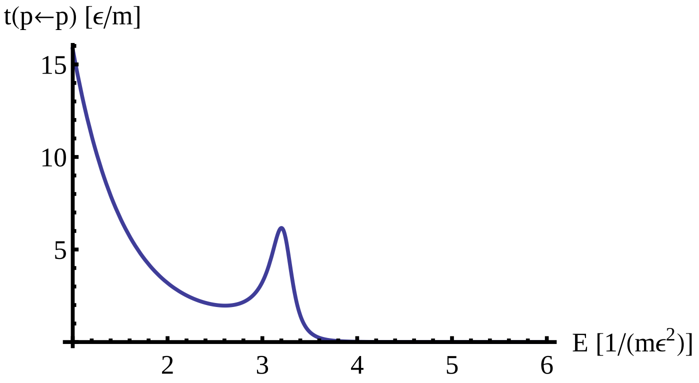

Figure 6.11: On-shell T-matrix $t(p \leftarrow p)$ versus the energy $E = p^2/(2m)$ for the smeared contact interaction $\langle \vec{s} | g^{(2)} V_\epsilon | \vec{s}\,' \rangle = \frac{g^{(2)}}{(2\pi\epsilon^2)^3} \exp\left(-\frac{|\vec{s}|}{2\epsilon^2}\right) \exp\left(-\frac{|\vec{s}\,'|}{2\epsilon^2}\right)$ with $mg^{(2)}/\epsilon = 100$.

Likewise, one finds for more repulsive interactions sharper resonances with the detection of peaks in the T-matrix. A selection of coupling constants $g^{(2)}$ with the corresponding resonance energies E_R and their widths Γ is collected in Table 6.2.

$mg^{(2)}/\epsilon$	100	200	300	400
E_R	3.2	5.36	7.5528	9.77722
Γ	0.24	0.02	$6.8 \cdot 10^{-4}$	$1.6 \cdot 10^{-5}$

Table 6.2: Selection of coupling constants $mg^{(2)}/\epsilon$ and their corresponding resonance energies E_R and widths Γ. Both are given in the energy unit $1/(m\epsilon^2)$.

In the next step the two-body problem is solved within the shell-model approach. The matrix elements of the Hamiltonian in oscillator states $\langle s_1^{(b)} | nlm \rangle$ are given by

$$ {}_b\langle n'l'm' | H | nlm \rangle_b = \frac{1}{m\ell^2} \left(\frac{1}{\beta^2}\, {}_1\langle n'l'm' | T_{\text{kin}} | nlm \rangle_1 + \frac{mg^{(2)}}{\ell} \frac{1}{\beta^3}\, {}_1\langle n'l'm' | V_\epsilon | nlm \rangle_1 \right) , \quad (6.21) $$

where ℓ is an arbitrary length scale, T_{kin} is the kinetic energy operator and $\beta = b/\ell$ is the oscillator length b in units of the length scale ℓ. The range of the interaction ϵ is chosen as the length scale, i.e. $\ell = \epsilon$.

As two examples, Figure 6.12 shows the complete energy spectrum for $N = 10$ with vanishing relative angular momentum versus $\beta = b/\epsilon$ for $mg^{(2)}/\epsilon = 100$ and $mg^{(2)}/\epsilon = 400$. In spite of the small cutoff parameter N one sees a noticeable structure in the β dependence at energy levels around the resonances energies $E_R = 3.2\,\frac{1}{m\epsilon^2}$ and $E_R = 9.77722\,\frac{1}{m\epsilon^2}$ in the left and right panel, respectively. The behaviour of the highest excited state is salient. At first, it decreases with increasing β up to the resonance energy and afterwards, it keeps approximately constant for a wide region of β. Furthermore, the behaviour of the ground state is remarkable in the right panel. There

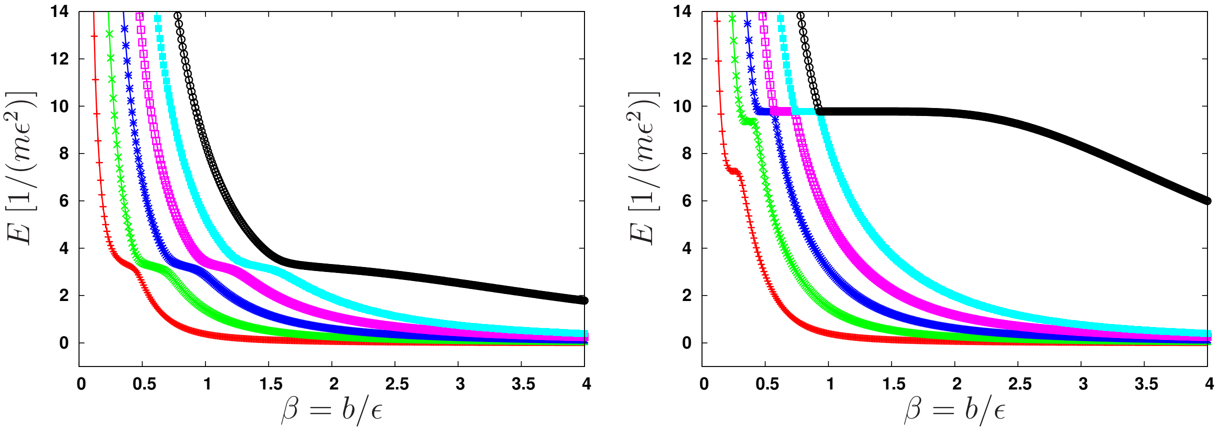

Figure 6.12: Energy spectrum for the two-body system with smeared contact interactions for $L^P = 0^+$ and $N = 10$. **Left panel**: $mg^{(2)}/\epsilon = 100$. **Right panel**: $mg^{(2)}/\epsilon = 400$.

is a plateau at $E \approx 7\,\frac{1}{m\epsilon^2}$ which seems to be related to the resonance. However, its energy level differs from E_R by $\Delta E \approx 2.7\frac{1}{m\epsilon^2}$.

In order to extract an estimate of the resonance position and its width from the energy spectrum, I show an enlarged area in Figure 6.13. Concentrating on the next-to-last excited states, the plateau of this state is bounded from left and right in contrast to the plateau in the highest excited state. The region of the plateau is marked with red horizontal lines. In the right panel the determination of this region is obvious for $mg^{(2)}/\epsilon = 400$. For the small coupling constant the plateau is not as distinctive as for the large one. Hence, the borders of the region themselves contain some uncertainty. The resonance energies are estimated with the arithmetic average of the borders and the corresponding uncertainties as the half of the distance of the borders. For $mg^{(2)}/\epsilon = 100$ and $mg^{(2)}/\epsilon = 400$ one finds $E_R = (3.21 \pm 0.22)\,\frac{1}{m\epsilon^2}$ and $E_R = (9.777218 \pm 2.5 \cdot 10^{-5})\,\frac{1}{m\epsilon^2}$, which is consistent with the values in Table 6.2. Moreover, the uncertainties are of the same order of magnitude as the width of the resonances.

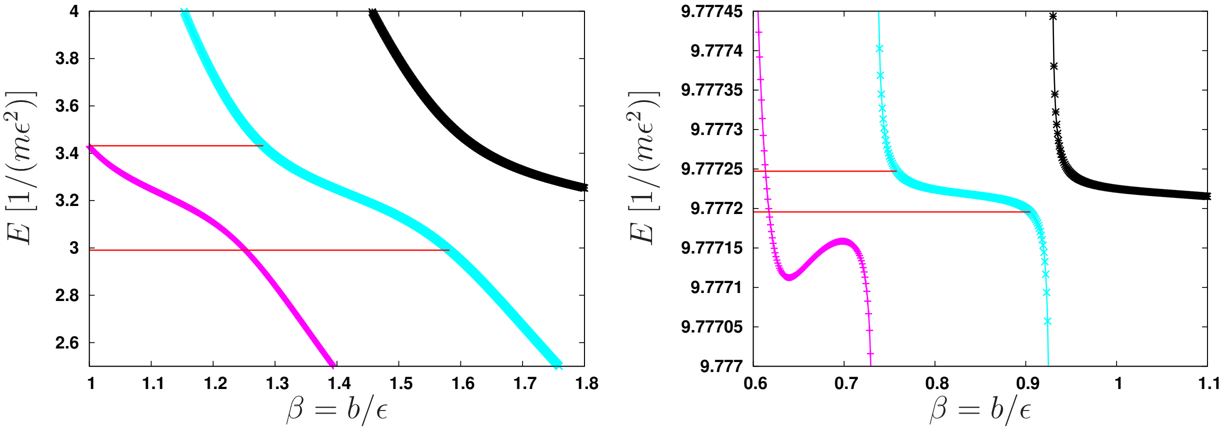

Figure 6.13: Energy spectrum for the two-body system with smeared contact interactions for $L^P = 0^+$ and $N = 10$. **Left panel**: $mg^{(2)}/\epsilon = 100$. **Right panel**: $mg^{(2)}/\epsilon = 400$.

In Table 6.3 resonance energies E_R in units of $\frac{1}{m\epsilon^2}$ for various coupling constants $g^{(2)}$ and cutoff parameters N are collected. The estimated resonance energies E_R and the corresponding uncertainties are independent of N. In larger model spaces it is not possible to determine the resonance energies more precisely. The uncertainties are for all N in the order of the width Γ of the resonances. For the smallest coupling constant $mg^{(2)}/\epsilon = 10$ the limits of the plateau are indeterminable for the larger cutoff parameter $N \geq 100$. Although the resonance energy itself can be identified with the help of the behaviour of the highest excited state, the uncertainties cannot be estimated from the next-to-last excited state.

N \ $mg^{(2)}/\epsilon$	100	200	300	400
10	3.21 ± 0.22	5.359 ± 0.018	$7.5529 \pm 1.0 \cdot 10^{-3}$	$9.777221 \pm 2.6 \cdot 10^{-5}$
100	-	5.359 ± 0.018	$7.5527 \pm 1.4 \cdot 10^{-3}$	$9.777218 \pm 2.5 \cdot 10^{-5}$
200	-	5.358 ± 0.015	$7.5528 \pm 1.3 \cdot 10^{-3}$	$9.777218 \pm 2.5 \cdot 10^{-5}$
300	-	5.360 ± 0.015	$7.5527 \pm 1.4 \cdot 10^{-3}$	$9.777211 \pm 5.2 \cdot 10^{-5}$
400	-	5.357 ± 0.014	$7.5527 \pm 1.8 \cdot 10^{-3}$	$9.777217 \pm 4.0 \cdot 10^{-5}$

Table 6.3: Estimated resonance energies E_R in $\frac{1}{m\epsilon^2}$ for various coupling constants $g^{(2)}$ and cutoff parameter N.

In conclusion, the numerical study of the repulsive smeared contact interaction in the two-body system suggests that the energy levels and widths of resonances can be extracted from the β-dependence of the energy spectrum in the model space. A sharp resonance corresponds to a distinctive plateau in the β-dependent energies. The corresponding width Γ can be extracted from the borders of the plateau. In order to formalise the prescription to estimate the resonance energies and widths, an approach used for the analyses of spectra in finite volumes could be helpful [103]. So far, only the two-body system is investigated. The extension on systems with more particles is straightforward. However, one expects more complicated spectra with several resonances.

Chapter 7

Conclusion and Outlook

In this thesis, I have covered issues ranging from the implementation and comparison of two different shell-model approaches, their application to bosonic systems with and without external confinement and finally to the extraction of scattering properties from energy spectra in a harmonic oscillator potential.

In the first shell-model framework I used the so-called M-scheme. In this scheme the many-body basis consists of the product of oscillator functions in one-particle coordinates. In contrast, the basis in the second framework consists of the angular momentum coupled oscillator functions expressed in relative coordinates, the so-called J-scheme. In the J-scheme the most time-consuming task is the construction of the symmetrised many-body basis and corresponding transformation matrices. This has to be done only once for a specific model space independently from the interaction. Hence, in a comparison of the M-scheme with the J-scheme procedure I have found a definite preference for the latter in order to determine energy spectra for various potentials globally, i.e. for a variety of coupling constants and parameter combinations.

However, for a specific problem the performance depends on the number of particles, the actual implementation and the hardware. For up to six particles the J-scheme is distinctly more advantageous than the M-scheme. For systems with more particles this is not so obvious since one should note that the most time-consuming part of the M-scheme is the diagonalisation of the many-body Hamiltonian; matrix diagonalisation is a standard problem, which is highly parallelisable. In future applications, benchmarking the diagonalisation routines for the many-body Hamiltonian in the M-scheme would therefore be instructive.

At first the shell-model approach has been applied to systems consisting of bosons with spin 0 in a harmonic confinement. Assuming dominating scattering lengths a in the effective range expansion, the interactions have been approximated by two-body and three-body contact interactions; this is called the scaling limit. In the model space the corresponding coupling constants have been renormalised and adjusted to reproduce given two-body and three-body energy levels $E^{(2)}$ and $E^{(3)}$, respectively. Here, the two-body energy $E^{(2)}$ is directly related to the scattering length a. For systems with up to seven bosons selected energy spectra have been presented for various renormalisation energies $E^{(2)}$ and $E^{(3)}$ as a function of the cutoff parameter N. With quadratic polynomials in the variable $1/\sqrt{N}$ energy spectra in various model-spaces are extrapolated to the limit $N \to \infty$.

In particular, the dependence on $E^{(2)}$, or equivalently on the scattering length a, for constant three-body interactions has been studied in the four-body sector in detail. The harmonic confinement strongly modifies the energy spectra with the consequence that energy levels are mutually perturbed. Furthermore various avoided level crossings have been found.

Throughout, I have found a slow convergence of the binding energies in the dependence of the cutoff parameter N in all studies. This defies an accurate extrapolation with small uncertainties to the limit $N \to \infty$. As a possible expedient the contact interactions have been modified to finite-ranged separable Gaussian interactions of width ϵ. For the new interactions I have found that the energy values depending on N converges for finite width ϵ exponentially. This width ϵ has been used as an additional extrapolation parameter beside the cutoff parameter N. In a detailed uncertainty analysis the mutual dependence of the finite cutoff parameter N and the finite width ϵ has been studied. For practical applications, the appropriate prescription can be summarised briefly as: Use converged results in the cutoff parameter N or extrapolate in the cutoff parameter N for finite width ϵ first and then extrapolate in the width to $\epsilon = 0$ linearly.

For several renormalisation energies the energy spectra have been shown as a function of the width ϵ. Usually, the extrapolated binding energies in the width ϵ for smeared contact interactions and extrapolated energies in the cutoff parameter N for genuine contact interactions coincide within the estimated uncertainties. But for certain combinations of renormalisation energies I have observed that these extrapolations disagree with each other significantly. These deviations indicate an underestimation of the errors and reveal parameter combinations with problematic extrapolations. Therefore it would be interesting to study the reason for this behaviour for specific renormalisation energies and to extract precise energy values with larger model spaces or alternative procedures.

As an example for a system without an external confinement potential, which has a short range strongly repulsive interaction combined with an attractive interaction of long range, I have considered systems with few ^{4}He atoms. Using the shell-model approach the ground state binding energies of ^{4}He atom clusters $^4\mathrm{He}_A$ have been determined. In these studies the interaction between the ^{4}He atoms was described by the ab-initio two-body potential LM2M2. Due to the shape of this interaction the energy levels in the model spaces used show a very strong cutoff dependence. Therefore, it has not been possible to predict binding energies accurately for the genuine LM2M2 potential.

Alternatively, exploiting the unitary SRG-transformation the coupling of low and high energy physics can be reduced and a faster convergence has indeed been achieved. For various flow parameter Λ the ground state energies have been determined for up to ten atoms. These values have been compared to predictions with Monte-Carlo methods. However, unitary SRG-transformation induces many-body forces, which have so far been omitted in these calculations. As a consequence a large dependence of the results on the flow parameter Λ has still been found. In particular, as in nuclear physics, a non-monotonous behaviour has been observed. In order to stabilise the estimated binding energies, the induced three-body interactions should be included. However, this requires more sophisticated solutions of the integro-differential equation for the three-body SRG-transformation. Furthermore, up to now only the kinetic energy has been used as generator for the SRG-transformation. Possibly, this is an inappropriate choice and in future studies the use of alternative generators should be investigated.

Instead of constructing an effective interaction of the LM2M2 potential systematically with the SRG-evolution, I have also studied an effective parametric interaction consisting of two- and three-body Gaussian interactions, here called the Pisa potential. The strength and range of the attractive two-body force are chosen to reproduce the two-body ground state energy of the cluster $^4\mathrm{He}_2$, the scattering length a, and the effective range r_0 of the LM2M2 potential. The strength and range of the repulsive three-body force are not unique. There is an infinite number of possible combinations which reproduce the LM2M2 ground state energy for $^4\mathrm{He}_3$.

For a version of the Pisa potential with a relatively soft (and thus long-ranged) three-body Gaussian interaction, binding energies for clusters with up to twelve constituents have been estimated by linear extrapolations in the cutoff parameter N. Due to the soft repulsive interaction the dependence on N is weak and uncertainties in the extrapolation are acceptably small. In comparison with results based on Monte-Carlo procedures using the genuine LM2M2-potential the ground state energy differs only by at most $\Delta E/E = 10\%$ for up to ten atoms.

In two hard versions of the Pisa potential the strong short-ranged three-body Gaussians lead to a slower convergence in the cutoff parameter N. Hence, the predictions via linear extrapolations carry larger uncertainties. With the SRG-transformation, faster convergence in N have been achieved. However, the complex integro-differential equation in the transformation of three-body potentials constrains the magnitude of the angular momenta for which the SRG-transformed interactions can be calculated reliably. The influence of the higher angular momenta terms was found to be minor in a pilot study. However, this and the effects of multiple-body induced forces as well as the flow parameter dependence should be investigated systematically.

Apart from these three main parts, the shell-model approach has been used to extract atom-dimer and dimer-dimer scattering observables from the energy spectrum of the three- and four-body system with identical spin-$1/2$ fermions in a harmonic confinement. For various two-body scattering lengths the atom-dimer scattering length and effective range as well as the dimer-dimer scattering length have been studied. Because of the intricate behaviour of the modified Busch formula for the energies, the extraction of these scattering observables have large uncertainties or could not been determined at all.

Finally, in the two-body system without any confinement it has been shown for the example of smeared contact interactions that the position and width of a resonance can be extracted from the energy spectrum dependence on the oscillator length b for a constant cutoff parameter N. Remarkably, these quantities can be determined even for small cutoff parameters. An extension of this method to systems with more particles would certainly be interesting.

Appendix A

Jacobi Coordinates

Jacobi coordinates are a set of coordinates to describe the relative motion in many-body systems. They are used for example to separate the centre-of-mass motion in a harmonic oscillator confinement potential. For two particles at positions $\vec{x}_1$ and $\vec{x}_2$ the Jacobi coordinates are defined by:

$$\vec{s}_1 := \frac{1}{\sqrt{2}}\left(\vec{x}_1 - \vec{x}_2\right) \ , \tag{A.1a}$$

$$\vec{R}_2 := \frac{1}{\sqrt{2}}\left(\vec{x}_1 + \vec{x}_2\right) \ , \tag{A.1b}$$

where $\vec{s}_1$ is the first Jacobi coordinate and $\vec{R}_2$ the corresponding centre-of-mass. The Jacobi coordinates fulfil the relation

$$\left|\vec{x}_1\right|^2 + \left|\vec{x}_2\right|^2 = \left|\vec{s}_1\right|^2 + \left|\vec{R}_2\right|^2 . \tag{A.2}$$

Hence, the transformation from single-particle coordinates $\vec{x}_1$ and $\vec{x}_2$ onto Jacobi coordinates is an orthogonal and isometric transformation. In general, for A particles at positions $\vec{x}_1$, $\vec{x}_2$,. . .,$\vec{x}_A$ the Jacobi coordinates are defined by

$$\vec{s}_n := \frac{1}{\sqrt{(n+1)\,n}}\left(\vec{x}_1 + \vec{x}_2 + \cdots + \vec{x}_n - n\cdot\vec{x}_{n+1}\right) \qquad n = 1,\ldots,A-1\,, \tag{A.3a}$$

$$\vec{R}_A := \frac{1}{\sqrt{N}}\left(\vec{x}_1 + \vec{x}_2 + \cdots + \vec{x}_A\right) \ . \tag{A.3b}$$

Again, the transformation is orthogonal and isometric:

$$\left|\vec{x}_1\right|^2 + \left|\vec{x}_2\right|^2 + \cdots + \left|\vec{x}_N\right|^2 = \left|\vec{s}_1\right|^2 + \cdots + \left|\vec{s}_{(N-1)}\right|^2 + \left|\vec{R}_A\right|^2 \tag{A.4}$$

and as a consequence also for the sum of laplace-operators one finds

$$\Delta_{\vec{x}_1} + \Delta_{\vec{x}_2} + \cdots + \Delta_{\vec{x}_N} = \Delta_{\vec{s}_1} + \Delta_{\vec{s}_2} + \cdots + \Delta_{\vec{s}_{(N-1)}} + \Delta_{\vec{R}_A} \ . \tag{A.5}$$

From Eq. (A.4) and (A.5) it follows that the centre-of-mass motion can be separated for the A-body harmonic oscillator, i.e. one finds

$$H = \sum_{i=1}^{A}\left(-\frac{\Delta_{x_i}}{2m} + \frac{1}{2}m\omega^2\left|\vec{x}_i\right|^2\right) \ , \tag{A.6}$$

$$= \sum_{i=1}^{A-1}\left(-\frac{\Delta_{\vec{s}_i}}{2m} + \frac{1}{2}m\omega^2\left|\vec{s}_i\right|^2\right) + \left(-\frac{\Delta_{\vec{R}_A}}{2m} + \frac{1}{2}m\omega^2\left|\vec{R}_A\right|^2\right) \ . \tag{A.7}$$

Appendix B

Talmi-Moshinsky Transformation

The orthogonal and isometric Talmi transformation maps a set of two coordinates $\vec{\rho}$ and $\vec{\lambda}$ onto a new set of coordinates $\vec{\rho}\,'$ and $\vec{\lambda}\,'$:

$$\begin{pmatrix} \vec{\rho}\,' \\ \vec{\lambda}\,' \end{pmatrix} = \underbrace{\begin{pmatrix} \sqrt{\frac{1}{1+d}} & -\sqrt{\frac{d}{1+d}} \\ \sqrt{\frac{d}{1+d}} & \sqrt{\frac{1}{1+d}} \end{pmatrix}}_{M_d} \cdot \begin{pmatrix} \vec{\rho} \\ \vec{\lambda} \end{pmatrix} \quad , \quad d \in \mathbb{R},\ d \geq 0 \ . \tag{B.1}$$

where M_d is a general orthogonal matrix. For historical reasons the matrix is parametrised by the weight d. For example, the matrix M_1 is the orthogonal and isometric transformation from the set of two single-particle coordinates $\vec{x}_1$ and $\vec{x}_2$ onto the Jacobi coordinates $\vec{s}_1$ and $\vec{R}_2$:

$$\begin{pmatrix} \vec{s}_1 \\ \vec{R}_2 \end{pmatrix} = M_1 \cdot \begin{pmatrix} \vec{x}_1 \\ \vec{x}_2 \end{pmatrix} \quad . \tag{B.2}$$

A particular feature of the Talmi transformation is that the angular momentum coupled oscillator function $\left[\phi_{n_\rho l_\rho}(\vec{\rho}) \otimes \phi_{n_\lambda l_\lambda}(\vec{\lambda})\right]^L_M$ depending on the coordinates $\vec{\rho}$ and $\vec{\lambda}$ is a finite linear combination of angular momentum coupled oscillator function $\left[\phi_{n_{\rho'} l_{\rho'}}(\vec{\rho}\,') \otimes \phi_{n_{\lambda'} l_{\lambda'}}(\vec{\lambda}\,')\right]^L_M$ depending on the coordinates $\vec{\rho}\,'$ and $\vec{\lambda}\,'$. The corresponding coefficients are given by the so-called Brody-Moshinsky brackets $\left\langle n_{\rho'} l_{\rho'} n_{\lambda'} l_{\lambda'}; L \middle| n_\rho l_\rho, n_\lambda l_\lambda \right\rangle_d$ [63], i.e.

$$\begin{aligned} &\left[\phi^{(b)}_{n_\rho l_\rho}\left(\vec{\rho}\right) \otimes \phi^{(b)}_{n_\lambda l_\lambda}\left(\vec{\lambda}\right)\right]^L_M = \\ &\qquad \sum_{n_{\rho'} l_{\rho'} n_{\lambda'} l_{\lambda'}} \underbrace{\left\langle n_{\rho'} l_{\rho'}, n_{\lambda'} l_{\lambda'}; L \middle| n_\rho l_\rho, n_\lambda l_\lambda \right\rangle_d}_{\text{Brody-Moshinsky-Brackets}} \left[\phi^{(b)}_{n_{\vec{\rho}\,'} l_{\vec{\rho}\,'}}\left(\vec{\rho}\,'\right) \otimes \phi^{(b)}_{n_{\vec{\lambda}\,'} l_{\vec{\lambda}\,'}}\left(\vec{\lambda}\,'\right)\right]^L_M \quad , \end{aligned} \tag{B.3}$$

where the sum is subject to following constraints:

- energy conservation: $N := 2n_{\rho'} + l_{\rho'} + 2n_{\lambda'} + l_{\lambda'} \overset{!}{=} 2n_\rho + l_\rho + 2n_\lambda + l_\lambda$,
- parity conservation: $(-1)^{l'_{\rho'} + l'_{\lambda'}} \overset{!}{=} (-1)^{l_\rho + l_\lambda}$,
- total angular momentum conservation.

Appendix C

Smeared Contact Interactions

C.1 Matrix Elements of Smeared Contact Interactions

In section 4.3, the following expression for matrix elements of the smeared contact interactions in the oscillator functions are used:

$$\big\langle n_1 l_1 \big| V_G \big| n_1' l_1' \big\rangle = \frac{1}{(1+\epsilon^2)^3} \phi_{n_1 0}(0) \Big(\frac{1-\epsilon^2}{1+\epsilon^2}\Big)^{n_1} \phi_{n_1' 0}(0) \Big(\frac{1-\epsilon^2}{1+\epsilon^2}\Big)^{n_1'} \delta_{l_1,0}\ \delta_{l_1',0}\ . \tag{C.1}$$

In this section, the corresponding derivation is given. For the seperable smeared contact interaction

$$\big\langle \vec{s} \big| V_G \big| \vec{s}\,' \big\rangle = \frac{1}{(2\pi\epsilon^2)^3} e^{-\frac{\vec{s}^2}{2\epsilon^2}} e^{-\frac{\vec{s}'^2}{2\epsilon^2}}\ , \tag{C.2}$$

the matrix elements are given by

$$\big\langle n_1 l_1 \big| V_G \big| n_1' l_1' \big\rangle = \frac{1}{(2\pi\epsilon^2)^3} \int \mathrm{d}^3 s\ \phi_{nl}(\vec{s}) e^{-\frac{\vec{s}^2}{2\epsilon^2}} \int \mathrm{d}^3 s'\ \phi_{nl}(\vec{s}\,') e^{-\frac{\vec{s}'^2}{2\epsilon^2}}\ . \tag{C.3}$$

Then, by straightforward computation one finds:

$$\int \mathrm{d}^3 s\ \phi_{nl}(\vec{s}) e^{-\frac{\vec{s}^2}{2\epsilon^2}} = \delta_{l,0}\, \sqrt{4\pi} \int_0^\infty \mathrm{d}r\ r^2 e^{-\frac{r^2}{2\epsilon^2}} R_{n0}(r) \tag{C.4}$$

$$= \delta_{l,0}\, \sqrt{4\pi} N_{n0} \int_0^\infty \mathrm{d}r\ r^2 e^{-\frac{1}{2}(1+\frac{1}{\epsilon^2})r^2} L_n^{(\frac{1}{2})}(r^2)\ , \tag{C.5}$$

with the associated Laguerre polynomials $L_n^{(\frac{1}{2})}$ and the normalisation factor

$$N_{n0} := \sqrt{\frac{1}{\sqrt{4\pi}} \frac{2^{n+3} n!}{(2n+1)!!}}\ . \tag{C.6}$$

With the substitution of $r^2 = x$ and the definition $\rho^2 := \frac{1}{2}(1+\frac{1}{\epsilon^2})$, one finds for this integral, using the expansion of the Laguerre polynomials in monomials,

$$\begin{aligned}
\int \mathrm{d}^3 s\; \phi_{n0}(\vec{s})e^{-\frac{\vec{s}^2}{2\epsilon^2}} &= \frac{\sqrt{4\pi}N_{n0}}{2}\sum_{i=0}^{n}\frac{(-1)^i}{i!}\frac{\Gamma(n+\frac{3}{2})}{\Gamma(i+\frac{3}{2})\Gamma(n-i+1)}\int_0^\infty \mathrm{d}x\; x^{\frac{1}{2}+i}e^{-\rho^2 x} && \text{(C.7)}\\
&= \frac{\sqrt{4\pi}N_{n0}}{2}\sum_{i=0}^{n}\frac{(-1)^i}{i!}\frac{\Gamma(n+\frac{3}{2})}{\Gamma(n-i+1)}\frac{1}{\rho^{3+2i}} && \text{(C.8)}\\
&= \frac{\sqrt{4\pi}N_{n0}\Gamma(n+\frac{3}{2})}{2\rho^3}\frac{1}{n!}\sum_{i=0}^{n}\binom{n}{i}(-\rho^{-2})^i && \text{(C.9)}\\
&= \frac{\sqrt{4\pi}N_{n0}(2n+1)!!}{2^{n+2}n!\rho^{2n+3}}(\rho^2-1)^n\sqrt{\pi}\ . && \text{(C.10)}
\end{aligned}$$

Finally, the quantities ρ and N_{n0} are replaced by their definitions and one finds

$$\begin{aligned}
\left\langle n_1 l_1\middle|V_G\middle|n_1' l_1'\right\rangle &= \frac{\delta_{l_1,0}\ \delta_{l_1',0}}{\left(1+\epsilon^2\right)^3\pi^{\frac{3}{2}}}\sqrt{\frac{(2n_1+1)!!}{n_1!2^{n_1}}}\sqrt{\frac{(2n_1'+1)!!}{n_1'!2^{n_1'}}}\left(\frac{1-\epsilon^2}{1+\epsilon^2}\right)^{n_1}\left(\frac{1-\epsilon^2}{1+\epsilon^2}\right)^{n_1'} && \text{(C.11)}\\
&= \frac{1}{(1+\epsilon^2)^3}\phi_{n_1 0}(0)\Big(\frac{1-\epsilon^2}{1+\epsilon^2}\Big)^{n_1}\phi_{n_1' 0}(0)\Big(\frac{1-\epsilon^2}{1+\epsilon^2}\Big)^{n_1'}\delta_{l_1,0}\ \delta_{l_1',0}\ . && \text{(C.12)}
\end{aligned}$$

C.2 Effective Range Expansion for Smeared Contact Interactions

For separable potentials

$$\left\langle \vec{s}\middle|V\middle|\vec{s}'\right\rangle = g\omega(\vec{s})\omega(\vec{s}')\,, \tag{C.13}$$

the T-matrix is given by

$$\left\langle \vec{p}\middle|T(z)\middle|\vec{p}'\right\rangle = \left(\frac{1}{g}-B(z)\right)^{-1}v(\vec{p})v(\vec{p}') \qquad \text{with} \qquad B(z) := \int\frac{\mathrm{d}^3 q}{(2\pi)^3}\frac{|v(\vec{q})|^2}{z-\frac{q^2}{2m}} \tag{C.14}$$

as a solution of the Lippmann-Schwinger equation

$$T(z) = V + V(z-H_0)^{-1}T(z)\ . \tag{C.15}$$

Here, $v(\vec{p})$ denotes the Fourier transform of $\omega(\vec{s})$

$$v(\vec{p}) = \int \mathrm{d}^3 s\; e^{i\vec{p}\cdot\vec{s}}\omega(\vec{s})\ . \tag{C.16}$$

Separable central potentials only contribute to s-wave ($\ell = 0$) scattering and one finds for the scattering amplitude $f_\ell(p)$ for $\ell = 0$ with the effective range expansion

$$\begin{aligned}
f_0(p) &= -\frac{m}{2\pi}\lim_{\Delta\to 0}\left\langle\vec{p}\middle|T(p^2/2+i\Delta)\middle|\vec{p}'\right\rangle\,, && \text{(C.17)}\\
&= \left[-\frac{2\pi}{m}|v(p)|^{-2}\big(1/g - B(p^2/2+i\Delta)\big)\right]^{-1}\,, && \text{(C.18)}\\
&= \left[-\frac{1}{a}+\frac{1}{2}rp^2+\mathcal{O}(p^4)-ip\right]^{-1}\ . && \text{(C.19)}
\end{aligned}$$

For the smeared contact interaction one has

$$\omega(\vec{s}) = \frac{1}{(2\pi\epsilon^2)^{\frac{3}{2}}} e^{-\frac{\vec{s}^2}{2\epsilon^2}} \; , \qquad v(\vec{p}) = e^{-\frac{\vec{p}^2\epsilon^2}{2}} \; , \tag{C.20}$$

$$B(p^2/2 + i\Delta) = \frac{m}{\pi^2}\int_0^\infty \mathrm{d}q \, \frac{q^2 e^{-\epsilon^2 q^2}}{p^2 - q^2 + i\Delta} = \frac{m}{2\pi^2}\int_0^\infty \mathrm{d}k \, \frac{\sqrt{k} e^{-\epsilon^2 k}}{p^2 - k + i\Delta} \; , \tag{C.21}$$

where

$$\lim_{\Delta\to 0^+} \int_a^b \mathrm{d}x \, \frac{f(x)}{x \pm i\Delta} = \mp i\pi f(0) + \mathcal{P}\int_a^b \mathrm{d}x \, \frac{f(x)}{x} \; . \tag{C.22}$$

Then for the imaginary part

$$\Im\frac{1}{f_0} = -\pi 2\pi e^{+\epsilon^2 p^2} \frac{1}{2\pi^2} p e^{-\epsilon^2 p^2} = -p \tag{C.23}$$

and for the real part

$$\Re\frac{1}{f_0} = \left[-\frac{2\pi}{g} - \frac{m}{\pi} \underbrace{\left[\mathcal{P}\int_{-\infty}^{+\infty} \mathrm{d}q \, \frac{q^2 e^{-\epsilon^2 q^2}}{q^2 - p^2} \right]}_{A(p^2)} \right] e^{\epsilon^2 p^2} \tag{C.24}$$

follows. Moreover, it can be shown, that

$$A(p^2) = \sqrt{\pi}\frac{1 - 2\epsilon p \mathrm{F}(\epsilon p)}{\epsilon} \; , \tag{C.25}$$

where the Dawson function is defined by (see appendix D)

$$\mathrm{F}(x) = e^{-x^2}\int_0^x \mathrm{d}y \, e^{y^2} = x - \frac{2}{3}x^3 + \mathcal{O}(x^5) \; . \tag{C.26}$$

The functions $A(p^2)$ and $e^{\epsilon^2 p^2}$ can be expanded in powers of p^2. Since in particular the scattering length a and the effective range r_0 are to be determined the expansion is terminated at $\mathcal{O}(p^4)$:

$$-\frac{1}{a} + \frac{1}{2} r_0 p^2 + \mathcal{O}(p^4) = -\left(\frac{2\pi}{gm} + \frac{1}{\sqrt{\pi}\epsilon}\right) + \frac{1}{2}\left(\frac{2\epsilon}{\sqrt{\pi}} - \frac{4\pi\epsilon^2}{gm}\right) p^2 + \mathcal{O}(p^4) \; . \tag{C.27}$$

Note that the vector $\vec{s}$ is the first Jacobi coordinate and $\vec{p}$ the corresponding Jacobi momentum. However, the ERE is canonically defined in the relative coordinate $\vec{x} = \vec{x}_1 - \vec{x}_2$. In this coordinate the potential reads

$$\langle \vec{x} | V | \vec{y} \rangle = \left[2\sqrt{2}g\right] \frac{1}{\left(2\pi\left[\sqrt{2}\epsilon\right]^2\right)^{3/2}} e^{-\frac{x^2}{2[\sqrt{2}\epsilon]^2}} \frac{1}{\left(2\pi\left[\sqrt{2}\epsilon\right]^2\right)^{3/2}} e^{-\frac{y^2}{2[\sqrt{2}\epsilon]^2}} \tag{C.28}$$

Hence, the scattering length a and the effective range r_0 in canonical relative coordinates read

$$1/a = 1/\sqrt{2}\left(\frac{2\pi}{2g\mu} + \frac{1}{\sqrt{\pi}\epsilon}\right) \; , \qquad r_0 = \sqrt{2}\left(\frac{2\epsilon}{\sqrt{\pi}} - \frac{4\pi\epsilon^2}{2g\mu}\right) \; , \tag{C.29}$$

with the reduced mass $\mu = m/2$.

Appendix D

Dawson Integral

To calculate:

$$A(p^2) = \lim_{\varepsilon \downarrow 0} \int_0^\infty \mathrm{d}q \, \frac{q^2 \, \mathrm{e}^{-b^2 \, q^2}}{q^2 - p^2 - i\varepsilon} \tag{D.1}$$

Substituting $y := b\,q\,, x = b\,p$:

$$A(p^2) = \lim_{\varepsilon \downarrow 0} \frac{1}{b} \int_0^\infty \mathrm{d}y \, \frac{y^2 \, \mathrm{e}^{-y^2}}{y^2 - x^2 - \mathrm{i}\varepsilon} = \lim_{\varepsilon \downarrow 0} \frac{1}{b} \int_0^\infty \mathrm{d}y \, \frac{y^2 \, \mathrm{e}^{-y^2}}{y^2 - (x + \mathrm{i}\varepsilon)^2} \, .$$

Now, from ABRAMOWITZ & STEGUN [97] (**7.1.3**) :

$$w(z) := \mathrm{e}^{-z^2} \left(1 + \frac{2\,\mathrm{i}}{\sqrt{\pi}} \int_0^z \mathrm{d}t \, \mathrm{e}^{t^2} \right) = \mathrm{e}^{-z^2} \mathrm{erfc}(-\mathrm{i}\, z) \tag{D.2}$$

and (**7.1.4**) :

$$w(z) = \frac{\mathrm{i}}{\pi} \int_{-\infty}^{\infty} \mathrm{d}t \, \frac{\mathrm{e}^{-t^2}}{z - t} = \frac{2\,\mathrm{i}\, z}{\pi} \int_0^\infty \mathrm{d}t \, \frac{\mathrm{e}^{-t^2}}{z^2 - t^2} \quad (\Im z > 0) \, . \tag{D.3}$$

Indeed, (D.2) and (D.3) are equivalent: Write $z = x + \mathrm{i}\varepsilon \, , \varepsilon > 0$. Then

$$\begin{aligned} w(x + \mathrm{i}\varepsilon) &= \frac{2\,\mathrm{i}\,(x + \mathrm{i}\varepsilon)}{\pi} \int_0^\infty \mathrm{d}t \, \frac{\mathrm{e}^{-t^2}}{(x + \mathrm{i}\varepsilon)^2 - t^2} \\ &= \frac{\mathrm{i}}{\pi} \int_0^\infty \mathrm{d}t \, \mathrm{e}^{-t^2} \left(\frac{1}{x + \mathrm{i}\varepsilon + t} + \frac{1}{x + \mathrm{i}\varepsilon - t} \right) \\ &= \frac{\mathrm{i}}{\pi} \left(- \int_0^{-\infty} \mathrm{d}t \, \frac{\mathrm{e}^{-t^2}}{x + \mathrm{i}\varepsilon - t} + \int_0^\infty \mathrm{d}t \, \frac{\mathrm{e}^{-t^2}}{x + \mathrm{i}\varepsilon - t} \right) = \frac{\mathrm{i}}{\pi} \int_{-\infty}^\infty \mathrm{d}t \, \frac{\mathrm{e}^{-t^2}}{x + \mathrm{i}\varepsilon - t} \, . \end{aligned}$$

Now

$$-2\,\mathrm{i} \int_0^\infty \mathrm{d}u \, \mathrm{e}^{2\mathrm{i}(x + \mathrm{i}\varepsilon \pm t)u} = -2\,\mathrm{i} \left. \frac{\mathrm{e}^{2\mathrm{i}(x \pm t)u} \mathrm{e}^{-2\,\varepsilon\, u}}{2\mathrm{i}(x + \mathrm{i}\varepsilon \pm t)} \right|_0^\infty = \frac{1}{x + \mathrm{i}\varepsilon \pm t} \, .$$

Therefore, with

$$\int_0^\infty \mathrm{d}t \, \mathrm{e}^{-(t+z)^2} = \int_z^\infty \mathrm{d}x \, \mathrm{e}^{-x^2} =: \frac{\sqrt{\pi}}{2} \mathrm{erfc}(z)$$

we find

$$\begin{aligned}
&w(x+\mathrm{i}\varepsilon)\\
&\quad= \frac{2}{\pi}\int_0^\infty \mathrm{d}t \int_0^\infty \mathrm{d}u\, \left(\mathrm{e}^{-t^2+2\mathrm{i}(x+\mathrm{i}\varepsilon+t)u} + \mathrm{e}^{-t^2+2\mathrm{i}(x+\mathrm{i}\varepsilon-t)u}\right)\\
&\quad= \frac{2}{\pi}\int_0^\infty \mathrm{d}u \int_0^\infty \mathrm{d}t\, \left(\mathrm{e}^{-(t-\mathrm{i}u)^2} + \mathrm{e}^{-(t+\mathrm{i}u)^2}\right) \mathrm{e}^{-(u-\mathrm{i}(x+\mathrm{i}\varepsilon))^2}\mathrm{e}^{-(x+\mathrm{i}\varepsilon)^2}\\
&\quad= \frac{2}{\pi}\int_0^\infty \mathrm{d}u\, \frac{\sqrt{\pi}}{2}\underbrace{(\mathrm{erfc}(-\mathrm{i}u)+\mathrm{erfc}(\mathrm{i}u))}_{=2}\mathrm{e}^{-(u-\mathrm{i}(x+\mathrm{i}\varepsilon))^2}\mathrm{e}^{-(x+\mathrm{i}\varepsilon)^2}\\
&\quad= \frac{2}{\sqrt{\pi}}\mathrm{e}^{-(x+\mathrm{i}\varepsilon)^2}\int_0^\infty \mathrm{d}u\, \mathrm{e}^{-(u-\mathrm{i}(x+\mathrm{i}\varepsilon))^2} = \frac{2}{\sqrt{\pi}}\mathrm{e}^{-(x+\mathrm{i}\varepsilon)^2}\frac{\sqrt{\pi}}{2}\mathrm{erfc}(-\mathrm{i}(x+\mathrm{i}\varepsilon))\\
&\quad= \mathrm{e}^{-(x+\mathrm{i}\varepsilon)^2}\mathrm{erfc}(-\mathrm{i}(x+\mathrm{i}\varepsilon))\,.
\end{aligned}$$

Finally,

$$\begin{aligned}
\mathrm{erfc}(-\mathrm{i}\,z) &= \frac{2}{\sqrt{\pi}}\int_{-\mathrm{i}\,z}^\infty \mathrm{d}t\,\mathrm{e}^{-t^2} = \frac{2}{\sqrt{\pi}}\int_{-\mathrm{i}\,z}^0 \mathrm{d}t\,\mathrm{e}^{-t^2} + \frac{2}{\sqrt{\pi}}\int_0^\infty \mathrm{d}t\,\mathrm{e}^{-t^2}\\
&= -\frac{2\,\mathrm{i}}{\sqrt{\pi}}\int_z^0 \mathrm{d}u\,\mathrm{e}^{u^2} + 1 = 1 + \frac{2\,\mathrm{i}}{\sqrt{\pi}}\int_0^z \mathrm{d}u\,\mathrm{e}^{u^2}\,.
\end{aligned}$$

Thus

$$\begin{aligned}
&\lim_{\varepsilon\downarrow 0}\int_0^\infty \mathrm{d}y\,\frac{y^2\,\mathrm{e}^{-y^2}}{y^2-(x+\mathrm{i}\varepsilon)^2}\\
&\quad= \lim_{\varepsilon\downarrow 0}\int_0^\infty \mathrm{d}y\,\frac{(x^2-y^2)\,\mathrm{e}^{-y^2}}{(x+\mathrm{i}\varepsilon)^2-y^2} - \lim_{\varepsilon\downarrow 0}x^2\int_0^\infty \mathrm{d}y\,\frac{\mathrm{e}^{-y^2}}{(x+\mathrm{i}\varepsilon)^2-y^2}\\
&\quad= \int_0^\infty \mathrm{d}y\;\mathrm{e}^{-y^2} - \frac{\pi\,x^2}{2\,\mathrm{i}\,x}\lim_{\varepsilon\downarrow 0}w(x+\mathrm{i}\varepsilon) = \frac{\sqrt{\pi}}{2} + \mathrm{i}\frac{\pi\,x}{2}\lim_{\varepsilon\downarrow 0}w(x+\mathrm{i}\varepsilon)\\
&\quad= \frac{\sqrt{\pi}}{2} + \mathrm{i}\frac{\pi\,x}{2}\,\mathrm{e}^{-x^2}\left(1+\frac{2\mathrm{i}}{\sqrt{\pi}}\int_0^x \mathrm{d}y\,\mathrm{e}^{y^2}\right)\\
&\quad= \frac{\sqrt{\pi}}{2} + \mathrm{i}\frac{\pi\,x}{2}\,\mathrm{e}^{-x^2} - \sqrt{\pi}\,x\,\mathrm{e}^{-x^2}\int_0^x \mathrm{d}y\,\mathrm{e}^{y^2} = \frac{\sqrt{\pi}}{2} + \mathrm{i}\frac{\pi\,x}{2}\,\mathrm{e}^{-x^2} - \sqrt{\pi}\,x\,F(x)\,,
\end{aligned}$$

where

$$F(x) := \mathrm{e}^{-x^2}\int_0^x \mathrm{d}y\,\mathrm{e}^{y^2} \tag{D.4}$$

is DAWSON's Integral. Now $F(0)=0$ and

$$F'(x) = -2\,x\,\mathrm{e}^{-x^2}\int_0^x \mathrm{d}y\,\mathrm{e}^{y^2} + \mathrm{e}^{-x^2}\,\mathrm{e}^{x^2} = -2\,x\,F(x)+1\,, \tag{D.5}$$

thus $F'(0)=1$, which, for $F(x)=\sum_{k=0}^\infty c_k\,x^k$ leads to

$$\sum_{k=0}^\infty k\,c_k\,x^{k-1} + 2\sum_{k=0}^\infty c_k\,x^{k+1} = 1$$

or

$$(k+2)\,c_{k+2} + 2\,c_k = 0 \quad\Leftrightarrow\quad c_{k+2} = -\frac{2}{k+2}\,c_k\,,\quad k\ge 0\,,$$

with $c_0 = 0\,, c_1 = 1\,.$ Thus $c_{2k} = 0\,,\, c_{2k+1} = \frac{(-2)^k}{(2k+1)!!}$ and

$$F(x) = \sum_{k=0}^{\infty} \frac{(-2)^k\, x^{2\,k+1}}{(2k+1)!!}\,. \tag{D.6}$$

Accordingly

$$\begin{aligned} A(p^2) &= \frac{\sqrt{\pi}}{2\,b} + \mathrm{i}\,\frac{\pi}{2}\,p\,\mathrm{e}^{-b^2\,p^2} - \sqrt{\pi}\,p\,F(b\,p) \\ &= \frac{\sqrt{\pi}}{2\,b} + \mathrm{i}\,\frac{\pi}{2}\,p\,\left(1 - (b\,p)^2 + \mathcal{O}((b\,p)^4)\right) - \sqrt{\pi}\,p\,\left(b\,p - \frac{2}{3}(b\,p)^3 + \mathcal{O}((b\,p^4))\right)\,. \end{aligned}$$

Appendix E

Specification of the LM2M2 Potential

The LM2M2 potential V was constructed by Aziz et al. [23, 88]. It consists of a basic HFD-B part V_b and a so-called add-on potential V_a.

$$V(r) = \epsilon\big(V_a(r/r_m) + V_b(r/r_m)\big) \ , \tag{E.1}$$

$$V_a(x) = \begin{cases} A_a \left(\sin\left(\frac{2\pi(x-x_1)}{(x_2-x_1)} - \frac{\pi}{2}\right) + 1\right) \ , & x_1 \le x \le x_2 \ , \\ 0 \ , & x < x_1 \vee x > x_2 \ , \end{cases} \tag{E.2}$$

$$V_b(x) = A^* \exp(-\alpha^* x + \beta^* x^2) - F(x)\left(\frac{c_6}{x^6} + \frac{c_8}{x^8} + \frac{c_{10}}{x^{10}}\right) \ , \tag{E.3}$$

with

$$F(x) = \begin{cases} \exp\left(-\left(\frac{D}{x} - 1\right)^2\right) \ , & x < D \ , \\ 1 \ , & x \ge D \ . \end{cases} \tag{E.4}$$

The constants are collected in Table E.1.

V_b	LM2M2	V_a	LM2M2
A^*	$1.89635353 \cdot 10^5$	A_a	$2.6 \cdot 10^{-3}$
α^*	10.70203539	x_1	1.003535949
β^*	-1.90740649	x_2	1.454790369
D	1.4088	r_m	2.96905 Å
c_6	1.34687065	ϵ	10.97 K
c_8	0.41308398		
c_{10}	0.17060159		

Table E.1: Constants of the potential LM2M2

Bibliography

[1] M. H. Anderson, J. R. Ensher, M. R. Matthews, C. E. Wieman, and E. A. Cornell, Observation of Bose-Einstein Condensation in a Dilute Atomic Vapor, Science **269**, 198 (1995).

[2] S. Jochim, M. Bartenstein, A. Altmeyer, G. Hendl, S. Riedl, C. Chin, J. Hecker Denschlag, and R. Grimm, Bose-Einstein Condensation of Molecules, Science **302**, 2101 (2003).

[3] M. Greiner, C. A. Regal, and D. S. Jin, Emergence of a molecular Bose–Einstein condensate from a Fermi gas, Nature **426**, 537 (2003).

[4] M. W. Zwierlein, C. A. Stan, C. H. Schunck, S. M. F. Raupach, S. Gupta, Z. Hadzibabic, and W. Ketterle, Observation of Bose-Einstein Condensation of Molecules, Phys. Rev. Lett. **91**, 250401 (2003).

[5] W. Zwerger (Ed.): The BCS–BEC Crossover and the Unitary Fermi Gas, Springer-Verlag Berlin Heidelberg, 2012.

[6] E. Braaten, and H.-W. Hammer, Universality in few-body systems with large scattering length, Phys. Rep. **428**, 259 (2006).

[7] V. Efimov, Is a qualitative approach to the three-body problem useful?, Comm. Nucl. Part. Phys. **19**, 271 (1990).

[8] I. Tanihata, H. Savajols, and R. Kanungo, Recent experimental progress in nuclear halo structure studies, Prog. Part. Nucl. Phys. **68**, 215 (2013).

[9] S. Scherer, and M. R. Schindler: A Primer for Chiral Perturbation Theory, 1st Edition, Springer-Verlag Berlin Heidelberg, 2012.

[10] R. Higa, H.-W. Hammer, and U. v. Kolck, $\alpha\alpha$ scattering in halo effective field theory, Nucl. Phys. A **809**, 171 (2008).

[11] G. P. Lepage, How to renormalize the Schrodinger equation, [arXiv:nucl-th/9706029].

[12] J. R. Taylor: Scattering Theory: The Quantum Theory of Nonrelativistic Collisions, Dover Publications Inc., Mineaola New York, 2006.

[13] V. Efimov, Energy levels arising from resonant two-body forces in a three-body system, Phys. Lett. B **33**, 563 (1970).

[14] T. Kraemer, M. Mark, P. Waldburger, J. G. Danzl, C. Chin, B. Engeser, A. D. Lange, K. Pilch, A. Jaakkola, H.-C. Nägerl, and R. Grimm, Evidence for Efimov quantum states in an ultracold gas of caesium atoms, Nature **440**, 315 (2006).

[15] F. Ferlaino, and R. Grimm, Forty years of Efimov physics: How a bizarre prediction turned into a hot topic, Physics **3**, 9 (2010).

[16] S. Tölle, Universelle Eigenschaften weniger Teilchen im harmonischen Oszillator, Universität Bonn, Diplomarbeit, 2009.

[17] T. Busch, B.-G. Englert, K. Rzążewski, and M. Wilkens, Two Cold Atoms in a Harmonic Trap, Found. Phys. **28**, 549 (1998).

[18] F. Werner, and Y. Castin, Unitary Quantum Three-Body Problem in a Harmonic Trap, Phys. Rev. Lett. **97**, 150401 (2006).

[19] M. Barranco, R. Guardiola, S. Hernández, R. Mayol, J. Navarro, and M. Pi, Helium Nanodroplets: An Overview, J. Low Temp. Phys. **142**, 1 (2006).

[20] S. R. Krishnan, L. Fechner, M. Kremer, V. Sharma, B. Fischer, N. Camus, J. Jha, M. Krishnamurthy, T. Pfeifer, R. Moshammer, J. Ullrich, F. Stienkemeier, M. Mudrich, A. Mikaberidze, U. Saalmann, and J.-M. Rost, Dopant-Induced Ignition of Helium Nanodroplets in Intense Few-Cycle Laser Pulses, Phys. Rev. Lett. 107, 173402 (2011).

[21] W. Schöllkopf, and J. P. Toennies, Nondestructive Mass Selection of Small van der Waals Clusters, Science **266**, 1345 (1994).

[22] R. E. Grisenti, W. Schöllkopf, J. P. Toennis, J. R. Manson, T. A. Savas, and H. I. Smith, He-atom diffraction from nanostructure transmission gratings: The role of imperfections, Phys. Rev. A **61**, 033608 (2000).

[23] R. A. Aziz, and M. J. Slaman, An examination of ab initio results for the helium potential energy curve, J. Chem. Phys. **94**, 8047 (1991).

[24] D. Blume, and C. H. Greene, Correlated gaussian hyperspherical method for few-body systems, J. Chem. Phys. **112**, 8053 (2000).

[25] M. Gattobigio, A. Kievsky and M. Viviani, Spectra of helium clusters with up to six atoms using soft-core potentials, Phys. Rev. A **84**, 052503 (2011). [arXiv:1106.3853].

[26] S. Kreuzer, Few-body physics in a finite volume, Universität Bonn, Dissertation, 2010.

[27] E. Epelbaum, H.-W. Hammer, and U.-G. Meißner, Modern theory of nuclear forces, Rev. Mod. Phys. **81**, 1773 (2009).

[28] S. Weinberg, Phenomenological Lagrangians, Physica A **96**, 327 (1979).

[29] H.-W. Hammer, and L. Platter, Efimov physics from a renormalization group perspective, Phil. Trans. Roy. Soc. Lond. A **369**, 2679 (2011). [arXiv:1102.3789].

[30] R. D. Amado, and J. V. Noble, On Efimov's effect: A new pathology of three-particle systems, Phys. Lett. B **35**, 25 (1971).

[31] R. D. Amado, and J. V. Noble, Efimov's effect: A new pathology of three-particle systems. II, Phys. Rev. D **5**, 1992 (1972).

[32] V. Efimov, Qualitative Treatment of Three-Nucleon Properties, Nucl. Phys. A **362**, 45 (1981).

[33] T. B. Ottenstein, T. Lompe, M. Kohnen, A. N. Wenz, and S. Jochim, Collisional Stability of a Three-Component Degenerate Fermi Gas, Phys. Rev. Lett. **101**, 203202 (2008). [arXiv:0806.0587].

[34] J. H. Huckans, J. R. Williams, E. L. Hazlett, R. W. Stites, and K. M. O’Hara, Three-Body Recombination in a Three-State Fermi Gas with Widely Tunable Interactions, Phys. Rev. Lett. **102**, 165302 (2009). [arXiv:0810.3288].

[35] G. Barontini, C. Weber, F. Rabatti, J. Catani, G. Thalhammer, M. Inguscio, and F. Minardi, Observation of Heteronuclear Atomic Efimov Resonances, Phys. Rev. Lett. **103**, 043201 (2009). [arXiv:0901.4584].

[36] N. Gross, Z. Shotan, S. Kokkelmans, and L. Khaykovich, Observation of Universality in Ultracold ^{7}Li Three-Body Recombination, Phys. Rev. Lett. **103**, 163202 (2009). [arXiv:0906.4731].

[37] M. Zaccanti, B. Deissler, C. D’Errico, M. Fattori, M. Jona-Lasinio, S. Müller, G. Roati, M. Inguscio, and G. Modugno, Observation of an Efimov spectrum in an atomic system, Nature Physics **5**, 586 (2009). [arXiv:0904.4453].

[38] S. Knoop, F. Ferlaino, M. Mark, M. Berninger, H. Schöbel, H.-C. Nägerl, and R. Grimm, Observation of an Efimov-like trimer resonance in ultracold atom-dimer scattering, Nature Physics **5**, 227 (2009). [arXiv:0807.3306].

[39] T. Lompe, T. B. Ottenstein, F. Serwane, K. Viering, A. N. Wenz, G. Zürn, and S. Jochim, Atom-Dimer Scattering in a Three-Component Fermi Gas, Phys. Rev. Lett. **105**, 103201 (2010). [arXiv:1003.0600].

[40] S. Nakajima, M. Horikoshi, T. Mukaiyama, P. Naidon and M. Ueda, Nonuniversal Efimov Atom-Dimer Resonances in a Three-Component Mixture of ^{6}Li, Phys. Rev. Lett. **105**, 023201 (2010). [arXiv:1003.1800].

[41] T. Lompe, T. B. Ottenstein, F. Serwane, A. N. Wenz, G. Zürn, and S. Jochim, Radio-Frequency Association of Efimov Trimers, Science **330**, 940 (2010). [arXiv:1006.2241].

[42] Z. Idziaszek, and T. Calarco, Analytical solutions for the dynamics of two trapped interacting ultracold atoms, Phys. Rev. A **74**, 022712 (2006).

[43] J. J. Liang, and C. Zhang, Two ultracold atoms in a completely anisotropic trap, Phys. Scr. **77**, 025302 (2008).

[44] S. Jonsell, H. Heiselberg, and C. J. Pethick, Universal Behavior of the Energy of Trapped Few-Boson Systems with Large Scattering Length, Phys. Rev. Lett. **89**, 250401 (2002). [arXiv:cond-mat/0203014].

[45] S. D. Glazek, and K. G. Wilson, Renormalization of Hamiltonians, Phys. Rev. D **48**, 5863 (1993).

[46] S. D. Glazek, and K. G. Wilson, Perturbative renormalization group for Hamiltonians, Phys. Rev. D **49**, 4214 (1994).

[47] F. Wegner, Flow-equations for Hamiltonians, Ann. Phys. **506**, 77 (1994).

[48] S. K. Bogner, R. J. Furnstahl, and R. J. Perry, Similarity renormalization group for nucleon-nucleon interactions, Phys. Rev. C **75**, 061001 (2007).

[49] E. Jurgenson, Applications of the Similarity Renormalization Group to the Nuclear Interaction, Ohio State Univerity, PhD thesis, 2009.

[50] C. Chin, R. Grimm, P. Julienne, and E. Tiesinga, Feshbach resonances in ultracold gases, Rev. Mod. Phys. **82**, 1225 (2010).

[51] R. Grimm, M. Weidemüller, and Y Ovchinnikov, Optical dipole traps for neutral atoms, Adv. At. Mol. Opt. Phys. **42**, 95 (2000). [arXiv:physics/9902072].

[52] C. N. Cohen-Tannoudji, and W. D. Phillips, New Mechanisms for Laser Cooling, Physics Today **43**, 33 (1990).

[53] H. F. Hess, Evaporative cooling of magnetically trapped and compressed spin-polarized hydrogen, Phys. Rev. B **34**, 3476 (1986).

[54] W. Petrich, M. H. Anderson, J. R. Ensher, and E. A. Cornell, Stable, Tightly Confining Magnetic Trap for Evaporative Cooling of Neutral Atoms, Phys. Rev. Lett. **74**, 3352 (1995).

[55] M. D. Barrett, J. A. Sauer, and M. S. Chapman, All-Optical Formation of an Atomic Bose-Einstein Condensate, Phys. Rev. Lett. **87**, 10404 (2001).

[56] R. E. Grisenti, W. Schöllkopf, J. P. Toennis, G. C. Hegerfeldt, T. Köhler, and M. Stoll, Determination of the Bond Length and Binding Energy of the Helium Dimer by Diffraction from a Transmission Grating Phys. Rev. Lett. **85**, 2284 (2000).

[57] D. C. Zheng, B. R. Barrett, L. Jaqua, J. P. Vary, and R. J. McCarthy, Microscopic calculations of the spectra of light nuclei, Phys. Rev. C **48**, 1083 (1993).

[58] P. Navràtil, S. Quaglioni, I. Stetcu, and B. R. Barrett, Recent developments in no-core shell-model calculations, J. Phys. G **36**, 083101 (2009).

[59] S. Okubo, Diagonalization of Hamiltonian and Tamm-Dancoff Equation, Prog. Theor. Phys. **12**, 603 (1954).

[60] K. Suzuki, and S. Y. Lee, Convergent Theory for Effective Interaction in Nuclei, Prog. Theor. Phys. **64**, 2091 (1980).

[61] D. A. Varshalovich, A. N. Moskalev, and V. K. Khersonskii: Quantum Theory of Angular Momentum, 2nd Edition, World Scientific Publishing, 1988.

[62] S. Tölle, H. W. Hammer, and B. Ch. Metsch, Convergence properties of the effective theory for trapped bosons, J. Phys. G **40**, 055004 (2013).

[63] L. Trlifaj, Simple Formula for the General Oscillator Brackets, Phys. Rev. C **5** 1534 (1972).

[64] J. W. Negele, and H. Orland: Quantum Many-Particle Systems, Addison-Wesley Publishing Company, 1988.

[65] A. G. M. van Hees, and P. W. M. Glaudemans, A Tanslationally Invariant Shell-Model Treatment of (0+1)$\hbar\omega$ States in A=4-16 Nucleit (I), Z. Phys. A - Atoms and Nuclei **314**, 323 (1983).

[66] J. Stoer, and R. Bulirsch: Numerische Mathematik 2, 5. Aufl., Springer-Verlag Berlin Heidelberg New York, 2005.

[67] S. Tölle, H.-W. Hammer, and B. Ch. Metsch, Universal few-body physics in a harmonic trap, C. R. Phys. **12**, 59 (2011).

[68] I. Stetcu, B. R. Barrett, and U. van Kolck, No-core shell model in an effective-field-theory framework, Phys. Lett. B **653**, 358 (2007). [arXiv:nucl-th/0609023].

[69] I. Stetcu, J. Rotureau, B. R. Barrett, and U. van Kolck, Effective interactions for light nuclei: An Effective (field theory) approach, J. Phys. G **37**, 064033 (2010). [arXiv:0912.3015].

[70] J. Rotureau, I. Stetcu, B. R. Barrett, and U. van Kolck, Two and Three Nucleons in a Trap and the Continuum Limit, Phys. Rev. C **85**, 034003 (2012). [arXiv:1112.0267].

[71] E. D. Jurgenson, P. Navrátil, and R. J. Furnstahl, Evolving Nuclear Many-Body Forces with the Similarity Renormalization Group, Phys. Rev. C **83**, 034301 (2011). [arXiv:1011.4085].

[72] G. Hagen, T. Papenbrock, D. J. Dean, and M. Hjorth-Jensen, Ab inition coupled-cluster approach to nuclear structure with modern nucleon-nucleon interactions, Phys. Rev. C **82**, 034330 (2010). [arXiv:1005.2627].

[73] S. A. Coon, M. I. Avetian, M. K. G. Kruse, U. van Kolck, P. Maris, and J. P. Vary, Convergence properties of ab initio calculations of light nuclei in a harmonic oscillator basis, [arxiv:1205.3230].

[74] H.-W. Hammer and L. Platter, Universal properties of the four-body system with large scattering length, Eur. Phys. J. A **32**, 113 (2007). [arXiv:nucl-th/0610105].

[75] J. von Stecher, J. P. D'Incao, and C. H. Greene, Signatures of universal four-body phenomena and their relation to the Efimov effect, Nature Physics **5**, 417 (2009). [arXiv:0810.3876].

[76] F. Ferlaino, S. Knoop, M. Berninger, W. Harm, J. P. D'Incao, H.-C. Nägerl, and R. Grimm, Evidence for Universal Four-Body States Tied to an Efimov Trimer, Phys. Rev. Lett. **102**, 140401 (2009). [arXiv:0903.1276].

[77] I. Stetcu, J. Rotureau, B. R. Barrett, and U. van Kolck, An effective field theory approach to two trapped particles, Ann. Phys. **325**, 1644 (2010). [arXiv:1001.5071].

[78] P. F. Bedaque, H.-W. Hammer, and U. van Kolck, Renormalization of the Three-Body System with Short-Range Interactions, Phys. Rev. Lett. **82**, 463 (1999). [arXiv:nucl-th/9809025].

[79] H.-W. Hammer, A. Nogga, and A. Schwenk, Colloquium: Three-body forces: From cold atoms to nuclei, Rev. Mod. Phys. **85**, 197 (2013). [arXiv:1210.4273].

[80] R. J. Furnstahl, private communication.

[81] I. M. Delves in Advances in Nuclear Physics, Vol. 5, M. Baranger and E. Vogt (Eds.), Plenum Press New York, 1972.

[82] T. R. Schneider, Convergence of generalized spherical harmonic expansions in the three nucleon bound state, Phys. Lett. B **40**, 439 (1972).

[83] R. J. Furnstahl, G. Hagen, and T. Papenbrock, Corrections to nuclear energies and radii in finite oscillator spaces, Phys. Rev. C **86**, 031301 (2012). [arXiv:1207.6100].

[84] G. J. Hanna, and D. Blume, Energetics and structural properties of three-dimensional bosonic clusters near threshold, Phys. Rev. A **74**, 063604 (2006).

[85] J. von Stecher, Five- and Six-Body Resonances Tied to an Efimov Trimer, Phys. Rev. Lett. **107**, 200402 (2011). [arXiv:1106.2319].

[86] A. N. Nicholson, N-body Efimov states from two-particle noise, Phys. Rev. Lett. **109**, 073003 (2012). [arXiv:1202.4402].

[87] M. Gattobigio, A. Kievsky, and M. Viviani, Nonsymmetrized hyperspherical harmonic basis for an A-body system, Phys. Rev. Lett. **83**, 024001 (2011).

[88] R. A. Aziz, F. R. W. McCourt, and C. C. K. Wong, A new determination of the ground state interatomic potential for He_2, Mol. Phys. **61**, 1487 (1987).

[89] A. K. Motovilov, W. Sandhas, S. A. Sofianos, and E. A. Koganova, Binding energies and scattering observables in the $^4He_3$ atomic system, Eur. Phys. J. D **13**, 33 (2001).

[90] A. Nogga, S. K. Bogner, and A. Schwenk, Low-momentum interaction in few-nucleon systems, Phys. Rev. C **70**, 061002 (2004). [nucl-th/0405016].

[91] M. Lüscher, Volume dependence of the energy spectrum in massive quantum field theories, Commun. Math. Phys. **105**, 153 (1986).

[92] M. Lüscher, Two-particle states on a torus and their relation to the scattering matrix, Nucl. Phys. B **354**, 531 (1991).

[93] S. R. Beane, W. Demold, K. Orginos, and M. J. Savage, Nuclear Physics from Lattice QCD, Prog. Part. Nucl. Phys. **66**, 1 (2011). [arXiv:1004.2935].

[94] T. Luu, M. J. Savage, A. Schwenk, and J. P. Vary, Nucleon-nucleon scattering in a harmonic potential, Phys. Rev. C **82**, 034003 (2010). [arXiv:1006.0427].

[95] S. Jonsell, Interaction Energy of Two Trapped Bosons with Long Scattering Lengths, Few-Body Systems **31**, 255 (2002).

[96] A. Suzuki, Y. Liang, and R. K. Bhaduri, Two-atom energy spectrum in a harmonic trap near a Feshbach resonance at higher partial waves, Phys. Rev. A **80**, 033601 (2009).

[97] M. Abramowitz, and I. A. Stegun: Handbook of Mathematical Functions, 9th Edition, Dover Publications (1984).

[98] J. Rotureau, I. Stetcu, B. R. Barrett, M. C. Birse, and U. v. Kolck, Three and Four Harmonically Trapped Particles in an Effective Field Theory Framework, [arXiv:1006.3820v2].

[99] S. Bour, H.-W. Hammer, D. Lee, and U.-G. Meißner, Benchmark calculations for elastic fermion-dimer scattering, Phys. Rev. C **86**, 034003 (2012).

[100] B. E. Grinyuk, I. V. Simenog, and A. I. Sitnichenko, Yad. Fiz. **39**, 402 (1984). [Sov. J. Nucl. Phys. **39**, 253 (1984)]

[101] J. v. Stecher, C. H. Greene, and D. Blume, Energetics and structural properties of trapped two-component Fermi gases, Phys. Rev. A **77**, 043619 (2008).

[102] D. S. Petrov, C. Salomon, and G. V. Shlyapnikov, Scattering properties of weakly bound dimers of fermionic atoms, Phys. Rev. A **71**, 012708 (2005).

[103] V. Bernard, M. Lage, U.-G. Meißner, and A. Rusetsky, Resonance properties from the finite-volume energy spectrum, JHEP **0808**, 024 (2008). [arXiv:0806.4495].

Danksagung

An erster Stelle gebührt der Dank meinen Betreuern Prof. Dr. Hans-Werner Hammer und PD. Dr. Bernard C. Metsch. Beide standen mir bei Fragen mit Rat und Tat zur Seite. Nur durch viele hilfreiche Gespräche und Diskussionen konnte meine Arbeit in dieser Form erfolgreich abgeschlossen werden.

Ebenso gilt mein Dank meinen Kollegen. Im wöchentlichen Kolloquium konnte ich im fachlichen Austausch neue Einsichten gewinnen und neue Denkanstöße erhalten. Darüber hinaus war die Atmosphäre freundschaftlich und offen. Auch die tatkräftige Unterstützung der guten Seele im Haus, unserer Sekretärin Barbara Mosblech, bei jeglichen organisatorischen Problemen war Gold wert.

Besonders hervorheben möchte ich meine Bürokollegen: Michael Ronniger, Christoph Ditsche und Christopher Helmes. Bei Schwierigkeiten jedweder Art versuchten wir, uns gegenseitig zu unterstützen und unter die Arme zu greifen. Insgesamt war es eine erfreuliche Zeit, die ich im HISKP verbringen durfte.

Nicht unerwähnt bleiben soll die gute Zusammenarbeit mit Prof. Christian Forssén. Ohne ihn wäre ein großer Teil der Arbeit nicht möglich gewesen. Aus seiner Arbeitsgruppe soll insbesondere Boris Carlsson genannt werden, dessen Fortschritte in der SRG-Transformation mir neue Möglichkeiten eröffneten.

Weiterhin möchte ich mich bei Prof. Dr. Stefan Linden und Prof. Dr. Thomas Bredow für ihre Bereitschaft bedanken, meine Promotionskommission zu vervollständigen.

Am Ende dieser Arbeit kann ich gar nicht genug meiner ganzen Familie danken. Ob Geschwister oder Eltern, ihr wart immer für mich da. Besonders meiner Frau Katja danke ich für die immerwährende Geduld und Rücksichtnahme im Endspurt dieser Arbeit. Zu guter Letzt danke ich meiner kleinen Tochter Emilia, dass sie einfach da ist.